dortmund university

Dissertation

Renal ASBT as a therapeutic target for cholemic nephropathy caused by cholestatic liver diseases

Zur Erlangung des akademischen Grades des Doktors der Naturwissenschaften (Dr. rer. nat.)

Vorgelegt an der Fakultät für Chemie und Chemische Biologie an der Technischen Universität Dortmund

Von Zaynab Hobloss

Dortmund, März 2025

Erstgutachter: Prof. Dr. Jan G. Hengstler

Zweitgutachter: Prof. Dr. Jörg Rahnenführer

IfADo
LEIBNIZ RESEARCH CENTRE
FOR WORKING ENVIRONMENT
AND HUMAN FACTORS

To my Family

Table of Contents

Table of contents

1 Abstract

Chronic liver diseases are prevalent, and a significant proportion of patients exhibit cholestasis, characterised by elevated bile acid concentrations in the general circulation. This exposure can result in adverse effects, including acute kidney injury, a frequently lethal complication of cholestatic liver disease. The potential role of bile acids in the pathogenesis of kidney injury has been a subject of speculation, leading to the term "cholemic nephropathy". However, the underlying mechanisms of this disease remain to be elucidated, and a specific therapeutic intervention remains elusive. To address this knowledge gap, a mouse model was employed, in which the common bile duct was ligated (BDL), resulting in elevated bile acid concentrations in the blood and various tissues. Subsequent to BDL, the mice were observed to develop kidney injury. The aim of my study was to illustrate the bile flux in renal tissue using intravital imaging. The study demonstrated that a fluorophore-coupled taurocholic acid (NBD-TCA) is taken up by proximal renal tubular epithelial cells (pTEC) and is enriched in this cell type. Following this enrichment, a series of observations were made, including cell death events of pTEC, immune cell infiltration, tubular dilatation and casts, leaky peritubular capillaries, fibrosis and enlarged glomeruli. These observations were subsequently confirmed through histological analysis and immune-staining of tissues, as well as analysis of biomarkers of kidney injury, including increased KIM-1, NGAL, cystatin C and, in the latest stages, creatinine. The subsequent study investigated the hypothesis that specific transporters may be responsible for the accumulation of bile acids in pTEC. Using specific inhibitors, I demonstrated that the inhibition of the apical sodium-dependent bile acid transporter (ASBT) almost completely blocked TCA accumulation in pTEC of mice after BDL. Importantly, ASBT inhibition prevented pTEC death events and strongly ameliorated all above described hallmarkers of kidney injury.

In conclusion, systemic ASBT inhibition may represent an efficient therapeutic strategy for the treatment of cholemic nephropathy if the results obtained in mice are relevant for the human situation.

2 Zusammenfassung

Chronische Lebererkrankungen sind weit verbreitet, und ein erheblicher Anteil der Patienten weist eine Cholestase auf, die durch erhöhte Gallensäurekonzentrationen im allgemeinen Kreislauf gekennzeichnet ist. Diese Exposition kann schädliche Auswirkungen haben, darunter die akute Nierenschädigung, e häufig tödlich verlaufende Komplikation der cholestatischen Lebererkrankung. Über die mögliche Rolle von Gallensäuren bei der Entstehung von Nierenschäden wird spekuliert, was zu dem Begriff „cholestatische Nephropathie“ geführt hat. Die dieser Krankheit zugrunde liegenden Mechanismen sind jedoch noch nicht geklärt, und ein spezifischer therapeutischer Eingriff ist nach wie vor nicht möglich.Um diese Wissenslücke zu schließen, wurde ein Mausmodell verwendet, bei dem der Hauptgallengang ligiert wurde (BDL), was zu erhöhten Gallensäurekonzentrationen im Blut und in verschiedenen Geweben führte. Im Anschluss an die BDL wurde bei den Mäusen eine Nierenschädigung beobachtet. Ziel meiner Studie war es, den Gallenfluss im Nierengewebe mit Hilfe der intravitalen Bildgebung zu veranschaulichen. Die Studie zeigte, dass eine fluorophorgekoppelte Taurocholsäure (NBD-TCA) von renalen Tubulusepithelzellen (pTEC) aufgenommen und in diesem Zelltyp angereichert wird. Nach dieser Anreicherung wurde eine Reihe von Beobachtungen gemacht, darunter Zelltod von pTEC, Infiltration von Immunzellen, tubuläre Dilatation und Ablagerungen, undichte peritubuläre Kapillaren, Fibrose und vergrößerte Glomeruli. Diese Beobachtungen wurden anschließend durch histologische Analysen und Immunfärbungen von Geweben sowie durch die Analyse von Biomarkern für Nierenschäden, einschließlich erhöhter KIM-1-, NGAL- und Cystatin-C-Werte und, in den letzten Stadien, Kreatininwerte, bestätigt. In der anschließenden Studie wurde die Hypothese untersucht, dass spezifische Transporter für die Anhäufung von Gallensäuren in pTEC verantwortlich sein könnten. Mit Hilfe spezifischer Inhibitoren konnte ich zeigen, dass die Hemmung des apikalen natriumabhängigen Gallensäuretransporters (ASBT) die TCA-Akkumulation in pTEC von Mäusen nach BDL fast vollständig blockierte. Wichtig ist, dass die ASBT-Hemmung das Absterben von pTEC verhinderte und alle oben beschriebenen Kennzeichen der Nierenschädigung stark verbesserte.

Zusammenfassend lässt sich sagen, dass die systemische ASBT-Hemmung eine wirksame therapeutische Strategie für die Behandlung der cholemischen Nephropathie darstellen könnte, wenn die bei Mäusen erzielten Ergebnisse für die Situation beim Menschen relevant sind.

3 Explanation to the present PhD

Results of my PhD studies have been published in 14 publications. In the next chapters I focus on a specific study (Ghallab et al., 2024) in which the so far unknown mechanism of a specific disease "cholemic nephropathy" (CN) was elucidated leading to a new therapeutic strategy. The following chapters contain images and contents that have already been published in *Ghallab et al.,* 2024 [1].

4 List of publications of my PhD

- **Inhibition of the Renal Apical Sodium Dependent Bile Acid Transporter Prevents Cholemic Nephropathy in Mice with Obstructive Cholestasis.**

Ghallab A, González D, Strängberg E, Hofmann U, Myllys M, Hassan R, **Hobloss Z**, Brackhagen L, Begher-Tibbe B, Duda JC, Drenda C, Kappenberg F, Reinders J, Friebel A, Vucur M, Turajski M, Seddek AL, Abbas T, Abdelmageed N, Morad SAF, Morad W, Hamdy A, Albrecht W, Kittana N, Assali M, Vartak N, van Thriel C, Sous A, Nell P, Villar-Fernandez M, Cadenas C, Genc E, Mar-chan R, Luedde T, Åkerblad P, Mattsson J, Marschall HU, Hoehme S, Stirnimann G, Schwab M, Boor P, Amann K, Schmitz J, Bräsen JH, Rahnenführer J, Edlund K, Karpen SJ, Simbrunner B, Reiberger T, Mandorfer M, Trauner M, Dawson PA, Lindström E, Hengstler JG. J Hepatol. 2023 Nov 6:S0168-8278(23)05235-2. doi: 10.1016/j.jhep.2023.10.035. Impact Factor: 26.8.

- **Interruption of bile acid uptake by hepatocytes after acetaminophen overdose ameliorates hepatotoxicity.**

Ghallab A, Hassan R, Hofmann U, Friebel A, **Hobloss Z**, Brackhagen L, Begher-Tibbe B, Myllys M, Reinders J, Overbeck N, Sezgin S, Zühlke S, Seddek AL, Murad W, Brecklinghaus T, Kappenberg F, Rahnenführer J, Gon-zález D, Goldring C, Copple IM, Marchan R, Longerich T, Vucur M, Luedde T, Urban S, Canbay A, Schreiter T, Trauner M, Akakpo JY, Olyaee M, Curry SC, Sowa JP, Jaeschke H, Hoehme S, Hengstler JG. J Hepatol. 2022 Jul;77(1):71-83. doi: 10.1016/j.jhep.2022.01.020. Epub 2022 Feb 5. PMID: 35131407. Impact Factor: 25.7.

- **Cognitive Functions, Neurotransmitter Alterations, and Hippocampal Microstructural Changes in Mice Caused by Feeding on Western Diet.**

Custodio RJP+, **Hobloss Z+,** Myllys M+ Hassan R, González D, Reinders J, Bornhorst J, Weishaupt AK, Seddek AL, Abbas T, Friebel A, Hoehme S, Getzmann S, Hengstler JG, van Thriel C, Ghallab A. Cells. 2023 Sep 21;12(18):2331. doi: 10.3390/cells12182331. Impact Factor: 5.1. **+ indicates shared first authorship**

- **Loss of bile salt export pump aggravates lipopolysaccharide-induced liver injury in mice due to impaired hepatic endotoxin clearance.**

Remetic J, Ghallab A, **Hobloss Z**, Brackhagen L, Hassan R, Myllys M, Radun R, Mlitz V, Zhu C, Baumgartner M, Schrottmaier WC, Mussbacher M, Timelthaler G, Scharnagl H, Stojakovic T, Assinger A, Fuchs CD, Hengstler JG, Trauner M. Hepatology. 2022 May;75(5):1095-1109. doi: 10.1002/hep.32289. Epub 2022 Jan 19. Impact Factor: 14.00.

- **Spatio-Temporal Multiscale Analysis of Western Diet-Fed Mice Reveals a Translationally Relevant Sequence of Events during NAFLD Progression.**

Ghallab A, Myllys M, Friebel A, Duda J, Edlund K, Halilbasic E, Vucur M, **Hobloss Z**, Brackhagen L, Begher-Tibbe B, Hassan R, Burke M, Genc E, Frohwein LJ, Hofmann U, Holland CH, González D, Keller M, Seddek AL, Ab-bas T, Mohammed ESI, Teufel A, Itzel T, Metzler S, Marchan R, Cadenas C, Watzl C, Nitsche MA, Kappenberg F, Luedde T, Longerich T, Rahnenführer J, Hoehme S, Trauner M, Hengstler JG. Cells. 2021 Sep 23;10(10):2516. doi: 10.3390/cells10102516.Impact Factor: 7.666.

- **Hypoalbuminemia affects the spatio-temporal tissue distribution of ochratoxin A in liver and kidneys: consequences for organ toxicity.**

Hassan R, Friebel A, Brackhagen L, **Hobloss Z**, Myllys M, González D, Al-brecht W, Mohammed ESI, Seddek AL, Marchan R, Cadenas C, Cramer B, Humpf HU, Hartl L, Simbrunner B, Reiberger T, Trauner M, Hoehme S, Degen GH, Hengstler JG, Ghallab A. Arch Toxicol. 2022 Nov;96(11):2967-2981. doi: 10.1007/s00204-022-03361-8. Epub 2022 Aug 13Impact Factor: 6.168.

- **Inhibition of cytochrome P450 enhances the nephro- and hepatotoxicity of ochratoxin A.**

Hassan R, González D, **Hobloss Z**, Brackhagen L, Myllys M, Friebel A, Seddek AL, Marchan R, Cramer B, Humpf HU, Hoehme S, Degen GH, Hengstler JG, Ghallab A. Arch Toxicol. 2022 Dec;96(12):3349-3361. doi: 10.1007/s00204-022-03395-y. Epub 2022 Oct 13. Impact Factor: 6.168.

- **Colchicine overdose impairs the capacity of Kupffer cells to clear foreign parti-cles and endotoxins.**

Hassan R, Myllys M, Brackhagen L, **Hobloss Z**, González D, Seddek AL, Friebel A, Hoehme S, Marchan R, Trauner M, Hengstler JG, Ghallab A. Arch Toxicol. 2022 Nov;96(11):3067-3076. doi: 10.1007/s00204-022-03353-8. Epub 2022 Sep 14. Impact Factor: 6.168.

- **Increased sinusoidal export of drug glucuronides is a compensative mechanism in liver cirrhosis of mice.**

Fendt R, Ghallab A, Myllys M, Hofmann U, Hassan R, **Hobloss Z**, González D, Brackhagen L, Marchan R, Edlund K, Seddek AL, Abdelmageed N, Blank LM, Schlender JF, Holland CH, Hengstler JG, Kuepfer L. Front Pharmacol. 2023 Nov 20;14:1279357. doi: 10.3389/fphar.2023.1279357. eCollection 2023. PMID: 38053838. Impact Factor: 4.4.

- **Integrated data from intravital imaging and HPLC-MS/MS analysis reveal large interspecies differences in AFB1-metabolism in mice and rats.**

Hassan R, Gerdemann A, Cramer B, **Hobloss Z**, Myllys M, González D, Albrecht W, Veerkamp J, Friebel A, Hoehme S, Esselen M, Degen GH, Humpf HU, Hengstler JG, Ghallab A. Arch Toxicol. 2024 Apr;98(4):1081-1093. doi: 10.1007/s00204-024-03688-4. Epub 2024 Mar 4. PMID: 38436695. Impact Factor: 4.8.

- **Acetaminophen overdose causes a breach of the blood-bile barrier in mice but not in rats.**

Hassan R, **Hobloss Z**, Myllys M, González D, Begher-Tibbe B, Reinders J, Friebel A, Hoehme S, Abdelmageed N, Abbas AA, Seddek AL, Morad SAF, Hengstler JG, Ghallab A. Arch Toxicol. 2024 May;98(5):1533-1542. doi: 10.1007/s00204-024-03705-6. Epub 2024 Mar 11. PMID: 38466352. Impact Factor: 4.8.

- **Role of albumin in the metabolism and excretion of ochratoxin A.**

Kuhn M, Hassan R, González D, Myllys M, **Hobloss Z**, Degen GH, Humpf HU, Hengstler JG, Cramer B, Ghallab A. Mycotoxin Res. 2024 May 14. doi: 10.1007/s12550-024-00538-1. Online ahead of print. PMID: 38743341. Impact Factor: 3.0.

- **Role of WISP1 in Stellate Cell Migration and Liver Fibrosis**

Daniela González, Gisela Campos, Larissa Pütter, Adrian Friebel, Christian H Holland, Leonhard Holländer, Ahmed Ghallab, **Zaynab Hobloss**, Maiju Myllys, Stefan Hoehme, Nadja M Meindl-Beinker, Steven Dooley, Rosemarie Marchan, Thomas S Weiss, Jan G Hengstler, Patricio Godoy. Cells. 2024 Sep 29;13(19):1629. doi: 10.3390/cells13191629. Impact Factor: 5.1.

- **Validation of NBD-coupled taurocholic acid for intravital analysis of bile acid transport in liver and kidney of mice**

Ahmed Ghallab [1 2], Sebastian Kunz [3], Celine Drossel [4], Veronica Billo [3], Adrian Friebel [5], Mats Georg [4], Richard Göttlich [4], **Zaynab Hobloss [1]**, Reham Hassan [1 2], Maiju Myllys [1], Abdel-Latief Seddek [2], Noha Abdelmageed [6], Paul A Dawson [7], Erik Lindström [8], Stefan Hoehme [5], Jan G Hengstler [1], Joachim Geyer [3]. EXCLI J. 2024 Oct 30:23:1330-1352.doi: 10.17179/excli2024-7707. eCollection 2024.

5 Abbreviations

%	Percentage
°C	Celsius degree
Ab	Antibody
ALT	Alanine transaminase
ALP	Alkaline phosphatase
ASBT	Apical sodium-dependent bile acid transporter
AST	Aspartate transaminase
BDL	Bile duct ligation
BSEP	Bile Salt Export Pump
CC1	Cell conditioning 1
CK	Cytokeratin
CLF	Cholyl-L-lysyl-fluorescein
CN	Cholemic nephropathy
Cyp7a1	Cytochrome P450 enzyme cholesterol 7α-hydroxylase
DAPI	4',6-diamidino-2-phenylindole
g	Gram
h	Hour(s)
H&E	Hematoxylin and eosin
KIM-1	kidney injury molecule
MALDI-MSI	Matrix-assisted laser desorption/ionization mass spectrometric imaging
mg	Milligram
min	Minute(s)
ml	Milliliter
MRP	Multidrug resistance-associated protein
NGAL	neutrophil gelatinase-associated lipocalin
NTCP	Na+-taurocholate co-transporting polypeptide
OATP	Organic anion-transporter
OST	Organic solute transporter
PBS	Phosphate-buffered saline solution
PCR	Polymerase chain reaction
PFA	Paraformaldehyde
pTEC	Proximal tubular epithelial cells
qRT-PCR	Quantitative real time PCR
RNA	Ribonucleic acid
TCA	Taurocholic acid
TMRE	Tetramethylrhodamine ethyl ester
µm	Micrometer

List of figures & tables

6 List of figures

List of figures & tables

List of figures & tables

List of figures & tables

List of figures & tables

7 List of tables

8 Introduction

Chronic liver diseases can lead to an increase in harmful bile acids, which can affect several organs[2]. One serious complication is cholemic nephropathy[3-5], which causes renal dysfunction[6, 7]. The exact mechanisms of cholemic nephropathy have been unclear, and there is currently no pharmacological treatment available[4, 8].

The microanatomy and transporters of the liver and kidney have already been reviewed [3, 6-8]. In this section, a concise summary of the key facts is provided to understand the experiments and conclusions of the present study.

In several liver diseases, there is an increase in bile acid concentrations in the systemic circulation[9]. This is due to a well-established mechanism in which the bile acid uptake transporter sodium/taurocholate cotransporting polypeptide (NTCP) is downregulated in response to liver inflammation[10]. Consequently, hepatocytes have a reduced capacity to clear bile acids from the blood, which contributes to increased blood bile acid concentrations (Fig. 1)[11]. Furthermore, two transporters located at the sinusoidal blood side of hepatocytes are upregulated, namely the organic anion transporters called Multidrug Resistance-Related Proteins 3 and 4 (MRP3 and MRP4)[12]. Consequently, bile acids that have been taken up by hepatocytes despite NTCP downregulation are immediately exported back to blood by MRP3 and MRP4, contributing to increased bile acid blood concentrations (Fig. 1)[10-12].

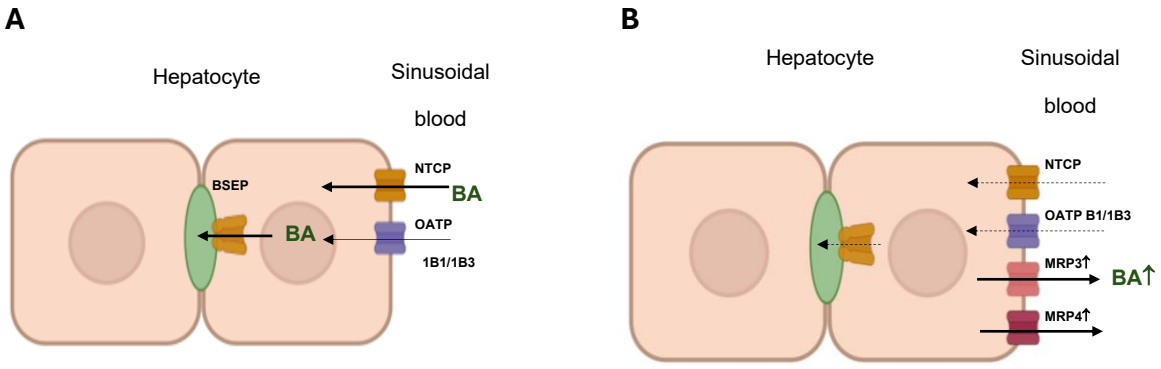

Fig. 1: Bile acid transport in the liver. **A:** Bile acids are transported to hepatocytes by sinusoidal uptake transporters such as NTCPs and OATPs. Bile acids are further transported to the bile canaliculi via BSEP and MRP2. **B:** At high concentrations bile acids are transported back to the systemic circulation via MRP3, MRP4. Figure modified from Ghallab et al, 2025, submitted review.

The kidney consists of an approximately 1000000 nephrons, consisting of the glomerulus, where filtration of blood occurs to generate the primary urine (Fig. 2)[13]. The primary urine flows through the proximal tubule, loop of Henle, distal tubule, collecting

duct and further to the urinary bladder. During the passage of the primary urine through the nephron, specific solutes are reabsorbed (Fig. 2, A)[13]. For the present study it is critical that several bile acids are reabsorbed from the tubular lumen into the cytoplasm of proximal tubular epithelial cells (pTEC). This uptake is mediated by the apical sodium-dependent bile acid transporter (ASBT). After the uptake of bile acids into pETC they are actively excreted at the opposite pole of pETC due to the activity of the organic solute transporters α-β (OST α-β), reaching the interstitium, from where they reach the peritubular blood capillaries and return to the general circulation (Fig. 2, B).

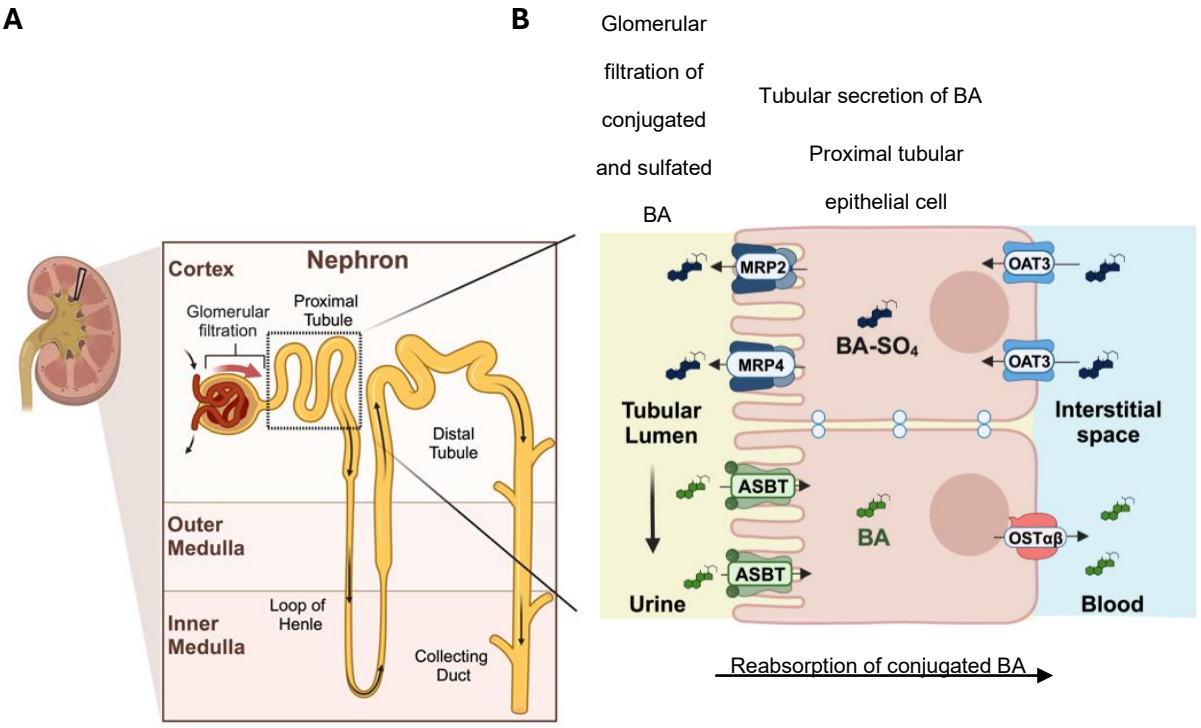

Fig. 2: Primary urine flows. A: the passage of the primary urine through the proximal tubule, loop of Henle, distal tubule and collecting duct. B: Reabsorption of bile acids into the proximal tubular epithelial cells (pTEC) by the apical sodium-dependent bile acid transporter (ASBT). Figure modified from Ghallab et al, 2025, submitted review.

As mentioned above, high bile acid concentrations can cause acute kidney injury, also named cholemic nephropathy (CN)[3-5]. CN is a severe complication of cholestatic liver disease with an often-lethal outcome. The exact mechanism of CN is unknown. Therefore, the aim of this study was to elucidate the molecular mechanism of CN and to develop a therapeutic strategy. For this purpose, I used a mouse model that recapitulates key events of human CN, namely bile duct ligation (BDL). In BDL the common bile duct (between gallbladder and duodenum) is ligated, leading to a strong increase of bile acids and further compounds present in bile in the systemic circulation. This has already been

shown to cause features of CN in the kidneys [9], such as cell death of tubular epithelial cells and so called “tubular casts” that also represent a hallmark of human CN. Here, I support that enrichment of bile acids in pTEC due to ASBT is an early key event of CN. Importantly, inhibition of ASBT by a small molecular compound prevented bile acid accumulation in pTEC and ameliorated all symptoms of the disease.

9 Aim of this work

Chronic liver diseases are widespread, and many patients suffer from cholestasis. This is characterised by elevated bile acid concentrations. Exposure can lead to adverse effects such as acute kidney damage, which is often fatal, and it is speculated that bile acids cause kidney damage. However, the underlying mechanisms are still unclear and there are no clear therapies yet. The overall aim of this work was to investigate the mechanisms and establish the prevention of the progression of CN. To achieve this goal, the work programme was divided into the following tasks:

1. Establishment of a cholestatic mouse model
2. Evaluation of renal damage in this model
3. Identification of the molecular mechanisms responsible for CN
4. Examination of the alteration of bile acid transport during the progression of CN
5. Targeting the identified mechanisms of CN and designing therapeutic interventions to prevent CN progression
6. Evaluation of the efficacy of the intervention on CN

10 Materials and methods

Please note that I described all materials and methods used for this thesis already in the publication Ghallab et al., 2024. Therefore, the following descriptions represent a literal reproduction of my already published text in 2024.

10.1 Materials

10.1.1 Table 1: Antibodies.

Name	Supplier	Cat no.
Recombinant anti-cytokeratin 19 antibody	Abcam	ab52625
Purified rat anti-mouse CD45	BD-Pharminogen	550539
Anti-MECA-32	DSHB	AB_531797
SLC10A2 polyclonal antibody/ASBT	Invitrogen	PA5-18990
SLC10A2 polyclonal antibody/ASBT	Invitrogen	PA5-52108
Ultra-Map anti rabbit HRP	Roche	05269717001
Ultra-Map anti rabbit Alk Phos	Roche	05269709001
AQP1 polyclonal antibody	Proteintech	20333-1-AP
Rabbit anti-thiazide sensitive NaCl co-transporter affinity purified polyclonal antibody	Millipore	AB3553
UltraMap anti-goat multimer	Roche	06607241001

OmniMap anti-rat HRP	Roche	05891892001
CD31 (PECAM-1) Monoclonal Antibody	Thermofisher Scientific	62-0311-82
Anti-Aquaporin 2 antibody	Abcam	ab199975

10.1.2 Table 2 : Consumables (e.g. drugs, proteins, vectors etc.).

Name	Supplier	Cat no.
AS0369	Albireo	-
Hoechst 33258	Thermo Fisher Scientific	H21491
Tetramethylrhodamin-Ethylester (TMRE)	Thermo Fisher Scientific	T669
Rhodamine123	Thermo Fisher Scientific	R302
Cholyl-lysyl-fluorescein (CLF)	Corning, USA	451041
Fluorescein-coupled TCA	Synthesized by Naim Kittana and Mohyeddin Assali	-
Evans blue	Sigma-Aldrich	E2129
SYTOX green	Thermo Fisher Scientific	S7020
2',7'Dichlorofluorescein diacetate	Sigma Aldrich	287810-100MG
Discovery inhibitor (H2O2 blocker)	Roche	7017944001
Eosin Y	Sigma-Aldrich	E4382-25g
Picrosirius red stain kit	Polyscience, Inc.	249410-250
Bluing Reagent	Roche	05 266 769 001
Bile Stain Kit-Halls	StatLab	KTHBI
Discovery Purple Kit RUO	Roche	07 053 983 001
Chromo Map DAB	Roche	05 266 645 001
Piccolo general chemistry 13	Hitado	AB-114-400-0029
Hematoxylin II	Roche	05 277 965 001
Discovery Teal HRP Kit (RUO)	Roche	8254338001
Mouse Lipocalin-2/NGAL DuoSet ELISA	R&D Systems	DY1857

DuoSet ELISA Ancillary Reagent Kit 2	R&D Systems	DY008
Human Lipocalin-2/NGAL Quantikine ELISA kit	R&D Systems	DLCN20
Mouse KIM 1 ELISA Kit	Abcam	ab213477
Human Serum TIM-1/KIM-1 HAVCR Quantikine ELISA kit	R&D Systems	DSKM100
Mouse Cystatin C ELISA Kit	Abcam	ab201280
Human Cystatin C Quantikine ELISA kit	R&D Systems	DSCTC0
RNeasy Mini Kit	Qiagen	74106
TaqMan universal mastermix with UNG	Thermo Fisher Scientific	4426710
High-Capacity cDNA Reverse Transcription Kit	Thermo Fisher Scientific	4368814
Bile Acid Standard 1 Mix (unconjugated)	Cambridge Isotope Laboratories, Inc.	MSK-BA1-1
Bile Acid Standard 1 Mix (unconjugated) unlabelled standard	Cambridge Isotope Laboratories, Inc.	MSK-BA1-US-1
Bile Acid Standard 2 Mix (conjugated)	Cambridge Isotope Laboratories, Inc.	MSK-BA2-1
Bile Acid Standard 2 Mix (conjugated) unlabelled standard	Cambridge Isotope Laboratories, Inc.	MSK-BA2-US-1
7α-Hydroxy-4-cholesten-3-one (C4)	Sigma-Aldrich	52853-1MG
Cholic acid sulfate (CA-S)	IsoSciences LLC	13098UNL3SO
Taurocholic acid sulfate, sodium salt (TCA-S)	IsoSciences LLC	13232UNL3SO
α-Tauro-muricholate, sodium salt (αTMCA)	Toronto Research Chemicals	T009130
β-Tauro-muricholate, sodium salt (βTMCA)	Toronto Research Chemicals	T009135
α-Muricholate (αMCA)	Toronto Research Chemicals	M732750
ω-Muricholate (ωMCA)	Toronto Research Chemicals	M732760
d4- Cholic acid sulfate (d4-CA-S)	IsoSciences LLC	130983SO
d4- Taurocholic acid sulfate, sodium salt (d4-TCA-S)	IsoSciences LLC	132323SO
d4-α-Tauro-muricholate, sodium salt (d4-αTMCA)	Toronto Research Chemicals	T009132

d4-β-Tauro-muricholate, sodium salt (d4-βTMCA)	Toronto Research Chemicals	T009137
d5-α-Muricholate (d5-αMCA)	Toronto Research Chemicals	M732752
Myc-DDK-tagged Human SLC10A1 ORF clone	ORIGENE	RC210241
Myc-DDK-tagged Mouse Slc10a1 cDNA clone	ORIGENE	MR205550
Human IBAT	ORIGENE	NM_000452
Mouse IBAT	ORIGENE	NM_011388

10.1.3 Table 3: Antibodies used for immunohistochemistry.

Target	**Primary antibodies**		**Secondary antibodies**	
	Antibody	**Dilution**	**Antibody**	**Dilution**
Cholangiocyte	Anti-cytokeratin 19 antibody, rabbit	1:500	Ultra-Map anti rabbit HRP	Automatic Discovery Ready to use
Bile canaliculi	Recombinant anti-CD13 antibody, rabbit	1:16000	Ultra-Map anti rabbit HRP	
Leukocytes	Anti-CD45 antibody, rat	1:400	Omni-Map anti rat HRP	
Endothelial cells	Anti-MECA-32 antibody, rat	1:250	Ultra-Map anti rat HRP	
ASBT	Anti-ASBT antibody, goat	1:500	Ultra-Map anti goat HRP	
ASBT	Anti-ASBT antibody, rabbit	1:50	Ultra-Map anti rabbit HRP	
AQP1	Anti-AQP1 antibody, rabbit	1:10000	Ultra-Map anti rabbit HRP	
TSC	Anti-TSC antibody, rabbit	1:2000	Ultra-Map anti rabbit HRP	

10.1.4 Table 4 : Fluorescent markers and functional dyes used in the study.

Fluorescent marker	**Marker for**	**Dose [mg/kg]**	**Vehicle**	**Two-photon excitation range [nm]**
Hoechst 33258	Nuclei	5	PBS	700-800
TMRE	mitochondrial membrane potential	0.96	Methanol: PBS (1:1)	740-820
Cholyl-lysyl-fluorescein	Bile acid analogue	1	PBS	740-820

2',7'Dichlorofluorescein diacetate	Oxidative stress	0.5	DMSO	900-950
SYTOX green	Cell death	1.2	DMSO: PBS (1:100)	900-950
Fluorescein-coupled TCA	Bile acid analogue	1	PBS	740-820
Fluorescent marker	**Marker for**	**Dose [mg/kg]**	**Vehicle**	**Confocal excitation range [nm]**
Anti-CD31	Endothelial cells	0.08	PBS	381 - 459
Evans blue	Capillary leakiness	0.5	PBS	646 - 709
Rhodamine123	Mitochondrial membrane potential	0.8	Methanol: PBS (1:1)	498 - 532

10.1.5 Table 5: Sequence based reagents: TaqMan gene assays.

Gene	**TaqMan Assay ID**	**Supplier**
Abcb11	Mm00445168_m1	Thermo Fisher Scientific
Abcc2	Mm00496899_m1	Thermo Fisher Scientific
Abcc3	Mm00551550_m1	Thermo Fisher Scientific
Abcc4	Mm01226381_m1	Thermo Fisher Scientific
Cyp7a1	Mm00484150_m1	Thermo Fisher Scientific
Egr1	Mm00656724_m1	Thermo Fisher Scientific
GAPDH	Mm99999915_g1	Thermo Fisher Scientific
Slc1a2	Mm01275814_m1	Thermo Fisher Scientific
Slc10a1	Mm00441421_m1	Thermo Fisher Scientific
Slc10a2	Mm00488258_m1	Thermo Fisher Scientific
Slco1b2	Mm00451510_m1	Thermo Fisher Scientific
Slc51a	Mm00521530_m1	Thermo Fisher Scientific

10.1.6 Table 6: List of bile acids and internal standards with MRM transitions and MS parameters for quantification by LC-MS-MS.

Analyte	Internal Standard	Precursor Ion	Product Ion	CE (V)
ω-Muricholate (ωMCA)	d5-ωMCA	407.3	407.3	0
α-Muricholate (αMCA)	d5-αMCA	407.3	407.3	0
ß-Muricholate (ßMCA)	d5-βMCA	407.3	407.3	0
Tauro-α/ß-muricholate (TαßMCA)	d4-TßMCA	514.3	80.1	74
Tauro-ω-muricholate (TωMCA)	d4-TßMCA	514.3	80.1	74
7-Dehydrocholate (7-DHCA)	d4-TßMCA	405.3	405.3	38
Hyodesoxycholate (HDCA)	d4-UDCA	391.3	391.3	0
Cholate (CA)	d4-CA	407.3	343.4	36
Glycocholate (GCA)	d4-GCA	464.3	74.0	40
Taurocholate (TCA)	d4-TCA	514.3	80.1	74
Chenodeoxycholate (CDCA)	d4-CDCA	391.3	391.3	0
Taurochenodeoxycholate (TCDCA)	d4-TCDCA	498.3	80	80
Deoxycholate (DCA)	d4-DCA	391.3	345.3	32
Taurodeoxycholate (TDCA)	d4-TDCA	498.3	80.1	78
Ursodeoxycholate (UDCA)	d4-UDCA	391.3	391.3	0
Tauroursodeoxycholate (TUDCA)	d4-TUDCA	498.3	80.0	74
Lithocholate (LCA)	d5-LCA	375.3	375.3	0
Taurolithocholate (TLCA)	d4-TLCA	482.3	80.1	78
Cholic acid sulfate (CA-S)	d4-CA-S	487.2	96.9	58
Taurocholic acid sulfate (TCA-S)	d4-TCA-S	594.2	514.3	32
Internal Standard				
d5-ω-Muricholate (d5-ωMCA)		413.3	413.3	0
d5-α-Muricholate (d5-αMCA)		413.3	413.3	0
d5-ß-Muricholate (d5-ßMCA)		413.3	413.3	0
d4-Tauro-ß-muricholate (d4-TMCA)		518.3	80.1	74
d4-Cholate (d4-CA)		411.3	347.2	40
d4-Glycocholate (d4-GCA)		468.3	74.0	40
d4-Taurocholate (d4-TCA)		518.3	80.1	74
d4-Chenodeoxycholate (d4-CDCA)		395.3	395.3	0
d4-Taurochenodeoxycholate (d4-TCDCA)		502.3	80.0	86
d4-Deoxycholate (d4-DCA)		395.3	395.3	38
d4-Taurodeoxycholate (d4-TDCA)		502.3	80.0	82
d4-Ursodeoxycholate (d4-UDCA)		395.3	395.3	0
d4-Tauroursodeoxycholate (d4-TUDCA)		502.3	80.0	74
d5-Lithocholate (d5-LCA)		380.3	380.3	0
d4-Taurolithocholate (d4-TLCA)		486.3	80.1	90

d4-Cholic acid sulfate (d4-CA-S)		491.3	98.0	58
d4-Taurocholic acid sulfate (d4-TCA-S)		598.3	518.3	32

10.1.7 Table 7: Software.

Software name	Manufacturer	Version
GraphPad Prism 9 Software	GraphPad	9.5.0
Ilastik	ilastik Team	1.3.3post1
Zen	Carl-Zeiss	
R	R Development Core Team	4.2.2
Salmon	Salmon Software	1.4.1
Scils Lab MVS	Bruker Daltonics	2021 c
Skyline Daily	University of Washington	23.0.9
TiQuant	Hoehme group	2.0
QuestTM	Thermo Scientific	
QuPath	QuPath team	0.4.2
CellX	Hoehme group	7.3

10.2 Methods

10.2.1 Animals and bile duct ligation

Eight-to-10-week-old male and female C57BL/6N (Janvier Labs, France) or Cyp2c70 -/- and corresponding C57BL/6J wildtype (Dawson, Karpen Lab) mice were used. The mice were housed at standard environmental conditions with free access to water, and ad libitum feeding with Ssniff R/M-H, 10 mm standard diet (Ssniff, Soest, Germany). All experiments were approved by the local animal welfare committee (LANUV, North Rhine-Westphalia, Germany, application number: 81-02.04.2022.A286). To induce obstructive cholestasis the extrahepatic common bile duct was ligated at a position between the gallbladder and the duodenum, as previously described [2, 3].

10.2.2 Preparation and application of AS0369

A stock formulation was prepared by dissolving AS0369 in the vehicle solution (0.5% methyl cellulose and 0.06% Tween 80) followed by sonication and vortexing for several minutes until a uniform suspension was obtained. The different doses of 15, 30, 60 and 120 mg/kg b.w. were prepared by diluting the stock formulation accordingly in the vehicle solution. The ASBT inhibitor (AS0369) and the vehicle were administered orally by gavage twice per day with an application volume of 4 mL/kg b.w.

10.2.3 Sample collection and processing

10.2.3.1 Blood sampling

Heart blood samples were collected from anaesthetised mice in syringes precoated with disodium ethylenediaminetetraacetic acid (EDTA), as previously described [3]. After centrifugation, plasma was separated and stored at -80 °C until used for analysis.

10.2.3.2 Tissue sample collection

Prior to tissue collection, transcardial perfusion with PBS was performed to wash out the remaining blood.

10.2.3.3 Liver tissue sample collection

The whole liver was excised. Samples of 5 × 7 mm diameter were collected from the left liver lobe and fixed for two days in 4% paraformaldehyde (PFA) followed by washing in PBS and embedding in paraffin. In addition, samples of 5 × 7 mm diameter were collected from the left liver lobe, immediately frozen in liquid nitrogen and stored at -80 °C until analysis by MALDI-MSI. The remaining liver tissue was snap-frozen by freeze-clamping and milling in liquid nitrogen and subsequently stored at -80 °C until RNA isolation.

10.2.3.4 Kidney tissue sample collection

Both the left and the right kidneys were excised. After removal of the surrounding capsule, the right kidney was divided longitudinally into two halves: one half was fixed in 4% PFA and embedded in paraffin, and the other half was immediately frozen in liquid nitrogen and stored at -80 °C until analysis by MALDI-MSI. The left kidney was snap-frozen by freeze-clamping and milling in liquid nitrogen and subsequently stored at -80 °C until RNA isolation.

10.2.3.5 Urine sample collection

24-hour urine samples were collected in metabolic cages as previously described [14]. Spontaneous urine samples were collected from female mice using a urinary bladder canula (25 gauge; SAI Infusion Technologies) as previously described [15].

10.2.3.6 Bile sample collection

Bile samples were collected from the gallbladder.

10.2.4 Biochemical analysis

Creatinine, urea, total bilirubin, and direct bilirubin from plasma and/or urine were determined using a C400 clinical chemistry analyzer (Pentra C400 Option I.S.E, HORIBA ABX SAS, Montpellier, France). Biomarkers of liver damage (alanine transaminase,

aspartate transaminase and alkaline phosphatase) were measured in mouse plasma using the Piccolo Xpress Chemistry Analyzer (Hitado, Germany) and the Piccolo General Chemistry 13 Panel Kit. The plasma samples from control and BDL mice were diluted 1:1 or 1:5 in normal mouse serum (S7273 -50ML, Sigma-Aldrich), respectively, prior to analysis. AS0369 was analyzed in plasma and tissue samples using LC-MS/MS.

10.2.5 Quantification of bile acids with LC-MS/MS

Bile acid concentrations in plasma, urine, bile, liver tissue and kidney tissue were determined by negative electrospray (ESI) liquid chromatography tandem mass spectrometry (LC- MS/MS) in multiple-reaction-monitoring (MRM) mode on an Agilent 6495B triple quadrupole mass spectrometer (Agilent, Germany) coupled to an Agilent Infinity II HPLC system as described previously [2]. Briefly, frozen tissue samples were homogenized in methanol: water 1:1 (v/v) in a FastPrep® 24 homogenizer (MP Biomedicals, Santa Ana, USA) to a final concentration of 40 mg wet tissue/ml as described previously [4]. Aliquots of 5 µL of plasma or diluted bile (1:100), 30 µl of tissue homogenate, or 2 µl of urine were spiked with internal standard solution followed by protein precipitation with methanol and centrifugation. The supernatant was used for LC MS/MS analysis. Urine samples above the calibration range were diluted with water 1:10 v/v to 1:50 v/v. LC-MS/MS parameters for measurement of bile acids and the internal standards are summarized in Table 6. Protein determination in tissue homogenates was performed with the PierceTM BCA protein assay kit.

10.2.6 ELISA assays

10.2.6.1 Determination of NGAL concentrations

Concentrations of NGAL/Lcn- 2 were determined in mouse urine and plasma using the Mouse Lipocalin-2/NGAL DuoSet ELISA kit plus the DuoSet ELISA Ancillary Reagent Kit 2 from R&D systems (DY1857 and DY008) according to the manufacturer's protocol. The concentrations of NGAL/Lcn-2 in human serum were determined using the Human Lipocalin-2/NGAL Quantikine ELISA kit from R&D Systems (DLCN20) following the manufacturer's protocol. The optical density of the color-forming TMB substrate from both assays was measured at 450 nm using a microplate reader (Infinite M200 Pro, Tecan) and the concentration of NGAL/Lcn-2 of each sample was calculated from the standard curve.

10.2.6.2 Determination of Kim-1 concentrations

Concentrations of Kim-1 were determined in mouse urine and plasma using the Mouse KIM 1 ELISA Kit from Abcam (ab213477) according to the manufacturer's protocol. The concentrations of Kim-1 in human serum were determined using the Human Serum TIM-1/KIM-1 HAVCR Quantikine ELISA kit from R&D Systems (DSKM100). The optical density of the color-forming TMB substrate from both assays

was measured at 450 nm using a microplate reader (Infinite M200 Pro, Tecan) and the concentration of KIM-1 of each sample was calculated from the standard curve.

10.2.6.3 Determination of cystatin C concentrations

Concentrations of Cystatin C were determined in plasma using the Mouse Cystatin C ELISA Kit from Abcam (ab201280) according to manufacturer's protocol. For human serum samples the Human Cystatin C Quantikine ELISA kit from R&D Systems (DSCTC0) was used following the manufacturer's instructions. The optical density of the color forming TMB substrate from both assays was measured at 450 nm using a microplate reader (Infinite M200 Pro, Tecan) and the concentration of Cystatin C of each sample was calculated from the standard curve.

10.2.7 Histopathology

Hematoxylin and eosin (H&E) and Sirius red staining were performed in 4 µm thick PFA (4%)-fixed paraffin-embedded liver and kidney tissue sections. Hematoxylin staining was performed using the Discovery Ultra Automated Slide Preparation System, as previously described [5]. Eosin staining was performed according to a standard protocol [8]. Sirius red staining was done using a commercially available kit, according to the manufacturer's instructions. To visualize bilirubin casts in kidney tissues, Hall's staining was performed using 4 µm-thick PFA (4%)-fixed paraffin-embedded kidney tissue sections using a commercially available kit (StatLab), according to the manufacturer's instructions. The principle of this staining technique is that oxidation of bilirubin in acidic medium results in formation of biliverdin which can be distinguished by its green color [6]; the cell cytoplasm stains yellow, while collagen appears red.

10.2.8 Immunohistochemistry

Immunostainings were performed using 4 µm-thick PFA (4%)- fixed paraffin-embedded liver and/or kidney tissue sections using the Discovery Ultra Automated Slide Preparation System, as previously described [7, 16]. Antibodies and their concentrations are given in Table 3. Nuclei were visualized by counter-staining with Mayer's hematoxylin. Whole slide scanning was performed using the Axio Scan.Z1.

10.2.9 Image analysis

High-resolution whole slide scans (~1 Gpixel each) were preprocessed using CLAHE, a widely used image processing technique improving the contrast in images by stretching the intensity distribution of the pixels [9] implemented in the software TiQuant [17]. The resulting data was segmented in a two-step process, starting with a Random Forest classification [18] to distinguish tissue and non-tissue regions, and a region of interest within the tissue typically emphasized by staining. Random forest classification is an

accurate and robust machine learning technique, whereby features are chosen based on the highest information gain. The model to classify each pixel was manually trained by a subset of images for each staining but was applied to all images using the software QuPath [19]. In a second segmentation step, we refined the segmentation result using the TiQuant software by a semantically informed application of morphological operators that considered known structure shape, size, and localization in tissue to further improve the segmentation accuracy. The diameter of the bile canaliculi network was measured using a pruned skeletonization of the bile network segmentation by averaging the diameter of the maximally inscribed spheres along the skeleton [20].

10.2.10 Intravital imaging

Functional intravital imaging of livers and kidneys of anesthetised mice was performed using an inverted two-photon microscope LSM MP7 or LSM880 (Zeiss, Germany), as previously described [7, 21, 22]. Before recording, the mice received bolus tail vein injections of Hoechst 33258 (nuclear marker), TMRE (mitochondrial membrane potential marker), SYTOX green (cell death marker), 2',7'dichlorofluorescein diacetate (H_2DCFDA; a non-fluorescent probe that passes passively into cells, de- esterified intracellularly, and turns to the green-fluorescent dichlorofluorescein (DCF) upon oxidation) and/or anti-CD31 antibody (endothelial cell marker) (Table 4). To allow administration of further functional dyes/markers while recording, a mouse catheter (SAI- infusion, IL, USA) was fixed in the tail vein. To analyse bile flux in the liver and kidneys, fluorescently labelled taurocholic acid (TCA) or the bile acid analogue CLF was administered via the tail vein catheter as a bolus (Table 4) [7]. To check the integrity of peritubular capillaries, a bolus of the leakiness marker Evans blue [23] was administered and intravital recording was done using the LSM880 confocal microscope (Table 4). At least three mice were analysed for each of the experimental scenarios shown in the result section.

10.2.11 Video analysis

As preprocessing for quantification of intravital imaging, rigid-body registration was performed using StackReg [24] to compensate for tissue motion (e.g., due to respiration and heartbeat) in the time series. Two-dimensional projections were created from these stabilized videos by z-projection using the average, maximum, and standard deviation operators. The autocontext segmentation workflow of the ilastik interactive image segmentation software (version 1.3.3post1) [24] was used to segment the tissue compartments in these 2D projections. The analyzed compartments were peritubular capillaries and TMRE positive tubular epithelial cells in the kidney time series showing TCA uptake, and capillaries and interstitium in the time series visualizing Evans blue dynamics. In the liver, the considered compartments were sinusoidal capillaries, hepatocytes, and bile canaliculi showing TCA flux. Mean raw TCA / Evans blue intensities were measured per compartment and frame. Additionally, the mean TCA signal in the TMRE positive cell compartment was measured per tubule, and tubules were

subsequently separated into two groups based on their maximum mean TCA intensity over time using k-means clustering.

10.2.12 MALDI-MS-Imaging

Frozen specimens were sectioned serially into 5-µm-thick tissue sections using a Leica CM 3050 S cryostat. The sections were thaw-mounted on IntelliSlides (Bruker Daltonics, Bremen, Germany), dried in a desiccator, and stored at - 20 °C until analysis. The tissue sections were sprayed (4 layers) with 5 mg/mL 2- mercaptobenzothiazole in acetone/water (5:1) using an HTX Imaging-Sprayer (HTX Technologies LLC, Chapel Hill, NC, USA) at 65 °C at 10 psi nitrogen. The flow was 120 µL/min. MALDI measurements were accomplished on MS1-level in negative mode with a tims TOF FleX without ion-mobility separation in a mass range from 85-800 m/z and calibrated internally using the 2-mercaptobenzothiazole matrix peak and taurocholate. Data was interpreted using Scils Lab MVS, Version 2021 c.

10.2.13 Gene expression analysis

RNA isolation and cDNA synthesis. Liver and kidney RNA was isolated from milled frozen tissue using the RNeasy Mini Kit, according to the manufacturer's protocol. cDNA synthesis was performed from 2 µg of isolated RNA using the High-Capacity cDNA Reverse Transcription Kit. qRT-PCR assays. qRT-PCR analyses were performed with cDNA using TaqMan 7500 Real-Time PCR, TaqMan universal PCR Master Mix, and TaqMan gene expression assays (Table 5) (ThermoFisher Scientifics, Oberhausen, Germany). The gene expression values were normalized to the housekeeping gene GAPDH and further calculated with the ΔΔCt method. The values were expressed as fold changes over control samples.

10.2.14 RNA-sequencing and bioinformatics

RNA-seq of liver and kidney tissues was performed as previously described [25]. Transcript quantification of RNA-seq data and mapping of the FASTQ files were performed with the software Salmon, version 1.4.1, using the option 'partial alignment' and the online provided decoy-aware index for the mouse genome [26]. Further analyses were performed with R, version 4.2.2 [27]. To summarize the transcript reads on gene level, the R package tximeta was used [28]. For pre-filtering, genes with less than 10 reads across all mice (18,872) were removed, so that 16,855 genes remained for further analyses. The following analyses were performed separately for kidney and liver samples. Differential gene expression analysis was calculated using the R package DESeq2 [29]. A general linear model with one factor and levels "sham vehicle", "BDL vehicle" and "AS0369 BDL" was fitted to calculate differentially expressed genes (DEGs). DEGs were then calculated for the comparisons "sham vehicle vs. BDL vehicle" and "sham vehicle vs AS0369 BDL". For more reliable effect estimates, adaptive shrinkage was applied [30].

This leads to shrinkage of log-2 transformed fold-changes (log 2(FCs)) towards zero if expression changes are mostly due to noise, whereas relevant log 2(FCs) are preserved. For each comparison, a gene was considered to be differentially expressed if the effect size fulfils log 2(FC) > log 2(1.5) for upregulation (log 2(FC) < -log 2(1.5) for downregulation) and the estimate is significantly different from zero (i.e., no effect) with a false discovery rate (FDR)-adjusted p-value p adj < 0.05. DiPa (Nell) plots were generated as recently described [31]. Enrichment analysis for biological processes gene ontology (GO) terms was applied separately for up and down regulated genes for the above-described comparison “sham vehicle vs. BDL vehicle” and two of the areas defined in the differentiation pattern (DiPa) plot (Fig 7C, I) using the R package topGO [32]. P-values of GO groups were FDR-adjusted and considered significant if the adjusted p-value was smaller than 0.05. To compare DEGs between liver and kidney, Venn diagrams were used, and the corresponding overlap ratios were calculated as previously described [33]. The overlap ratio between two sets of genes indicates the degree of overrepresentation in the overlap of the two gene sets compared to a random situation. If the ratio is higher than 1, the number of genes in the overlap is higher than randomly expected. The overlap ratio is calculated as follows: If nuniverse is the total number of analyzed genes, n 1 and n 2 are the numbers of DEGs in gene set 1 and 2, and O is the number of genes present in both sets, then: Overlap ratio = (O nuniverse) / (n 1 n 2).

10.2.15 Statistical analysis

Data were analyzed using Prism software (GraphPad Prism 9.5.0 Software, Inc., La Jolla, CA, USA). Statistical group comparisons were done using Tukey’s, Dunn's, or Šídák's multiple comparisons test, or unpaired t-test, as indicated in the figure legends. Statistical analysis of genome-wide gene expression was done using R (version 4.2.2) [23].

11 Results

11.1 Establishment of a cholestatic mouse model

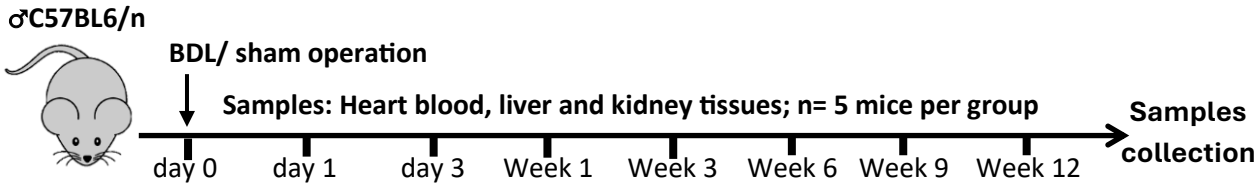

Fig. 3: Experimental schedule illustrating different steps of the experiment that have been planned. After BDL and sham operations, different samples are collected from the male C57BL6/n mice. These samples are stored safely for later analysis.

To study the adverse consequences of increased bile acid concentrations in the systemic circulation, I established an obstructive cholestatic mouse model. The currently most applied mouse model induces cholestasis by surgical ligation of the common bile duct. I established the procedure introducing the ligation between the gallbladder and the duodenum. Mice that underwent surgery without ligation of the bile duct were as controls, further named “sham”. After following the experiment setting described in figure 3, mice are sacrificed, and organs are collected to continue with tissue analysis. Since the gallbladder is located upstream of the ligation the obstruction caused a strong dilatation of the gallbladder three days after ligation which continued up to week 12 (Fig. 4). Sometimes the increased gallbladder even developed one or two additional branches.

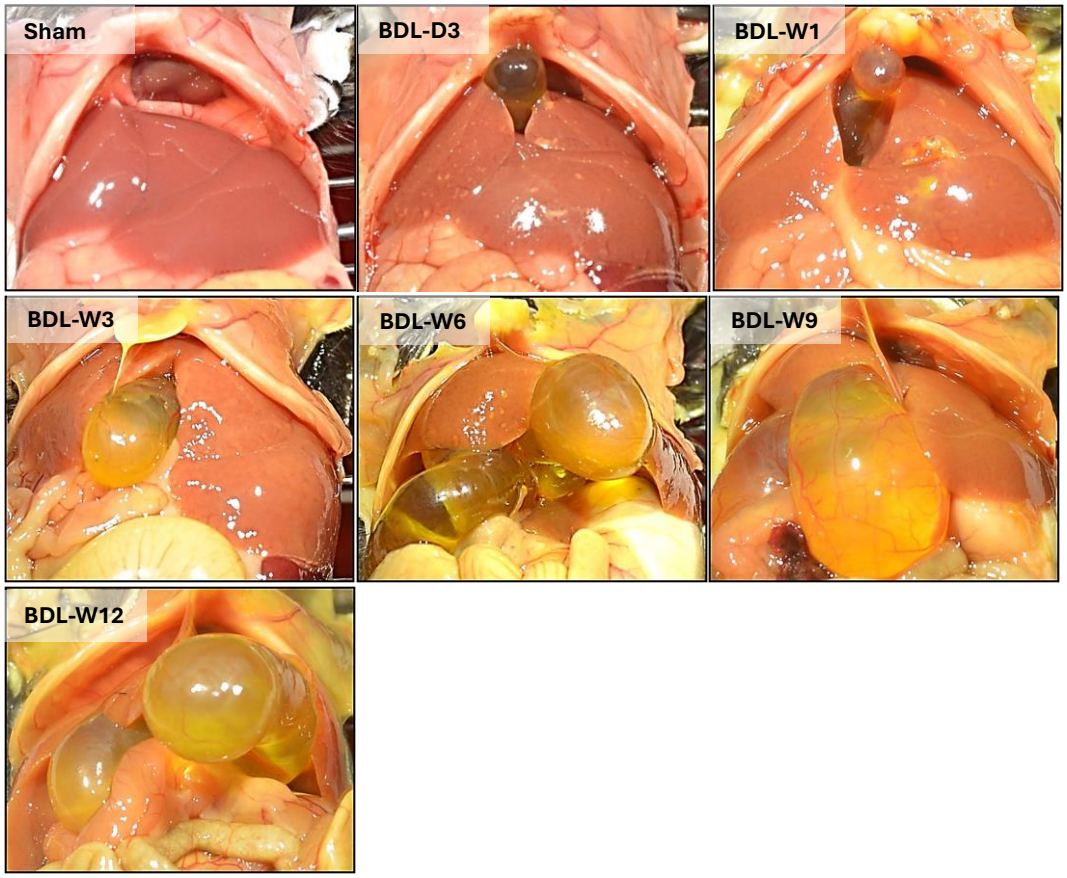

Fig. 4: Morphology of the gallbladder after bile duct ligation. The findings reveal a clear dilatation of the gallbladder, accompanied by an increase in bile volume.

11.2 Clinical chemistry after bile duct ligation

The transaminases ALT and AST were analysed, because they represent accepted markers of liver tissue damage. Initially (day 1), a very strong increase in ALT and AST was observed (Fig. 5). Interestingly, the blood concentrations of ALT and AST decreased later, suggesting an adaptation to the cholestatic situation. Total bilirubin increased and reached a plateau at week 1, while the cholangiocytes damage marker ALP increased continuously, suggesting the occurrence of chronic damage to the biliary system (Fig.5).

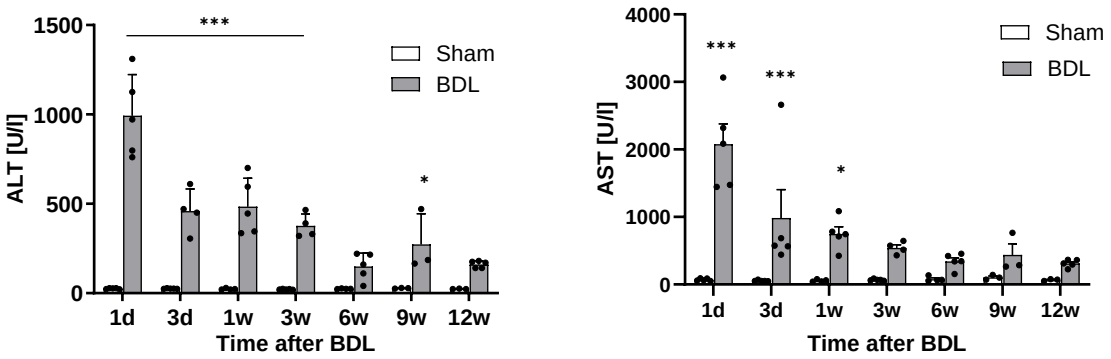

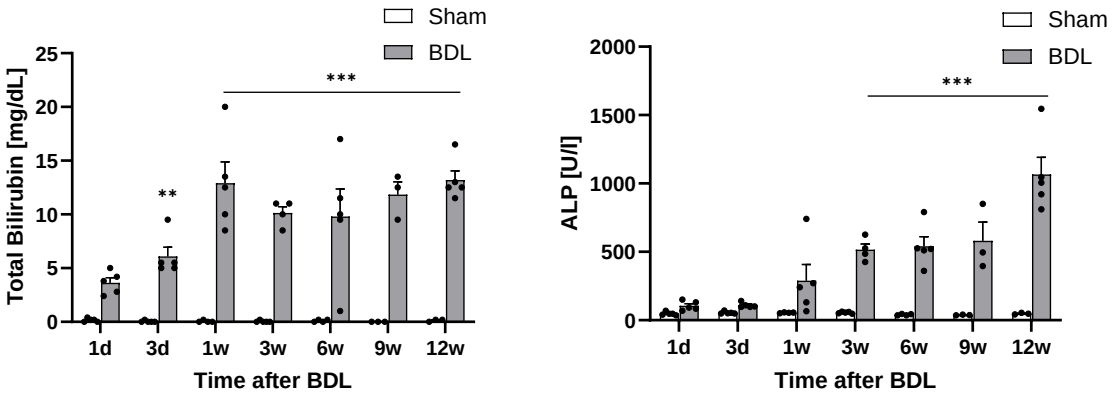

Fig. 5: Clinical chemistry in the plasma of mice after bile duct ligation. Each dot represents a mouse. **p <0.01; ***p <0.001 compared to sham day 1, Unpaired t test. The data are from male mice.

11.3 Histological examination after BDL

To analyse the histological modifications due to BDL, I analysed tissue sections at various time points after BDL or sham surgery. As a first staining H&E was applied (Fig. 6). This analysis showed strong and progressive tissue damage in the periportal region of liver lobules.

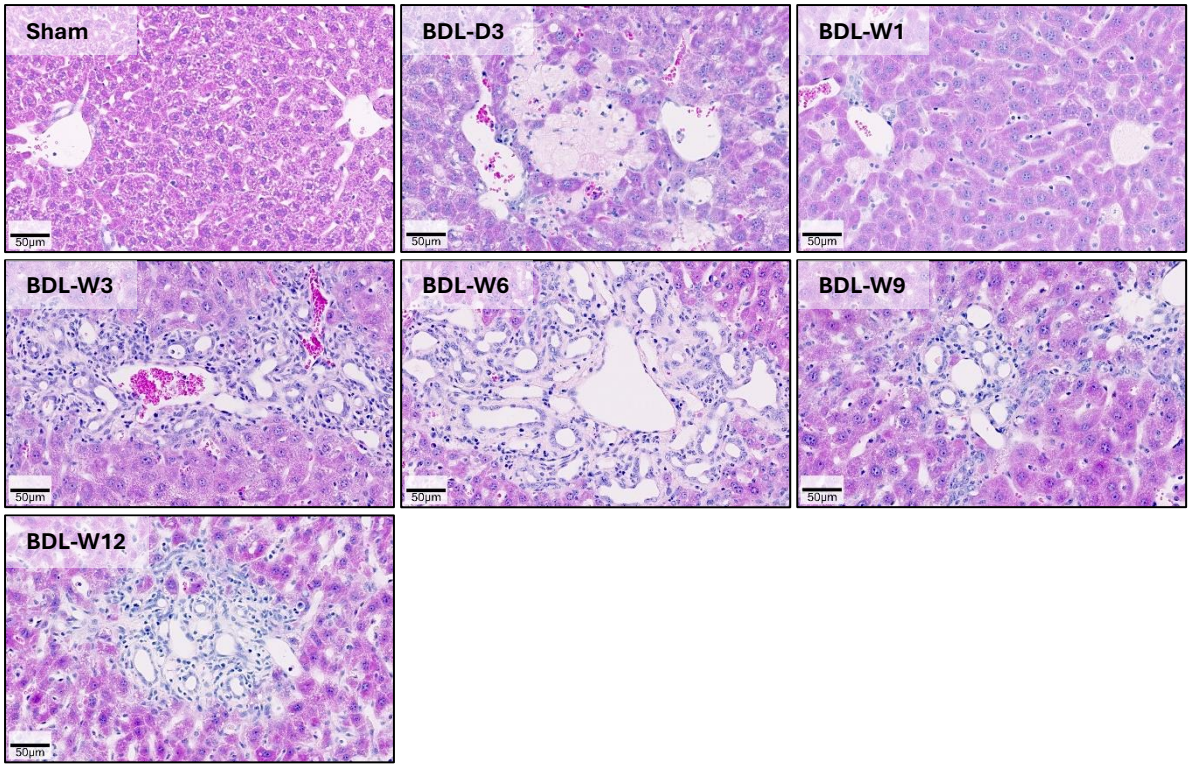

Fig. 6: H&E staining of liver tissue at various time points after BDL showing an increased damage in the portal area in the liver tissues. Scale bars: 50 µm. D: day; W: week

11.4 Histochemical examination after BDL

Histochemical examination of the immune cells after BDL demonstrated a significant increase in immune response. The CD45 staining of BDL-livers showed time-dependently increasing infiltration of leukocytes in the liver tissue and a clear accumulation of positive cells in the damaged portal area (Fig. 7). To specify the damage area, a CK19 staining (marker for cholangiocytes) was performed. The results show a clear ductular reaction at week one, which increased up to week 12 after BDL (Fig. 8). To examine fibrosis, collagen was stained with the Sirius red kit. An ascending increase in fibrosis is shown in Figure 9.

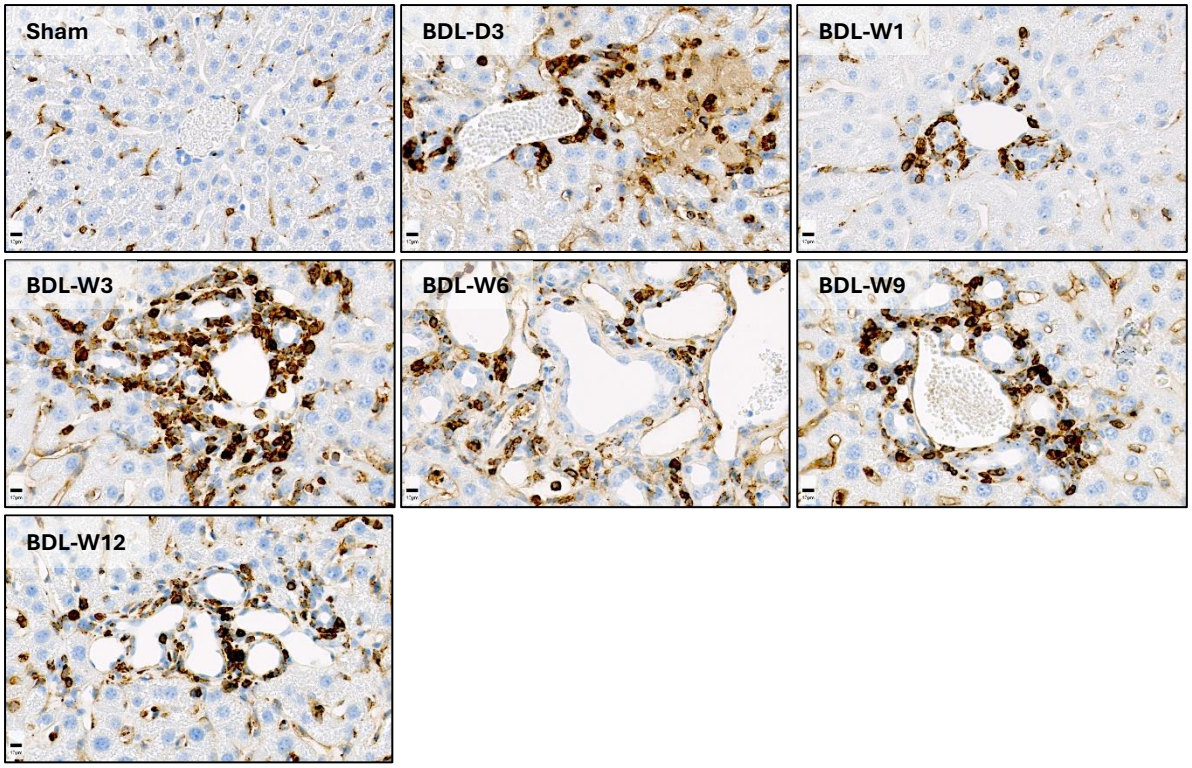

Fig. 7: Immunostaining of leukocyte (CD45) demonstrates an infiltration of immune cells in liver tissues, especially around the portal veins. Scale bars: 10 µm.

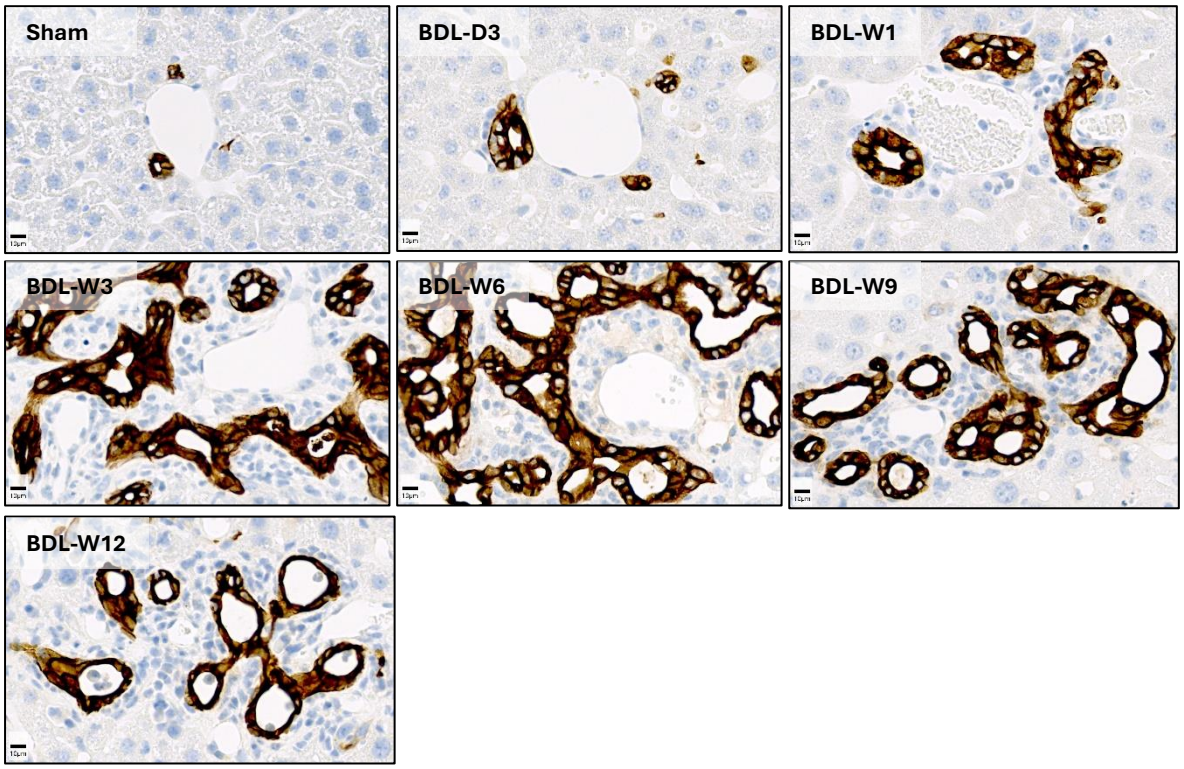

Fig. 8: Immunostaining of bile ducts (CK19) showing increasing ductular reaction in the portal area in liver tissues. Scale bars: 10 µm.

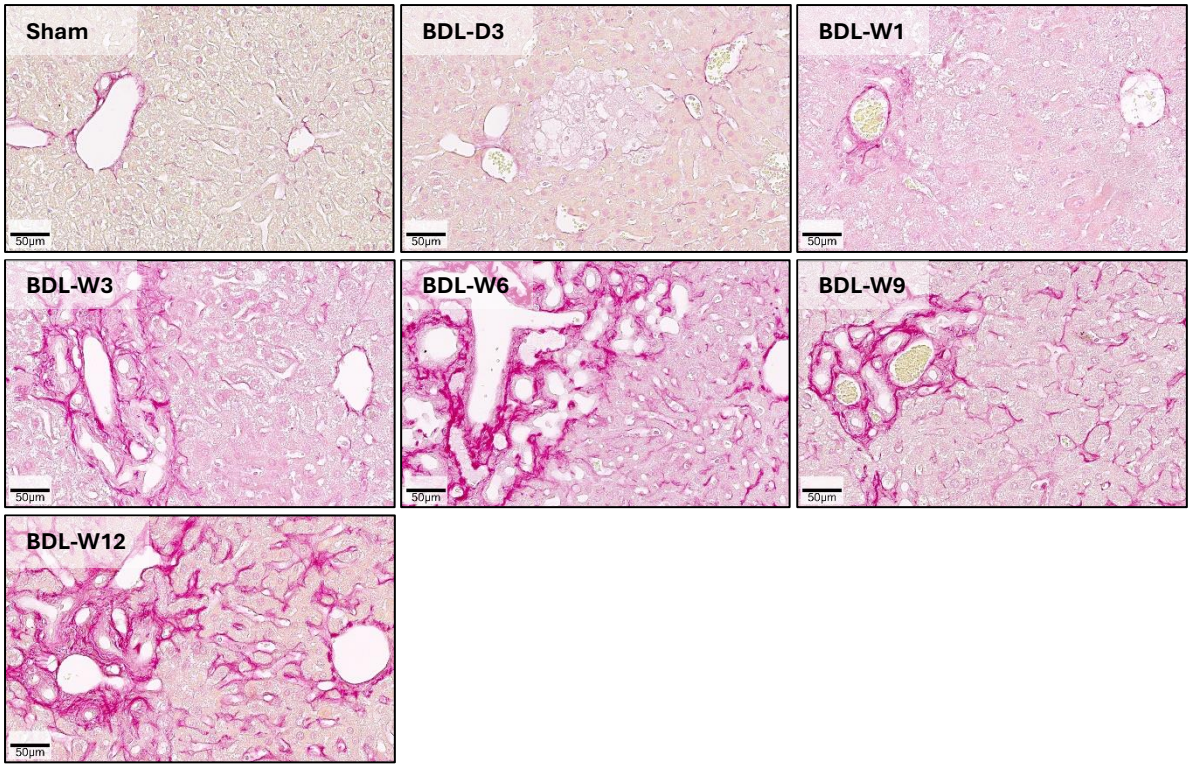

Fig. 9: Sirius Red staining showing time-dependently increasing collagen accumulation and portal fibrosis. Scale bars: 50 µm.

11.5 Intravital analysis of bile flux in the liver

To study bile flux in intact livers of anesthetised mice I used a technique of intravital two-photon microscopy. This technique allows time resolved analysis of fluorescent bile acid analogues such as fluorophore coupled TCA with a resolution of approximately 250 nm. The result of the control shows an initial appearance of the TCA signal in the blood sinusoids (Fig. 10 A). Next TCA was taken up into the hepatocytes and further secreted into the bile canaliculi. A completely different situation was seen after BDL (Fig. 10 A). The TCA signal stayed in the sinusoidal blood for the entire imaging period (2h). Only, extremely little TCA passed from sinusoidal blood into hepatocytes and the canaliculi demonstrated a very strong block of the uptake of the bile acids from blood to hepatocyte.

Quantification of the TCA signal in the three compartments, sinusoids, hepatocytes and canaliculi confirmed the observations from the intravital imaging (Fig. 10 B).

Results

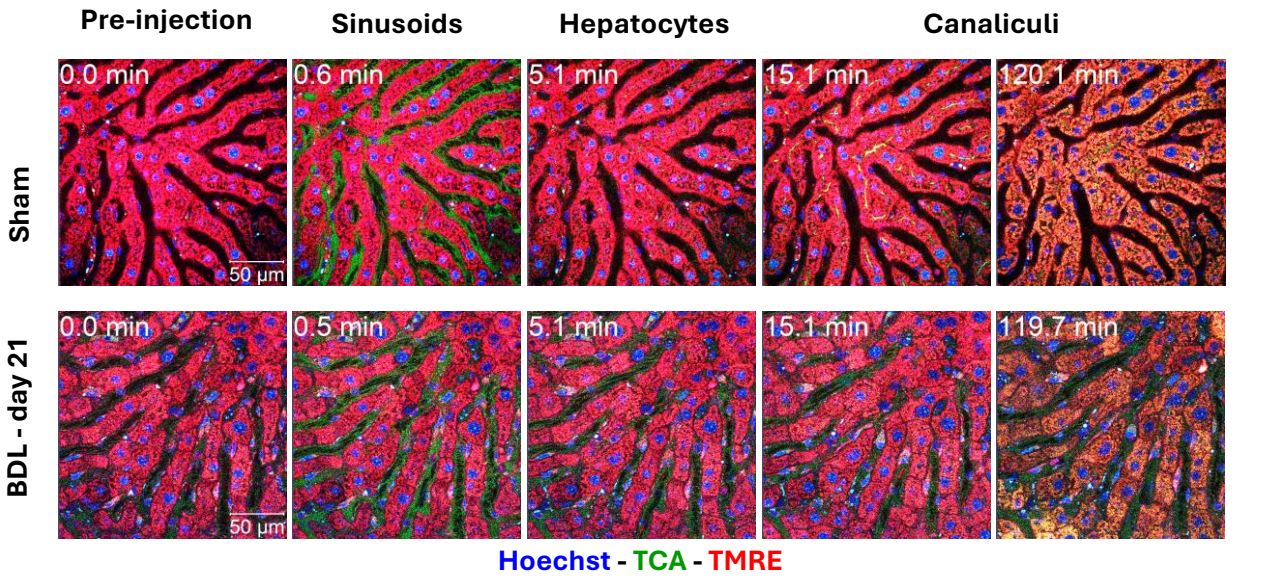

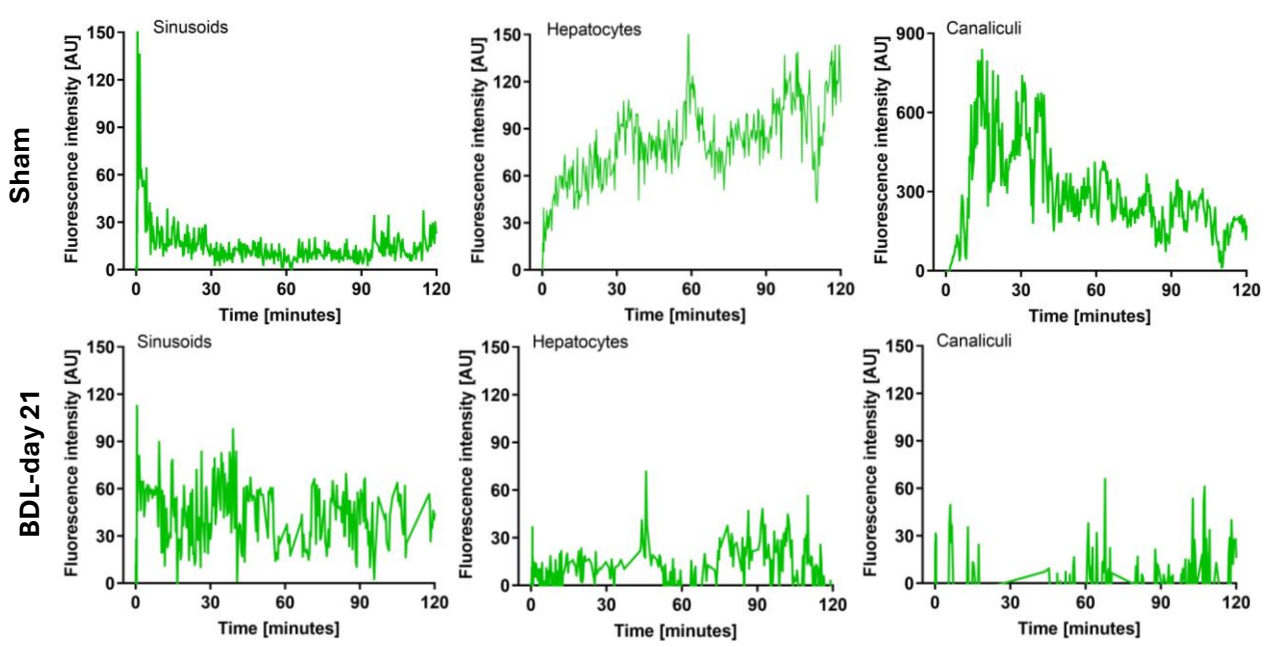

Fig. 10: Intravital imaging of bile flux in liver tissue. **A:** Images taken from intravital videos of the liver of sham controls and mice 21 days after the BDL treatment. Red: TMRE; green: TCA; blue: Hoechst. Scale bars: 50 µm. **B**: Corresponding quantifications of the intravital videos of the liver of sham controls and mice 21 days after BDL.

11.6 Intravital analysis of bile flux in the kidney

Similar as in the liver, bile flux was also analysed by intravital imaging in the kidneys (Fig. 11). Bolus injection of 1mg TCA-FITC per Kg body weight led to an only very low fluorescent signal in the renal blood capillaries (Fig. 11 A). This was in contrast to the situation after BDL, where a much stronger increase in the blood capillaries was seen (Fig. 11 A, B). The difference is due probably to the much stronger extraction by the liver from control mice compared to BDL animals. After BDL I observed a strong increase of TCA-FITC in the lumen of the renal tubules that occurred immediately after the increase in the capillaries. An interesting further observation was that subsequently TCA-FITC was absorbed into some tubular epithelial cells (Fig. 11 A).

Quantification of the segmented videos showed that only a fraction of all tubular epithelial cells enriched TCA-FITC (Fig. 11 B).

A

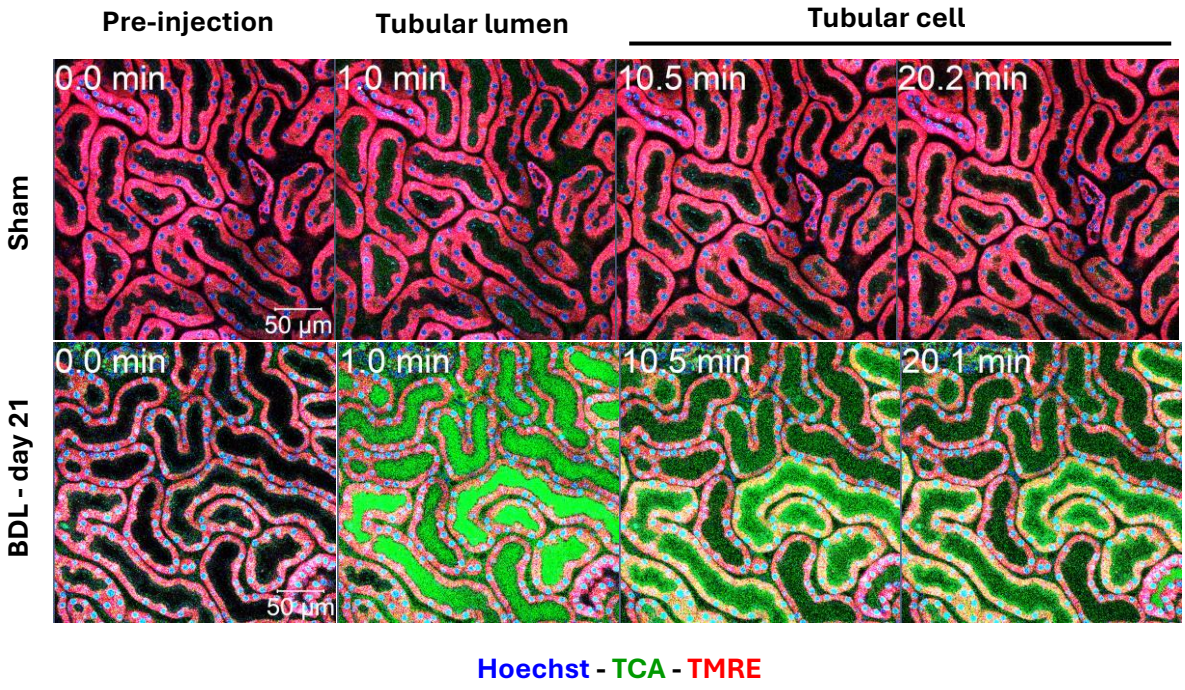

B

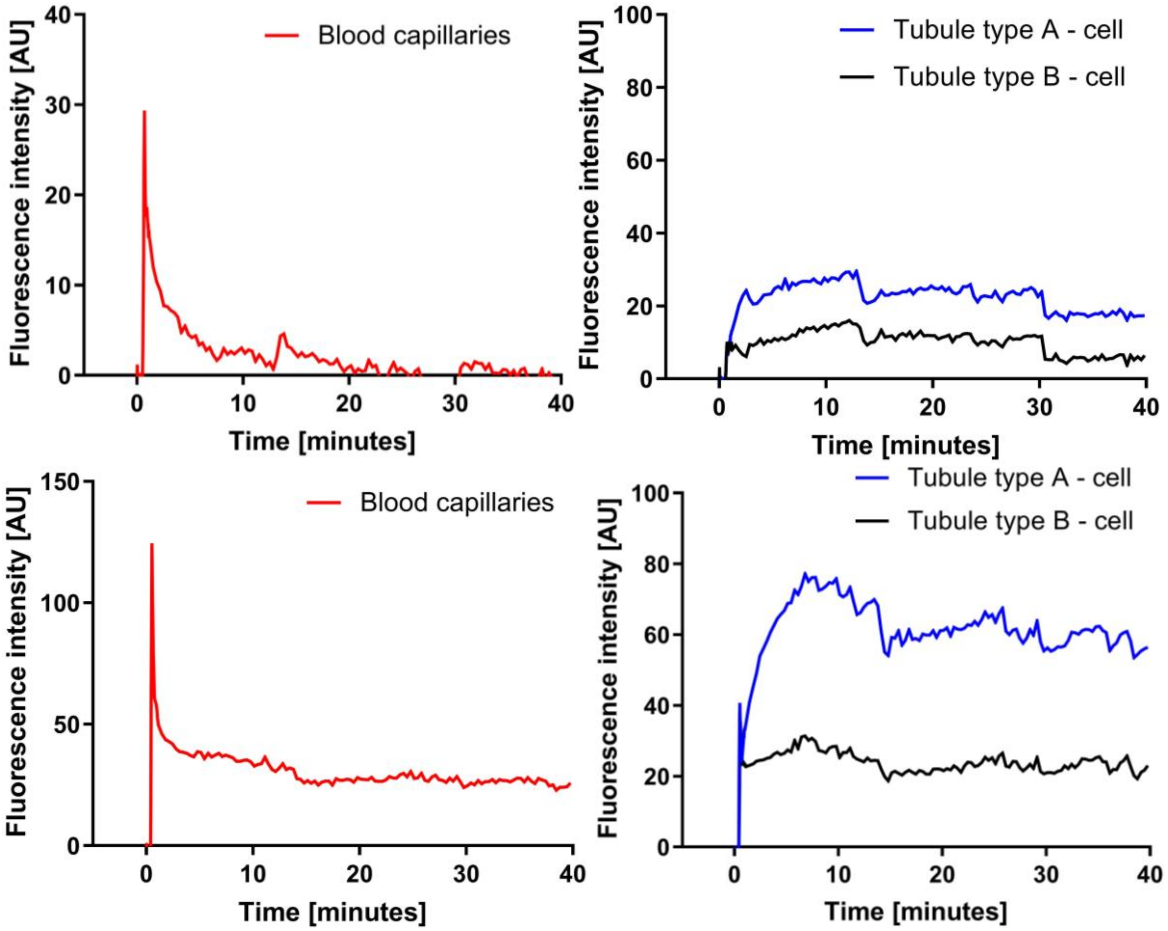

Fig. 11: Intravital imaging of bile flux in kidney tissue. **A:** Increase of TCA-FITC uptake into the proximal tubular epithelial cells after BDL. Images from intravital videos of kidney of sham controls and mice 21 days after BDL. Scale bars: 50 µm. **B**: Corresponding quantifications. Red: TMRE; green: TCA; blue: Hoechst.

11.7 Analysis of liver and renal tissue by MALDI-MSI

In the previous experiment, I analysed bile flux by a fluorescein coupled with TCA, exogenously administered bile acid. Next, I visualized the endogenous bile acids in tissue showing TCA as an example (Fig. 12). Cryosections of liver and kidney tissue were scanned one day, as well as 1, 3, 6 and 12 weeks after BDL (Fig. 12). Liver tissue showed a strong transient increase of TCA on day 1 after BDL followed by lower levels, thereafter, suggesting liver adaptation (Fig. 12). The MALDI signal was superimposed onto CK19 immunostained sections, demonstrating that the increase of the TCA signal occurred predominantly in the periportal region. The situation in the kidney was different compared to the liver, because a continuous increase of the TCA signal was obtained until the longest observation period of 12 weeks BDL (Fig. 12).

To obtain an overview, the MALDI-MSI scans of whole tissue sections are shown in Fig. 13. The upper panel shows entire sections through the left liver lobule. The lower panel shows longitudinal sections of entire kidneys. The results confirm the previous MALDI-MSI shown on Fig. 12. The later overview also shows the adaptation of the liver and illustrates the particularly high TCA signal in the renal pelvis in weeks 6 and 12.

Quantification of the TCA signal in the MALDI analysis confirmed the above tendencies (Fig. 14).

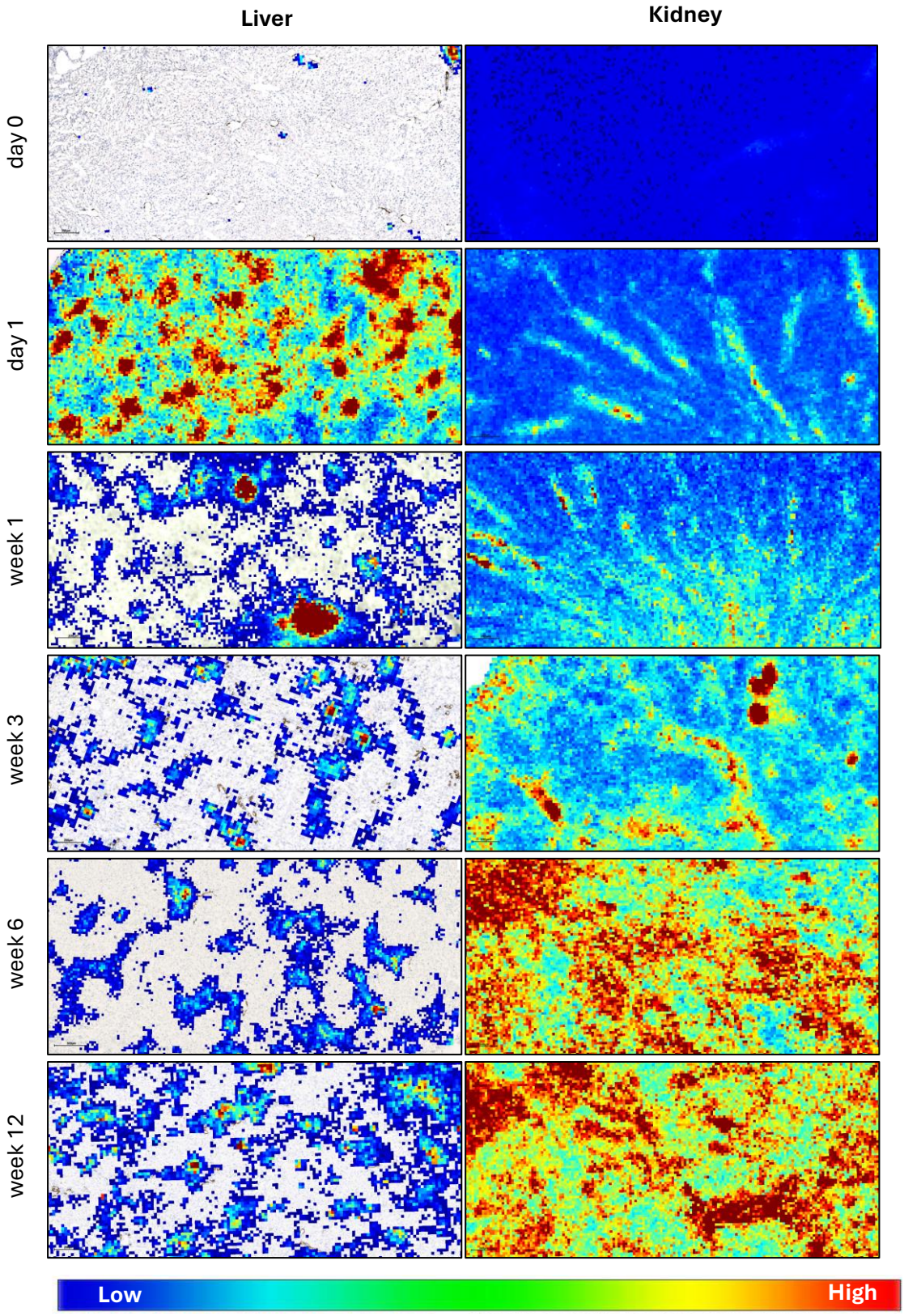

Fig. 12: MALDI-MSI images representing accumulation of taurocholate in liver and kidney tissues after BDL. After day 1 a strong accumulation of TCA in the liver tissue followed by a decrease of the signal up to week 12. In contrast, an ascending accumulation of TCA is seen in the kidney tissue. Superimposing onto adjacent liver slices stained with CK19

revealed that the accumulation mainly occurs in periportal compartments of the liver lobule. Scale bars: 200 µm.

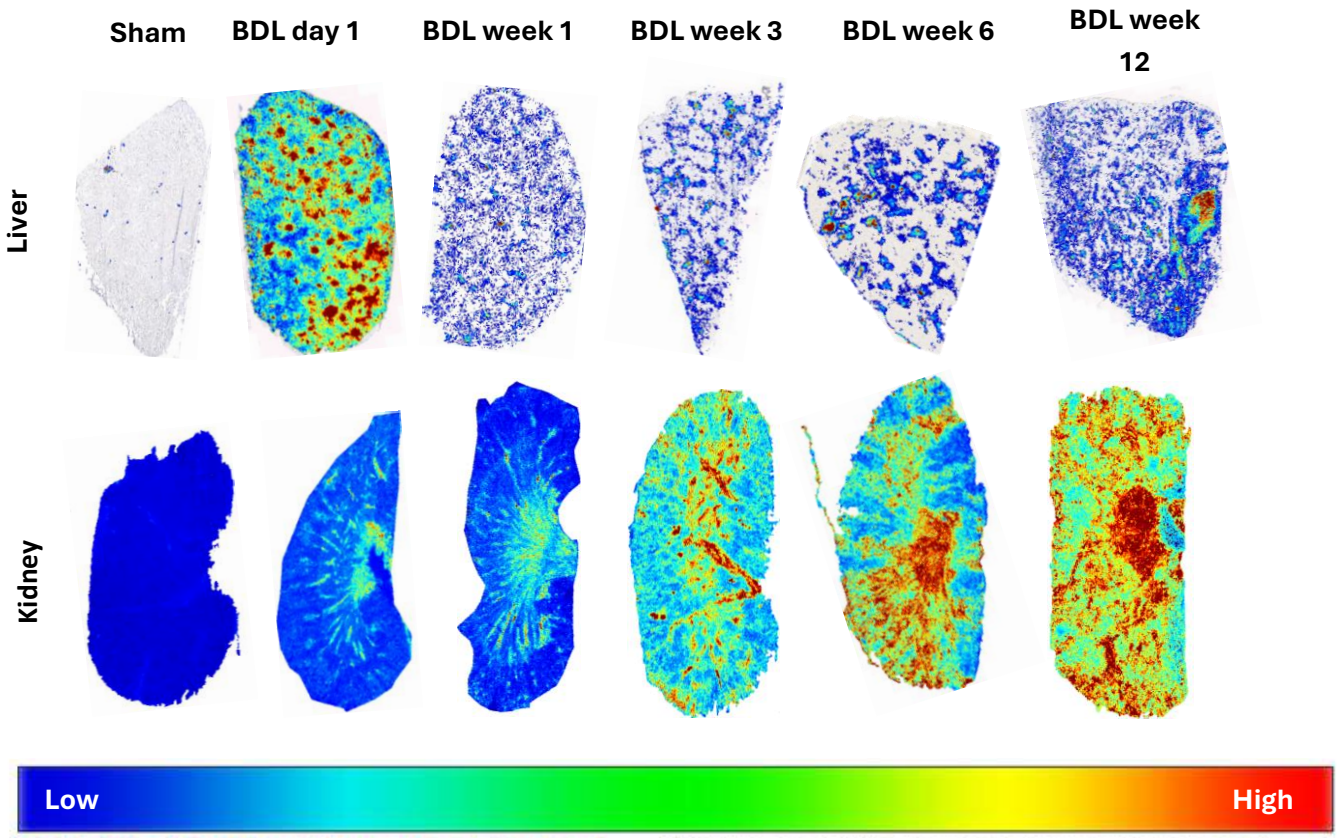

Fig. 13: Whole slide scans of MALDI-MSI images to obtain an overview of accumulation of taurocholate in liver and kidney tissues after BDL. As in the previous images, there was an accumulation of TCA in the liver tissue after day 1, followed by a decrease in signal until week 12. However, there was an accumulation of TCA in the kidney tissue.

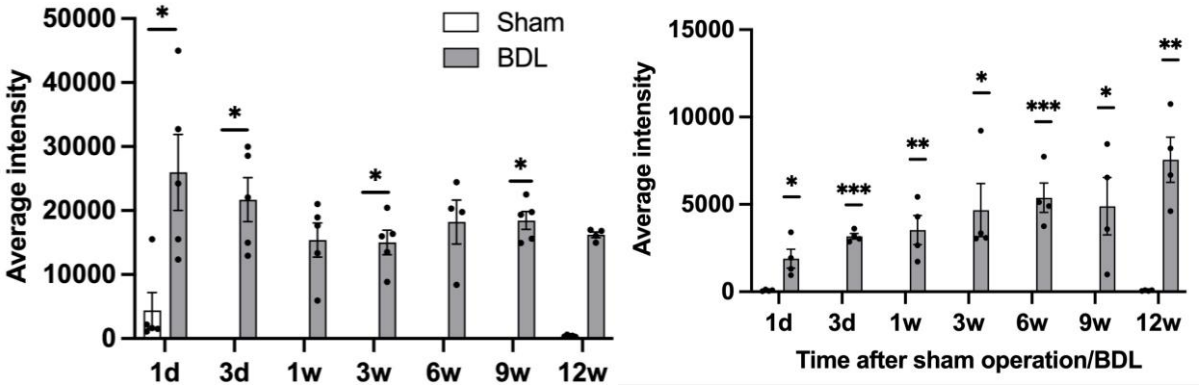

Fig. 14: Quantifications of MALDI-MSI images. data are presented as mean± SEM; n = 5 mice per group. ∗p <0.05; ∗∗p <0.01; ∗∗∗p <0.001 compared to sham day 1, Unpaired t test. The data are from male mice.

11.8 Confirmation of bile acids concentrations by LC-MS/MS

To check the above-described results, an independent technique, LC-MS/MS, was applied to quantify bile acids in the tissue homogenate of the liver, kidney and blood (Fig. 15). Similar as seen for TCA after MALDI-MSI analysis, also sum bile acids increased at day 1 after BDL in liver tissue. Thereafter, a plateau was reached. In contrast, renal tissue homogenate showed a continuous increase in bile acids concentrations. The two main bile acids species that increased after BDL were tauro-α/β-muricholate followed by taurocholate in both liver and renal tissues (Fig.15). It should be considered that tauro-α/β-muricholate represents a relatively hydrophilic, relatively untoxic bile acid, while taurocholic acid is more lipophilic with stronger cytotoxic effects.

Also, in the blood taken from the left heart chamber, a massive increase in total bile acids was seen after BDL, with tauro-α/β-muricholate and taurocholate representing the most increased individual bile acids (Fig. 15).

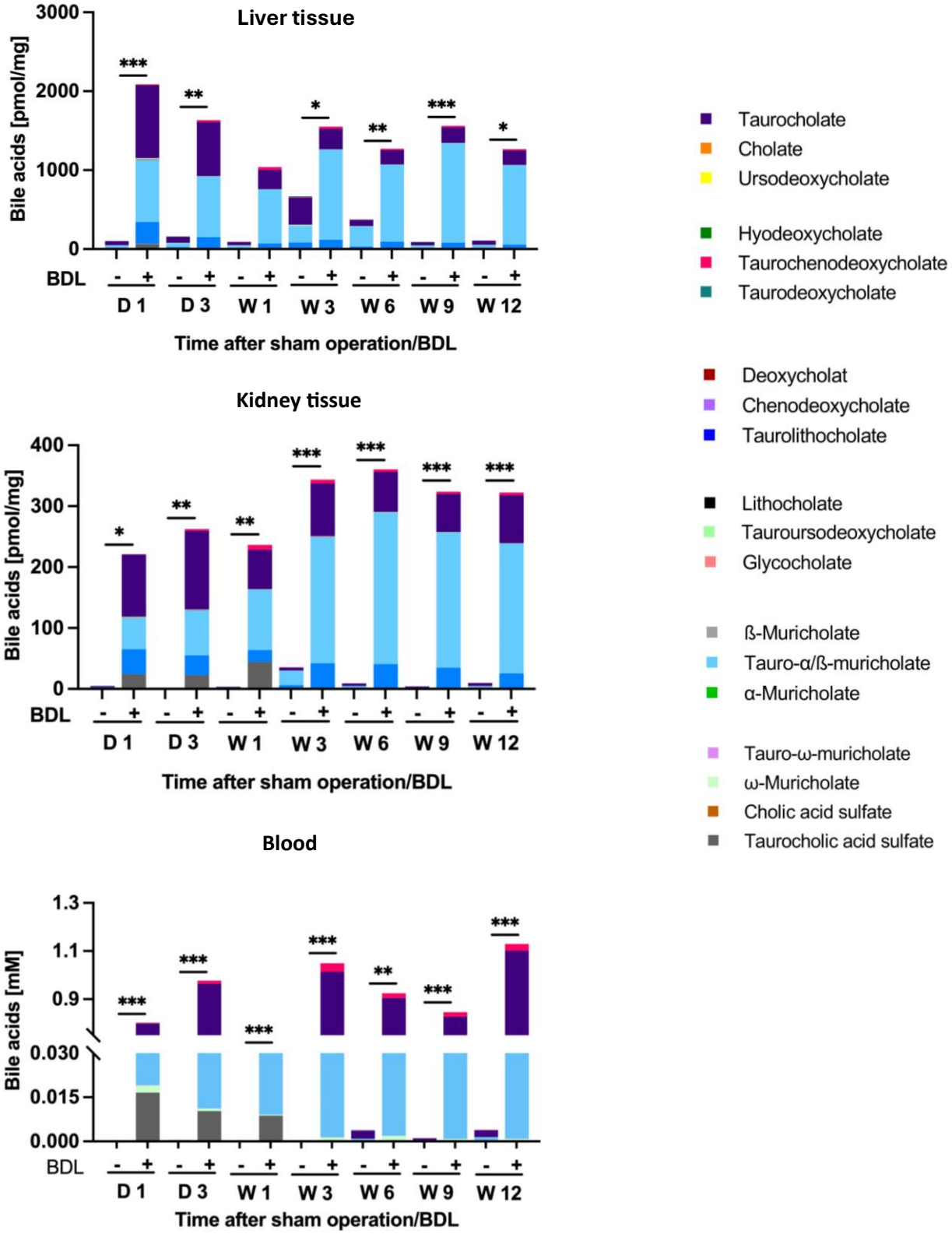

Fig. 15: Quantifications of bile acids concentrations in blood, liver and kidney tissues after BDL by LC-MS/MS. Data are presented as mean± SEM; n = 5 mice per group. ∗p <0.05; ∗∗p <0.01; ∗∗∗p <0.001 compared to sham day 1, Unpaired t test. The data are from male mice.

11.9 Clinical chemistry in plasma after BDL

Increased urea is one marker of kidney injury. Urea in plasma increased significantly at weeks 6, 9 and 12 after BDL compared to sham operated controls (Fig. 16). Vice versa urea decreased in urine, suggesting reduced glomerular filtration, particularly at the longest observation period of 12 weeks.

Bilirubin is a marker of cholestasis. It showed a permanent increase in plasma (Fig. 16). In urine the increase was largest at day 1 followed by a decrease thereafter. Both, direct and indirect bilirubin increased as a consequence of BDL, but the fraction of direct bilirubin was larger.

Creatinine is a well-established marker of renal injury. An increase of creatinine was obtained in blood while a decrease in seen in urine (Fig. 16). This constellation corresponds to decreased glomerular filtration.

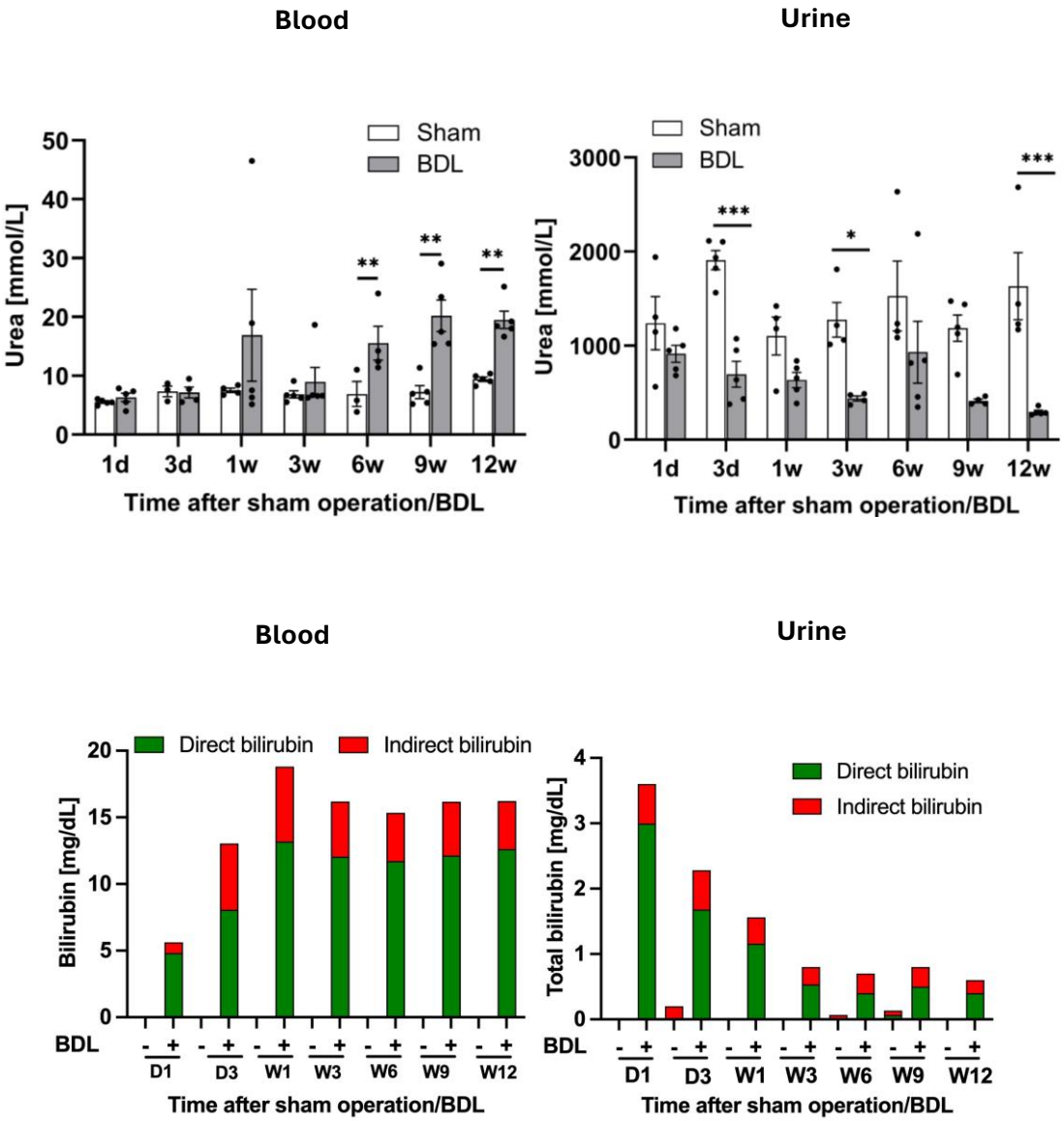

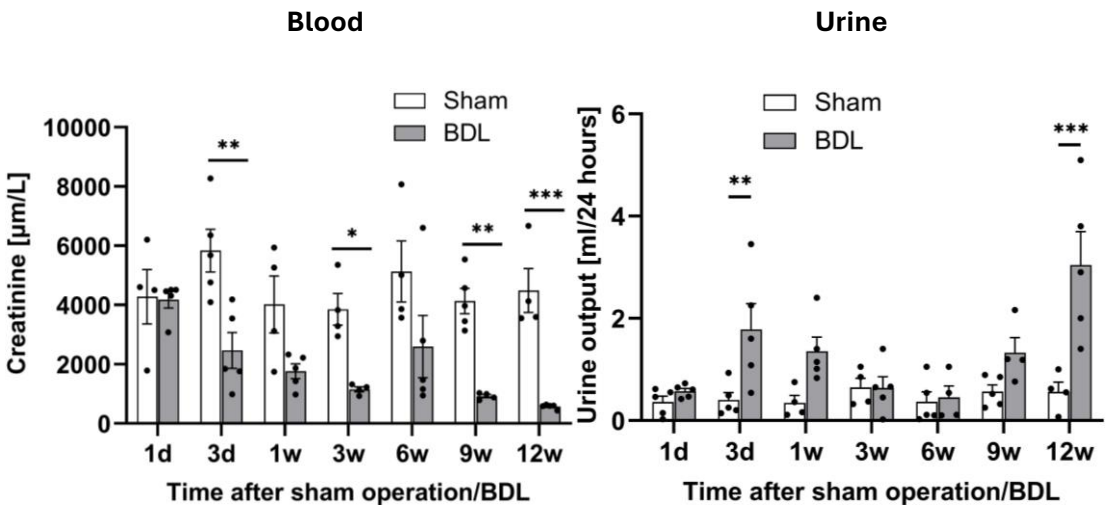

Fig. 16: Biomarkers of kidney injury in blood and in urine, and urine output. Data are presented as means ± SEM; n= 5 mice per group. *p< 0.05; **p< 0.01; ***p< 0.001 compared to the corresponding sham controls, Šídák's multiple comparisons test.

11.10 Gross pathology, histology and Immunohistochemistry of the kidney after BDL

Prior to microscopic analysis, images of the kidneys were captured to illustrate the gross pathology (Fig. 17). Of particular interest was the observation of green discolouration at weeks 6, 9 and 12 following BDL, which has been identified as a potential indicator of renal injury.

H&E staining showed a massive tissue damage at week 3 and up to week 12 (Fig. 18). Tubular dilation and enlarged glomeruli, also named “glomerular cysts” were seen.

To visualise leukocyte infiltration, immunostaining of the pan leukocyte marker CD45 was done (Fig 19). The result demonstrated leukocyte infiltration beginning already at day 3 after BDL, which intercified continuously.

Fibrosis was visualised by means of Sirius red staining (see Fig. 20). A significant increase in the Sirius red signal was observed at week 6 following BDL, with a further increase at later time periods. This finding indicates an ascending fibrosis process in the renal tissue after BDL.

A clinically well-established analysis is staining for bile casts. For this purpose, Hall’s stain was used (Fig. 21). The result demonstrated an increased of Hall’s stain positive casts already at week 1 after BDL. A Hall’s positive intratubular cast is indicated by the arrow. It should be considered that Hall’s stain consists of two components Fouchet’s reagent to visualise bile casts, and van Guieson’s stain also visualised fibrosis, which explains the similar appearance as seen for the sirius red images in Fig. 20.

A central question guiding this study is to identify the specific tubular epithelial cells that were affected by BDL. To address this question, aquaporin 1 (AQP1) was utilised as a

marker for proximal tubular epithelial cells, anti-thiazide-NaCl cotransporter (TSC) distal tubular epithelial cells, and aquaporin 2 was specifically applied to stain the collecting ducts. The triple-stained sections revealed that dilatation initially occurred in the proximal tubules, becoming evident at week 1 (Fig. 22). Subsequently, the distal tubules and collecting ducts were also compromised.

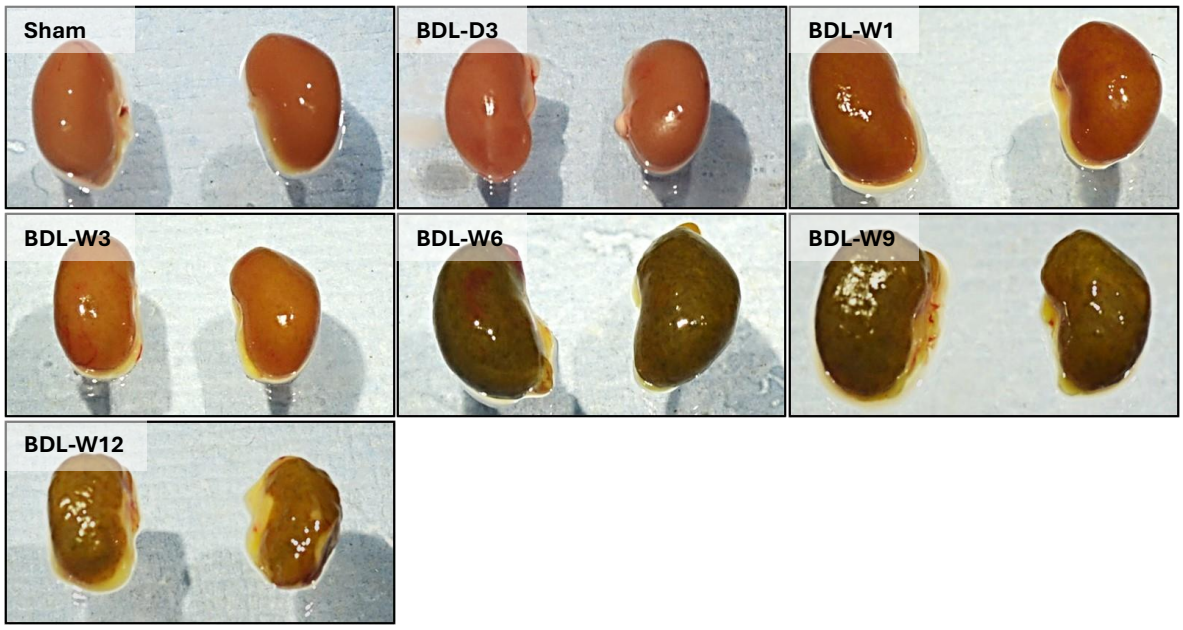

Fig. 17: Gross pathology of mouse kidneys reveals a greenish discolouration that is detectable up to week 6.

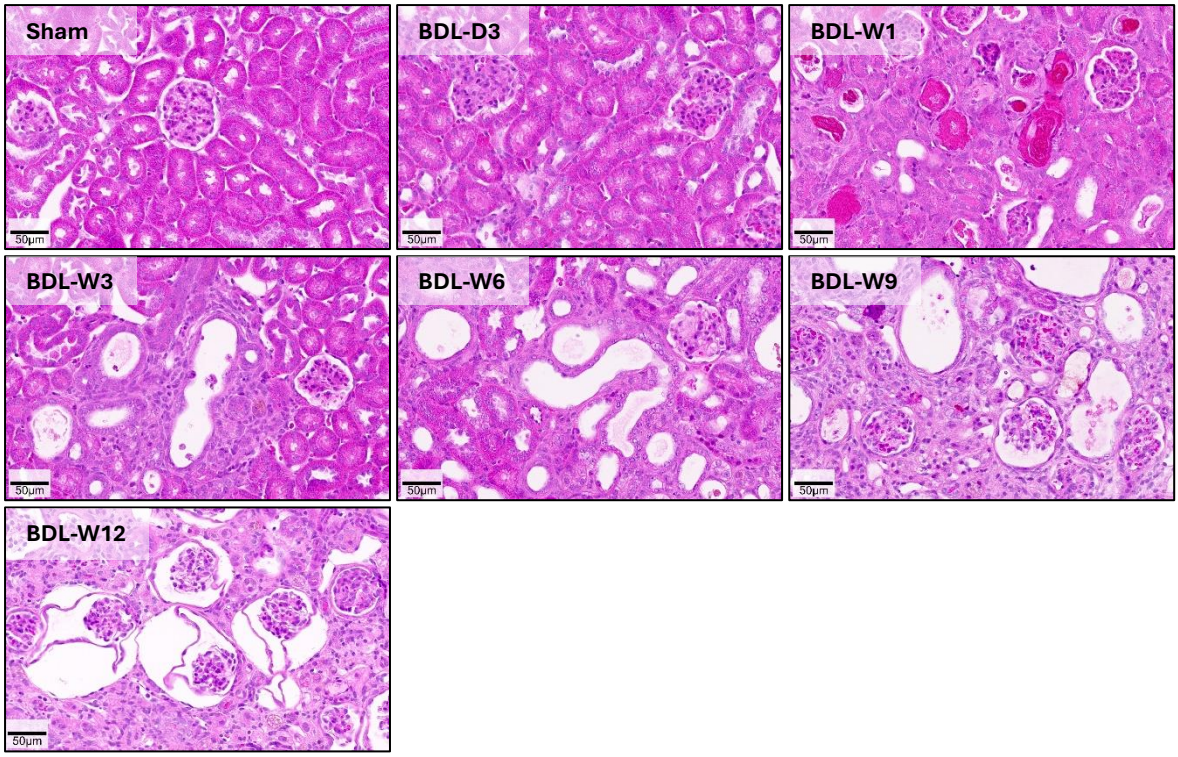

Fig. 18: H&E staining of kidney tissue at various time points after BDL showing an increased damage in tubular epithelial cells in the kidney tissues. Scale bars: 50 µm.

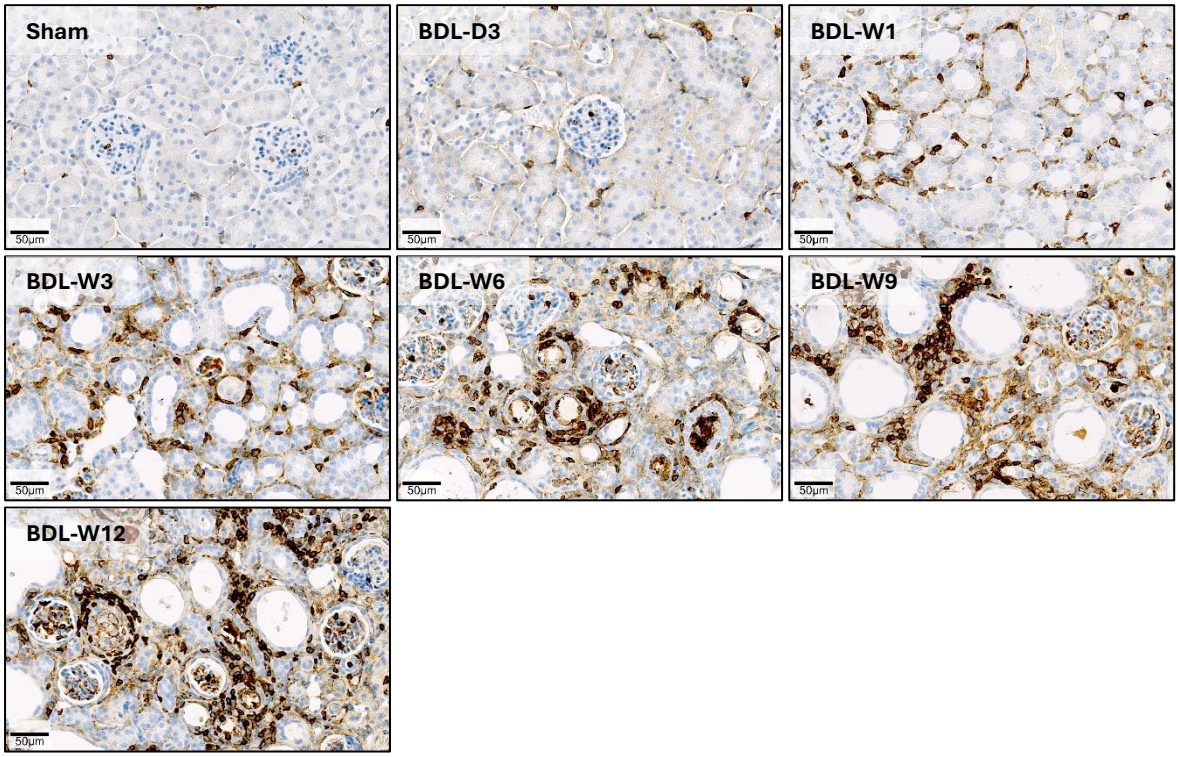

Fig. 19: Immunostaining of leukocyte (CD45) demonstrates an infiltration of immune cells in the kidney tissues. Scale bars: 50 µm.

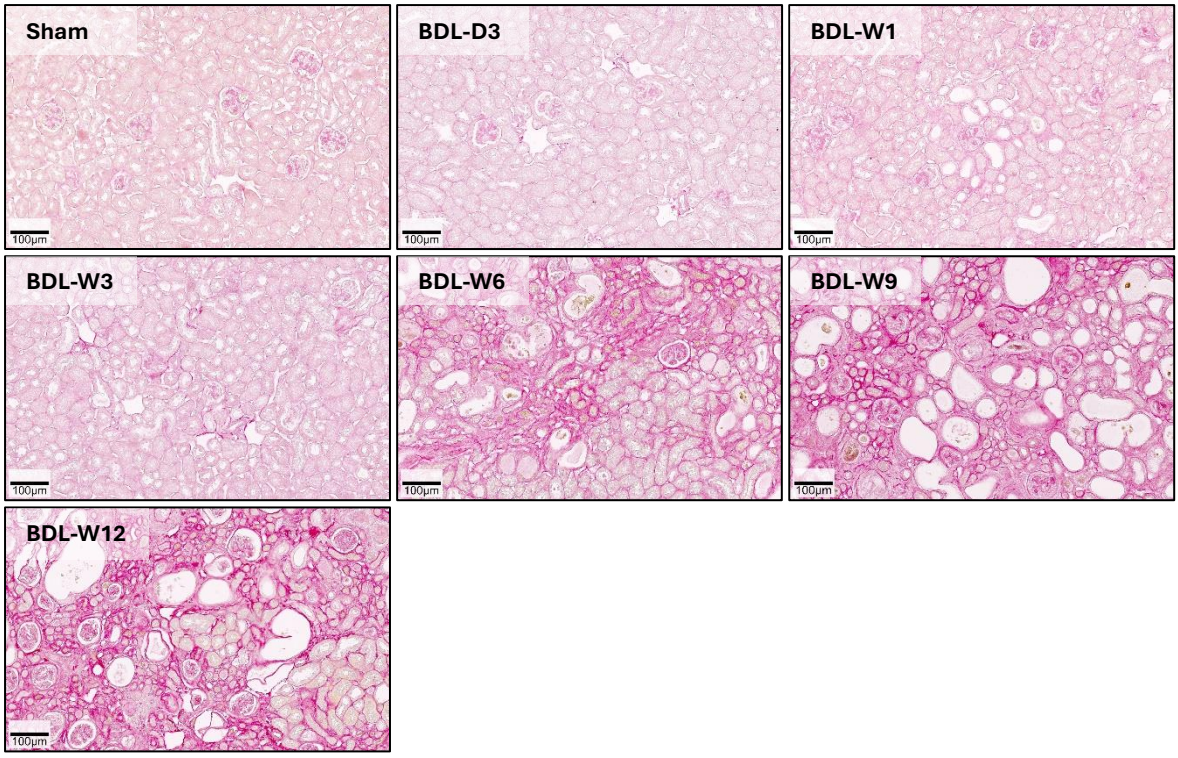

Fig. 20: Sirius Red staining showing time-dependently increasing collagen accumulation and fibrosis in kidney tissue. Scale bars: 100 µm.

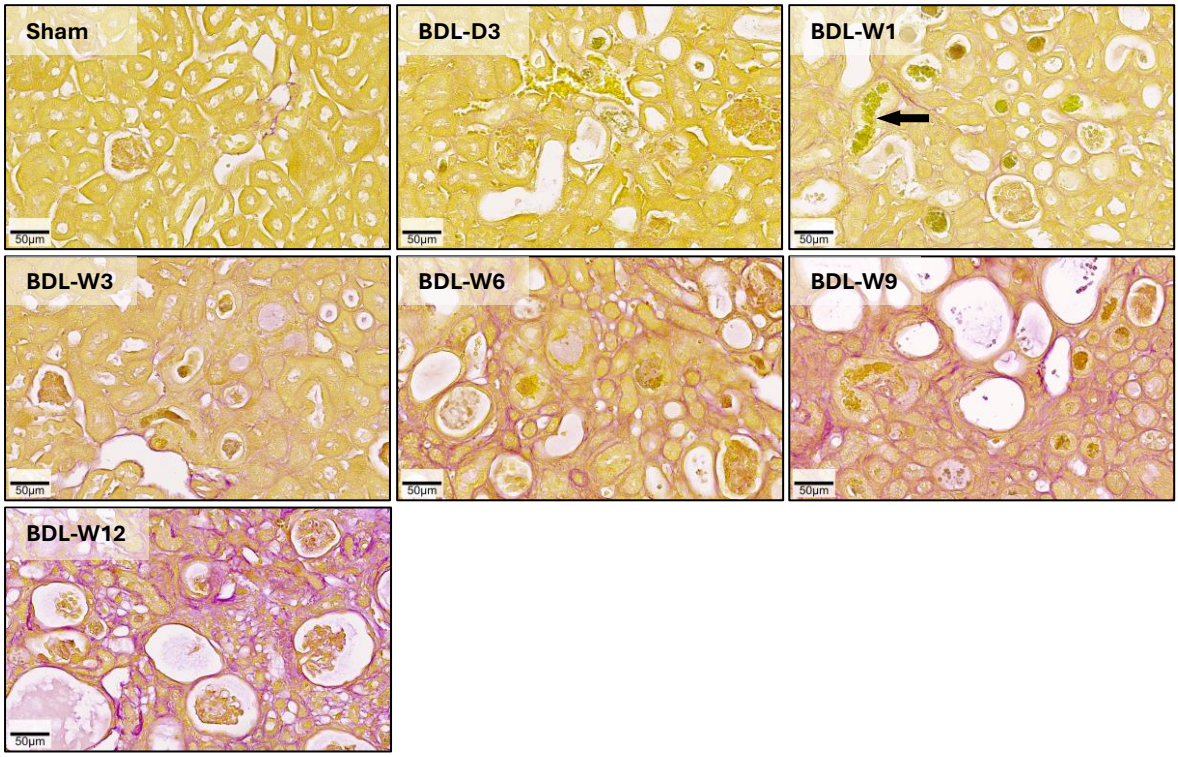

Fig. 21: Hall's staining showing time-dependently increasing casts accumulation and fibrosis in kidney tissue. Scale bars: 50 µm.

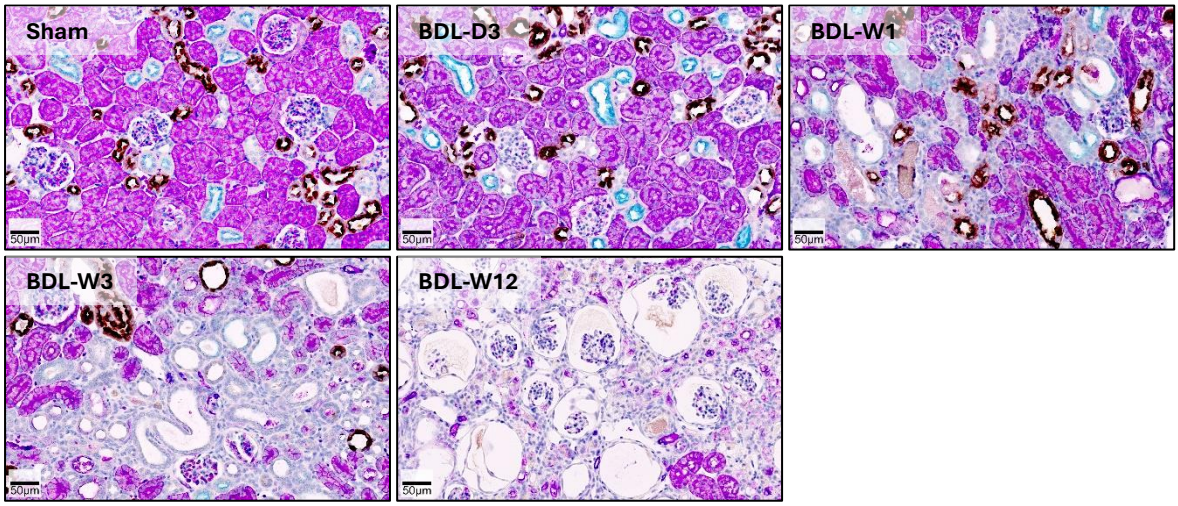

Fig. 22: Co-immunostaining of the proximal TEC marker AQP1, distal TEC marker TSC and the collecting duct marker AQP2 at various time periods after BDL. Dilatation occurred first for proximal tubules, which became evident at week 1 after. Only later also distal tubules and collecting ducts were affected. Scale bars: 50 µm.

11.11 Oxidative stress in tubular epithelial cells

To study oxidative stress an intravital imaging was used where 2',7'Dichlorofluorescein diacetate (DCF) in intravenously injected into mice, which generate the green fluorophore when oxidative stress is present. Two photon imaging 4h and 3 days after BDL showed oxidative stress in tubular epithelial cells (Fig. 23). Since the affected tubular epithelial cells showed a higher density of TMRE-positive mitochondria, they most probably represent proximal tubular epithelial cells. This also corresponds to the immunostaining results in Fig. 22 where the proximal tubules were affected after earlier time as distal tubules and collecting ducts.

At week 1 after BDL also tubular casts became visible also in two-photon microscopy (Fig. 23). Also, the massively dilated glomeruli were visible. The lumen of the enlarged glomeruli showed an intensive green auto-fluorescence that is possibly due to the high bilirubin (Fig.23).

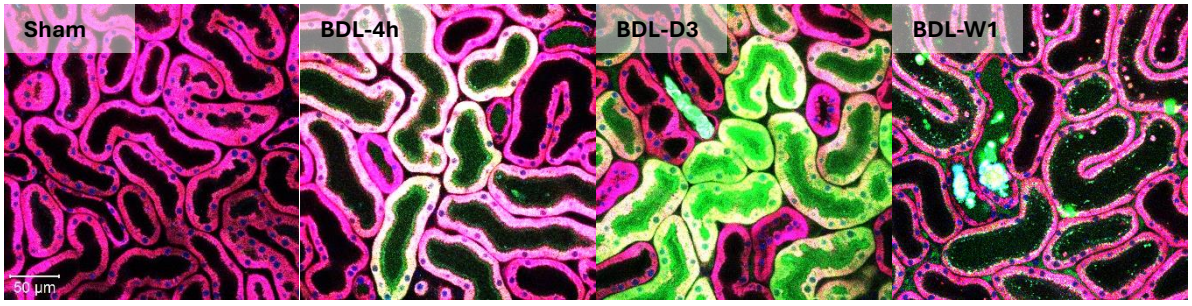

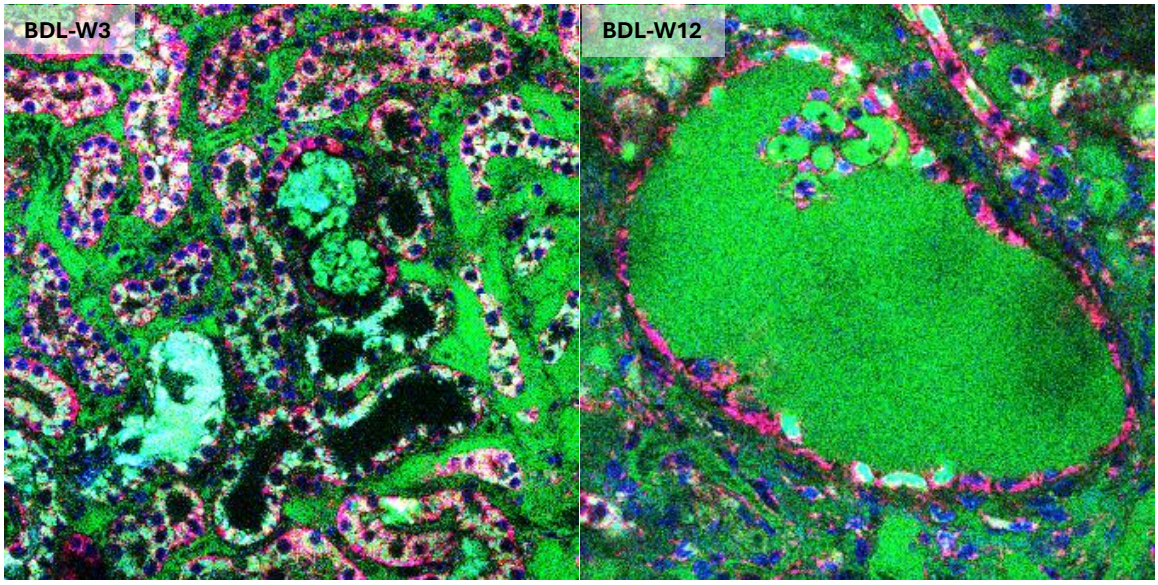

Hoechst – DCF-Auto-fluorescence - TMRE

Fig. 23: Intravital imaging showing the oxidative stress of proximal TECs 4 hours and 1 day after BDL, employing the marker DCF. The images show dead proximal tubular cells (TECs), and debris accumulated in the distal tubules at day 3 after BDL. Autofluorescence is evident and around the peritubular capillaries at week 3 after BDL. Finally, at week 12 after BDL, glomerular cysts are visible. Red: TMRE (the proximal tubules can be differentiated from distal tubules by their higher TMRE intensity); green: DCF (oxidative stress marker); blue: Hoechst.

The following photos from intravital imaging in Fig. 24 as in Fig. 23 provide a sequence of events in the pathogenesis of cholemic nephropathy. The following sequence of events is demonstrated by overview images of the kidneys at different time intervals after BDL: Zonated oxidative stress in the proximal tubular epithelial cells (BDL 4 hours, arrow – day 1), followed by a cell death of proximal tubular epithelial cells (days 1-3), then cast formation in distal tubules (day 3), next peritubular capillary leakiness (weeks 3 and 12), and finally glomerular cysts (week 12).

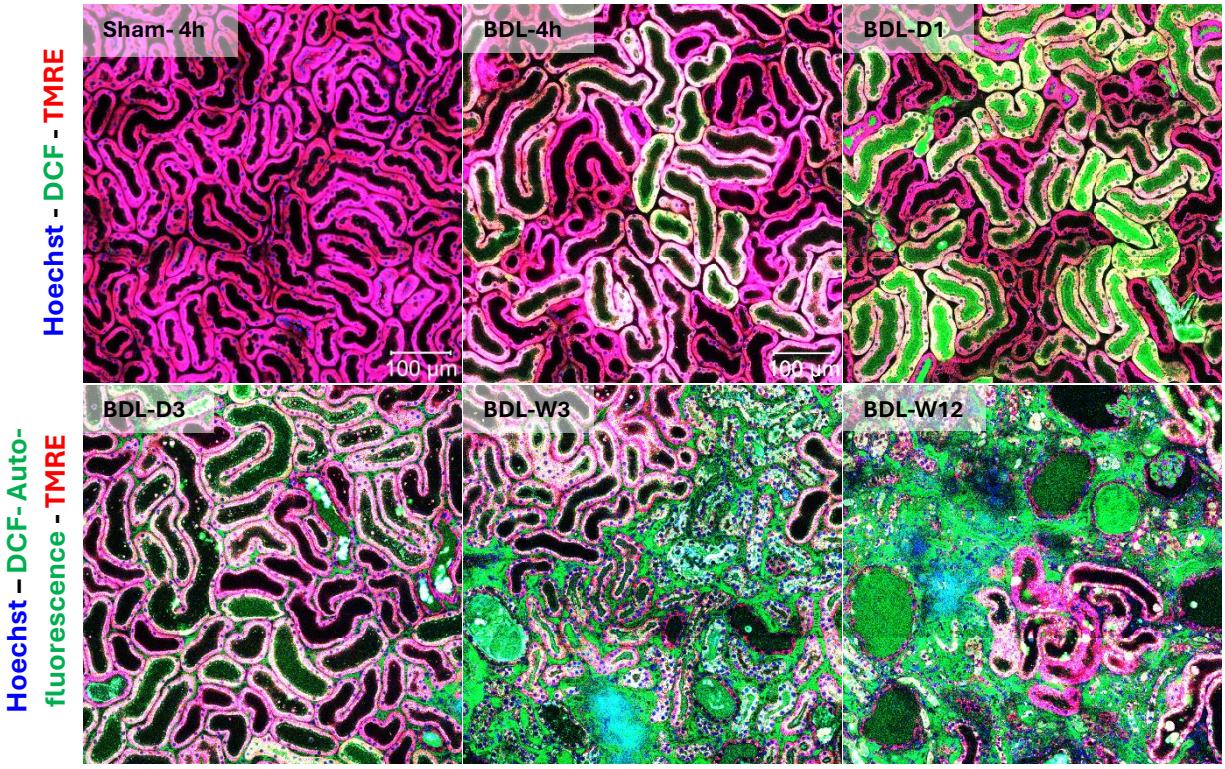

Fig. 24: Overview of the intravital images showing the oxidative stress of proximal TECs 4 hours and 1 day after BDL, employing the marker DCF. As illustrated by the images, dead proximal tubular cells (TECs) and debris accumulated in the distal tubules at day 3 after BDL. Autofluorescence is evident and surrounds the peritubular capillaries at week 3 post-BDL. Finally, at week 12 after BDL, glomerular cysts become visible. Red: TMRE (the proximal tubules can be differentiated from distal tubules by their higher TMRE intensity); green: DCF (oxidative stress marker); blue: Hoechst. Scale bars: 100 µm.

To study if the above-described oxidative stress in tubular epithelial cells leads to cell death, the intravital dye SYTOX green was intravenously injected, illustrating dispersed cell death events of tubular epithelial cells (Fig. 25). Most probably these represent proximal tubular epithelial cells, because of the high mitochondrial density. The release of cellular debris from dead proximal TECs into the tubular lumen was observed, with the debris subsequently flowing into the distal tubules. A portion of this residue adhered to the surface of the distal tubules and collecting ducts, forming casts and causing dilation (Fig. 25, 26).

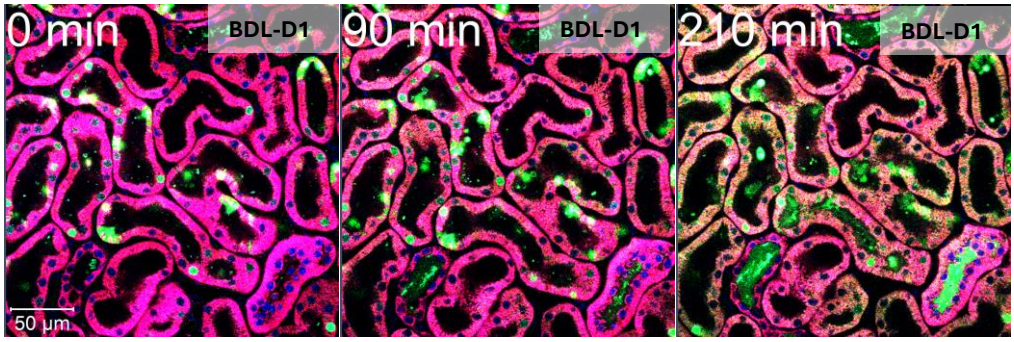

Hoechst - SYTOX Green - TMRE

Fig. 25: Intravital imaging of dead proximal tubular epithelial cells (pTEC) was performed at day 1 post-BDL, utilising the toxicity marker SYTOX Green to visualise cast formation in collecting duct and distal tubules. Scale bars: 50 µm.

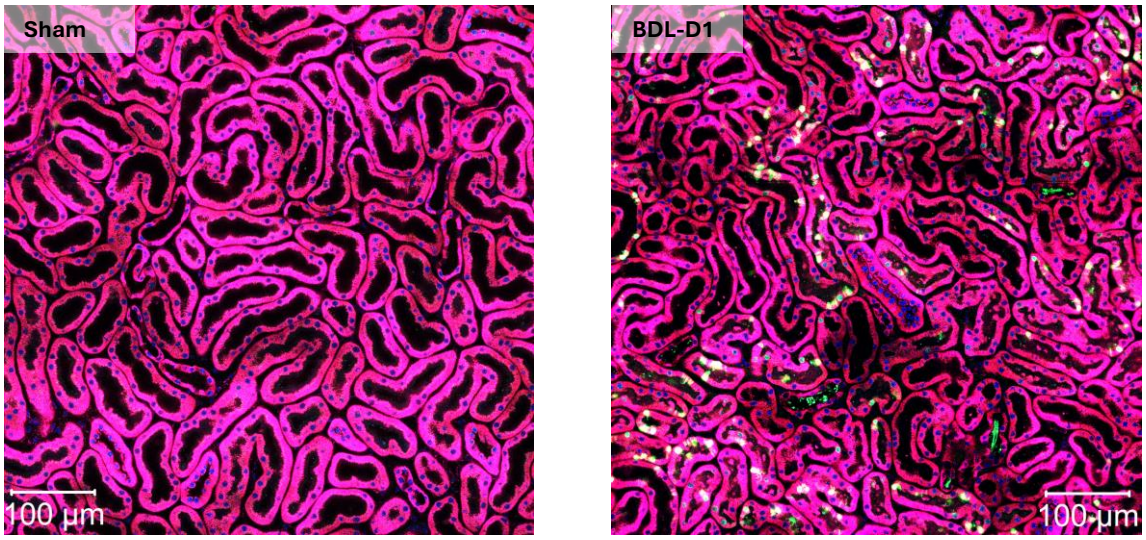

Hoechst - SYTOX Green - TMRE

Fig. 26: Overview of the intravital images of healthy (sham) and dead proximal tubular epithelial cells (pTEC) performed at day 1 post-BDL. Scale bars: 100 µm.

11.12 Leaky renal capillaries after BDL

A well-established technique to visualise leaky capillaries relies on the intravenous injection of the magenta dye Evans blue. Evans Blue is maintained within the lumen of intact capillaries (Fig. 27). However, it leaks into the adjacent interstitium when capillaries become leaky. Using this technique, I demonstrated that leaky renal capillaries occur after BDL (Fig. 27). However, this represents a relatively late event that is only observed at week 6 after BDL and thereafter.

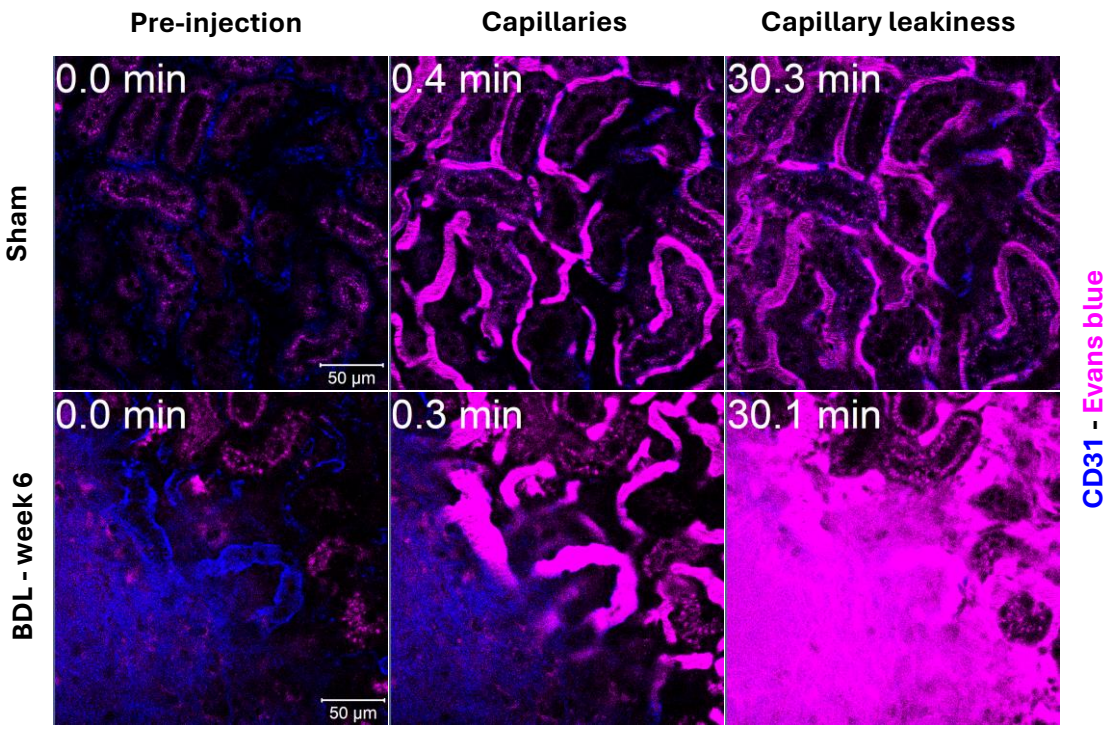

Fig. 27: Leakiness of peritubular capillaries was observed six weeks after BDL. Intravital imaging was performed following the injection of Evans blue (magenta). Blue into the tail vein. Peritubular capillaries are visualized by anti-CD31 antibody (blue); scale bars: 50 µm. Data are presented as mean ± SEM; n = 5 mice per group. $*p$ <0.05; $**p$ <0.01; $***p$ <0.001 compared to the corresponding sham controls; Tukey's multiple comparisons test. The data are from male mice.

Image analysis of the intravital videos demonstrated the operated signal within capillaries and the almost negative signal of the interstitium in sham mice (Fig. 28). Conversely, 6 weeks post-BDL, a stronger increase in signal is seen in both blood capillaries and interstitium, indicating that a strong leakage from peritubular capillaries into the interstitium has been observed.

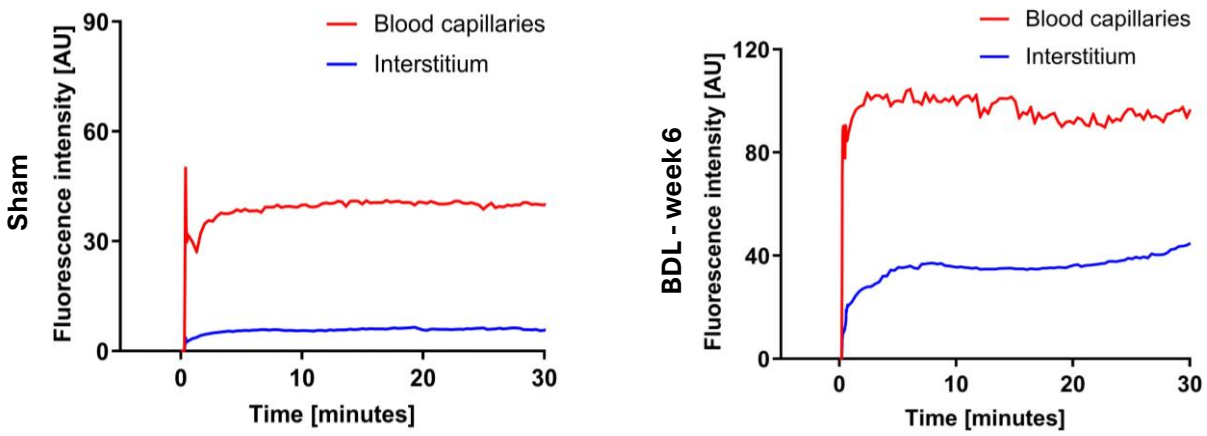

Fig. 28: The signal of Evans blue is quantified in the peritubular capillaries and in the interstitium according to the intravital videos. Data are presented as mean ± SEM; n = 5 mice per group. ∗p <0.05; ∗∗p <0.01; ∗∗∗p <0.001 compared to the corresponding sham controls; Tukey's multiple comparisons test. The data are from male mice.

To characterise the interstitial tissue into which Evans blue leaked (Fig. 27), we performed combined intravital imaging of Evans blue (magenta) and rhodamine 123 (green) (Fig. 29). Rhodamine 123 is a mitochondrial activity marker that visualises vital cells. Interestingly, Evans blue leaks into tissue domains that were Rhodamine 123 negative, therefore representing dead tissue.

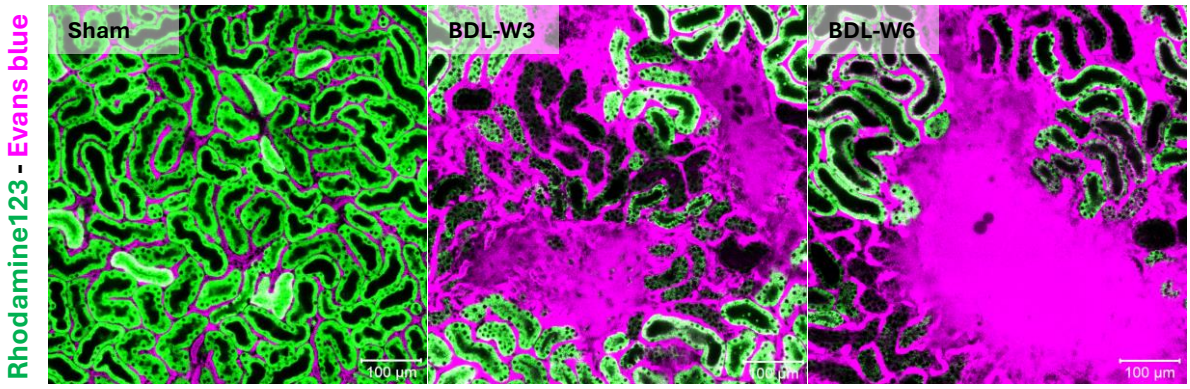

Fig. 29: Overview of Intravital imaging following tail vein injection of Evans Blue in mice. Intravital imaging was done under both control conditions and after 3 and 6 weeks of bilateral carotid artery ligation (BDL) to investigate the Leakiness of peritubular capillaries. Evans blue (Magenta); rhodamine123 (green); scale bars: 100 µm.

A well-established marker for endothelial cells is MECA-32. Immunostaining showed a strong decrease of the MECA-32 signal at week 3, 6,9 and 12 (Fig. 30). Therefore, analysing of the endothelial cells marker confirmed the above-described results with

intravital Evans blue imaging, this showed clear damage to the endothelial cells and leaky peritubular capillaries after BDL.

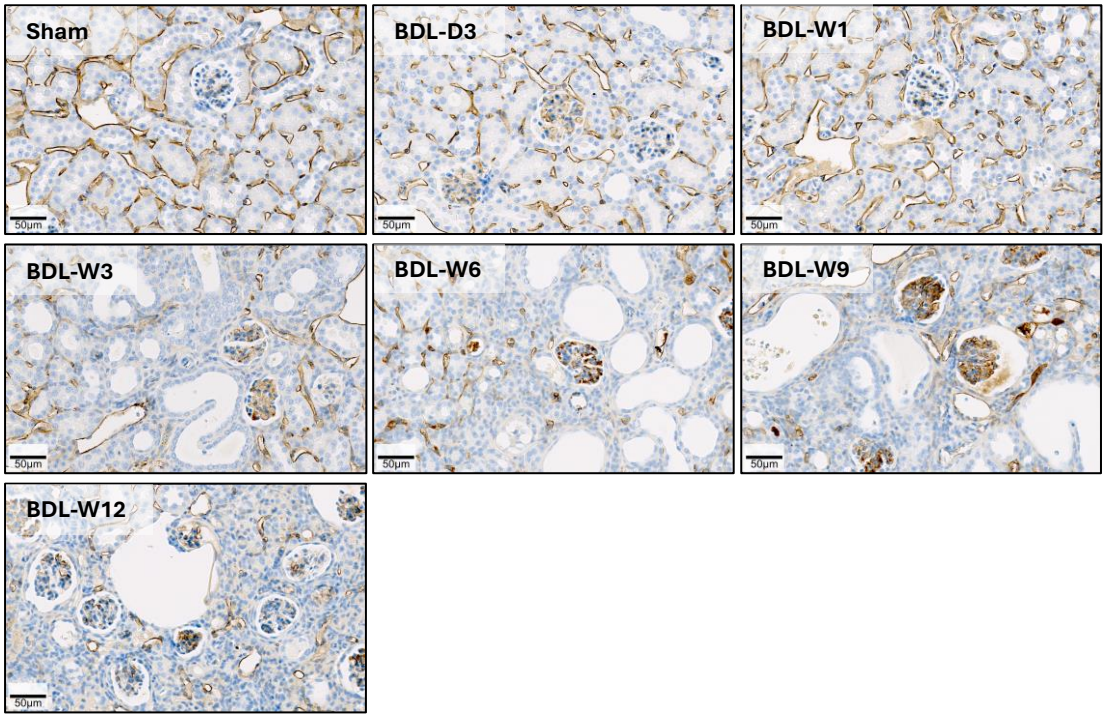

Fig. 30: Immunostaining was performed using antibodies directed against the endothelial cell antigen MECA-32 to investigate the damage of endothelial cells following BDL. Scale bars: 50 µm.

11.13 Cell type specific tissue injury markers

Since the above-described imaging experiments suggested that damage occurs first in the proximal and only later in the distal tubular epithelial cells, I studied the proximal tubular epithelial cells specific biomarker KIM-1 in plasma at various time periods after BDL. KIM-1 massively increased at day 3 to week 3 (Fig. 31, A). It decreased again at week 12 after BDL.

NGAL represents a kidney injury marker for proximal and distal tubular epithelial cells. It remained elevated also at the longest period of week 12 after BDL (Fig. 31, B).

Cystatin C is a marker of compromised glomerular filtration. Only at the latest time periods of 9 and 12 weeks after BDL glomerular filtration was compromised (Fig. 31, C).

Results

A

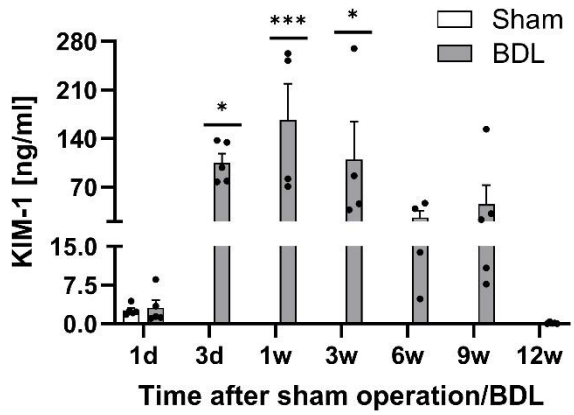

B

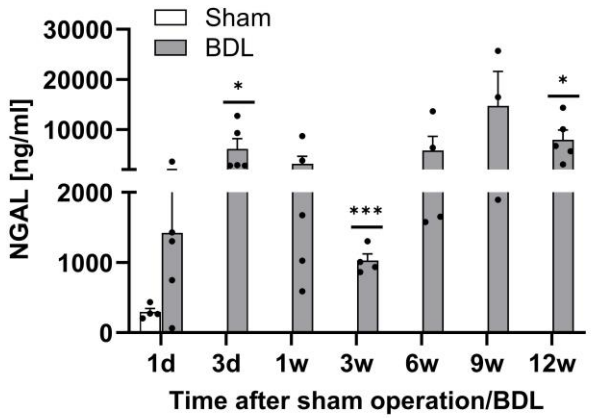

C

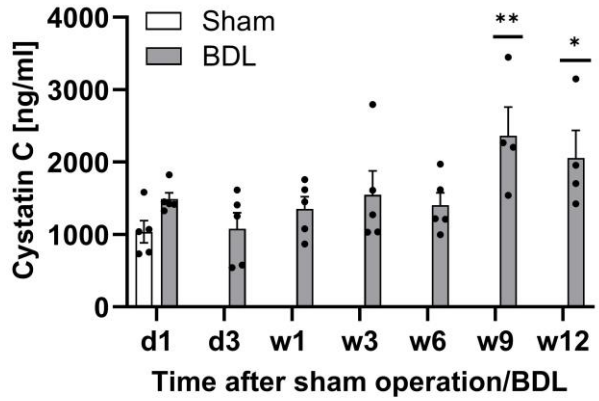

Fig. 31: Time course of kidney injury biomarkers in urine. Data are presented as mean ± SEM; n = 5 mice per group. $*p<0.05$; $**p<0.01$; $***p<0.001$ compared to the corresponding sham controls; Tukey's multiple comparisons test. The data are from male mice.

11.14 Pilot study with an ASBT inhibitor

In the previous experiments I have shown that bile acids, particularly TCA, is enriched in a subpopulation of renal proximal tubular epithelial cells. It is known that proximal tubular epithelial cells express ASBT at their luminal side as an uptake transporter of bile acids [1]. Therefore, inhibition of ASBT may ameliorate renal injury in cholestasis. Recently, a systemically available ASBT inhibitor, AS0369, has been developed by Erik Lindström (Albireo Pharma Inc, Boston, MA, USA) and was made available for my study.

In a pilot experiment I administered 0, 15, 30, 60 and 120 mg AS0369/Kg body weight by gavage to male C57BL6/N mice (experimental schedule: Fig. 32). Interestingly, AS0369 increased urinary concentrations of non-sulfated bile acids, while sulfated bile acids were less affected (Fig 33, A). This agrees to the fact that non-sulfated bile acids have a lower affinity to ASBT [1].

While urinary bile acids concentrations increased, the opposite constellation -a decrease of bile acids- was observed in blood (Fig. 33, B). For the maximal effect dose 60 mg/kg was chosen.

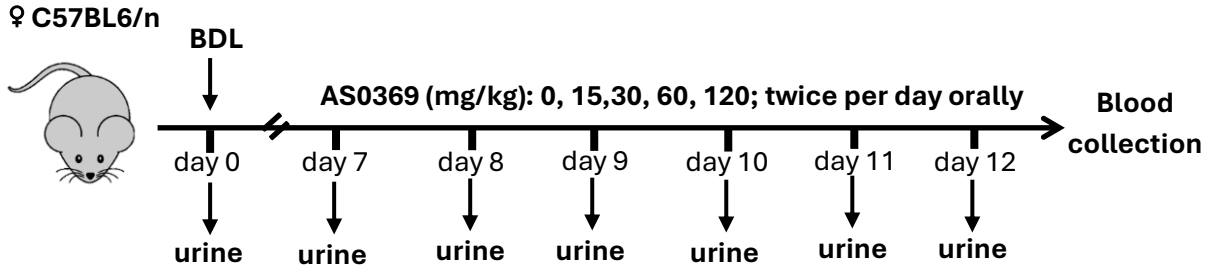

Fig. 32: Experimental schedule illustrating the different steps of the experiments that have been planned. 7 days after BDL and sham operations, the mice receive different doses of AS0369 twice daily per oral gavage for 5 days. Blood and urine samples were collected from mice. These samples were stored properly so that they could be analysed later.

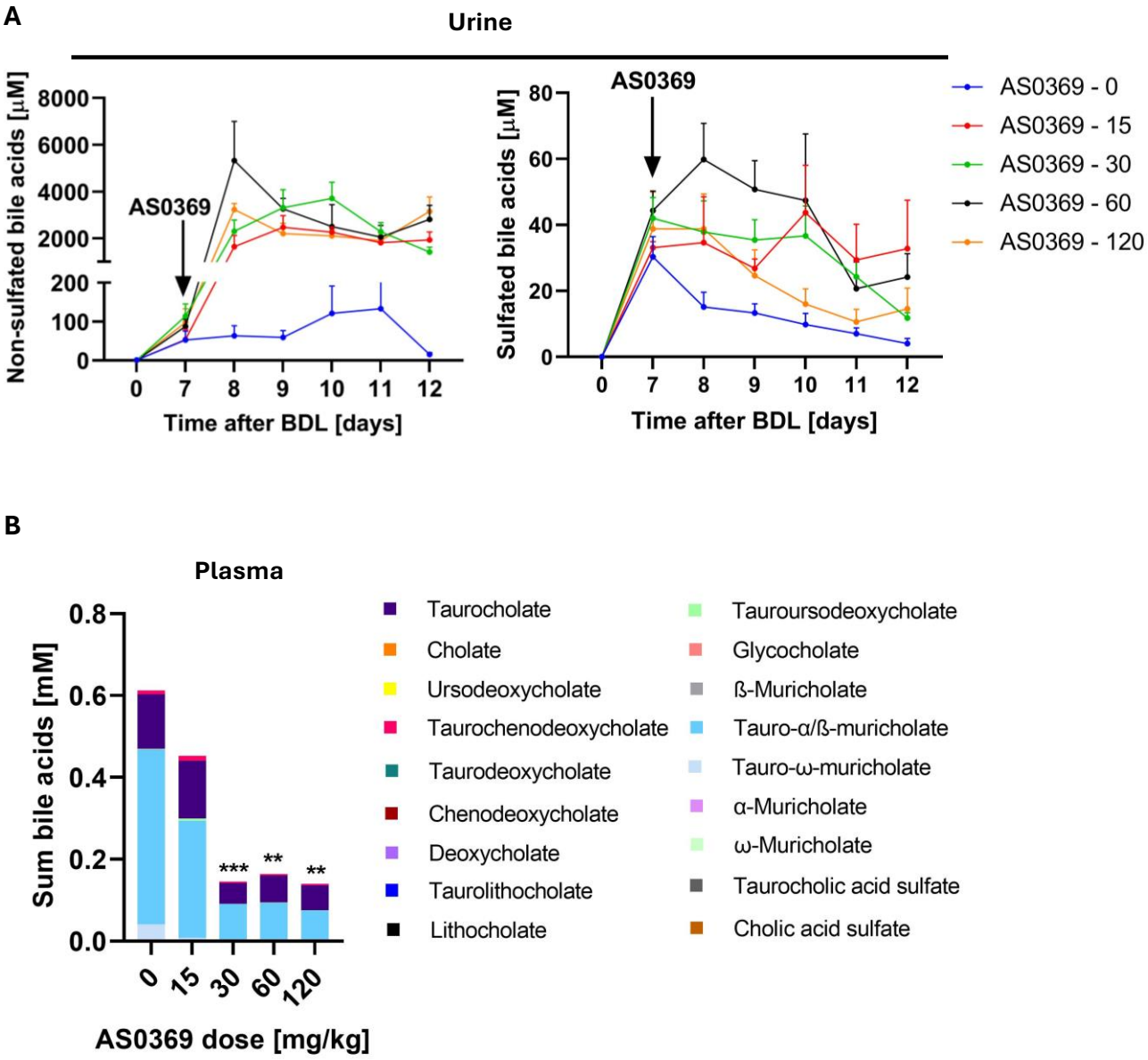

Fig. 33: (A, B): Sulfated and non-sulfated BAs concentrations in urine and plasma of BDL mice after AS0369 administrations. Data are presented as mean ± SEM; n = 3-6 mice per group; $**p$ <0.01; $***p$ <0.001 compared to the controls (0); Tukey's multiple comparisons test.

11.15 ASBT inhibition prevents TCA enrichment in proximal tubular epithelial cells

To study bile flux in kidneys with vehicle or AS0369 treatment of anesthetised BDL mice I used intravital two-photon microscopy. Bolus injection of 1mg TCA-FITC per Kg body weight shows strong appearance of the TCA signal in the lumen of the renal tubules of BDL mice that occurred immediately after the increase in the capillaries (Fig. 34). This was in contrast to the situation after BDL mice treated with AS0369, where a much stronger decrease of TCA signal in the blood capillaries followed by a strong reduction of

TCA-FITC uptake into the proximal tubular epithelial cells was seen (Fig. 34). This discrepancy serves to underscore the efficacy of the AS0369 treatment.

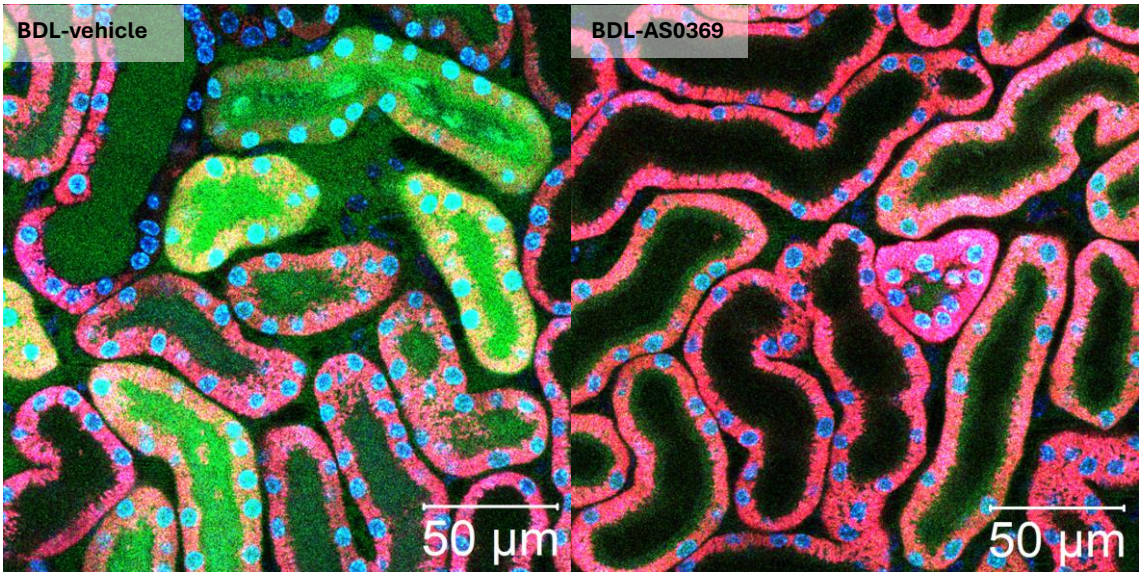

Fig. 34: Decrease of TCA uptake into proximal tubular epithelial cells after AS0369 treatment. Intravital images were taken from 3 days post BDL mice kidneys after treatment with AS0369 (60 mg/kg, twice daily) or vehicle. Imaging was conducted approximately two hours following the last administration of AS0369. Red: TMRE; green: TCA; blue: Hoechst. Scale bars: 50 µm.

In order to investigate the impact of ASBT inhibition on oxidative stress, intravital imaging was used, in which 2',7'-dichlorofluorescein diacetate (DCF) was intravenously injected into mice. The results obtained demonstrated that oxidative stress in tubular epithelial cells was significantly reduced in mice subjected to BDL compared to the vehicle-treated BDL mice (Fig. 35).

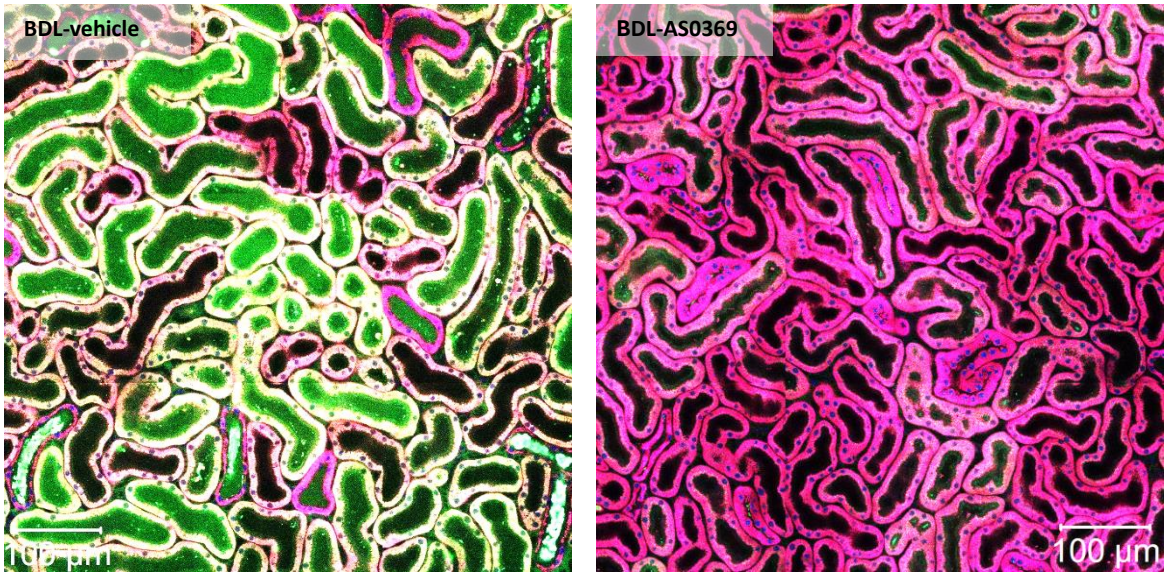

Fig. 35: Overview of intravital imaging showing the oxidative stress of proximal tubular epithelial cells in mice on day 2 after BDL, employing the marker DCF. The images show strong amelioration of dead proximal tubular cells and tubule casts after treatment with AS0369. Red: TMRE (the proximal tubules can be differentiated from distal tubules by their higher TMRE intensity); green: DCF (oxidative stress marker); blue: Hoechst. Scale bars: 100 µm.

11.16 ASBT inhibition in BDL mice improves survival, body weight and the gross pathology of kidneys

After improvement of the cholestatic mouse model which led to CN in mice and selection of the dose of AS0369 (60mg/kg). In this chapter I will investigate the efficacy of ASBT inhibition in prevention on BDL induced CN.

Following the experimental setup described in Figure 36, BDL or sham mice were treated for 6 weeks with AS0369 or vehicle. Biological samples were collected for later analysis. The survival was improved for BDL mice treated with AS0369; the mice show the same survival as the sham vehicle mice. In contrast BDL vehicle mice which showed a decreased survival indicating the increasing mortality of cholestatic mice (Fig. 37, A). The same is true for body weight, the loss in body weight seen in BDL mice is regained in AS0369 treated BDL mice (Fig. 37, B). These positive results are a first step towards improving efficient therapy of cholemic nephropathy (CN) by ASBT inhibition.

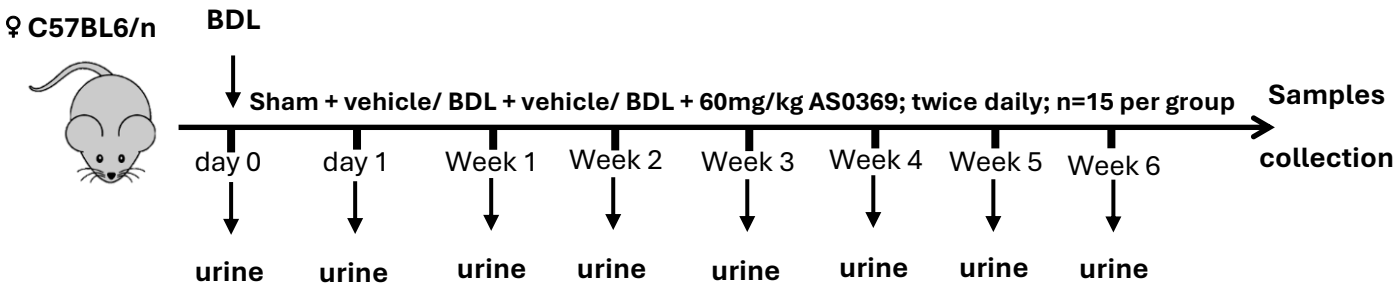

Fig. 36: Experimental schedule illustrating different steps of the experiments that have been planned. After BDL and sham operations, mice were treated for 6 weeks with AS0369 or vehicle (sham only with vehicle). Different samples were collected from the female C57BL6/N mice. These samples were stored properly so that they could be analysed later.

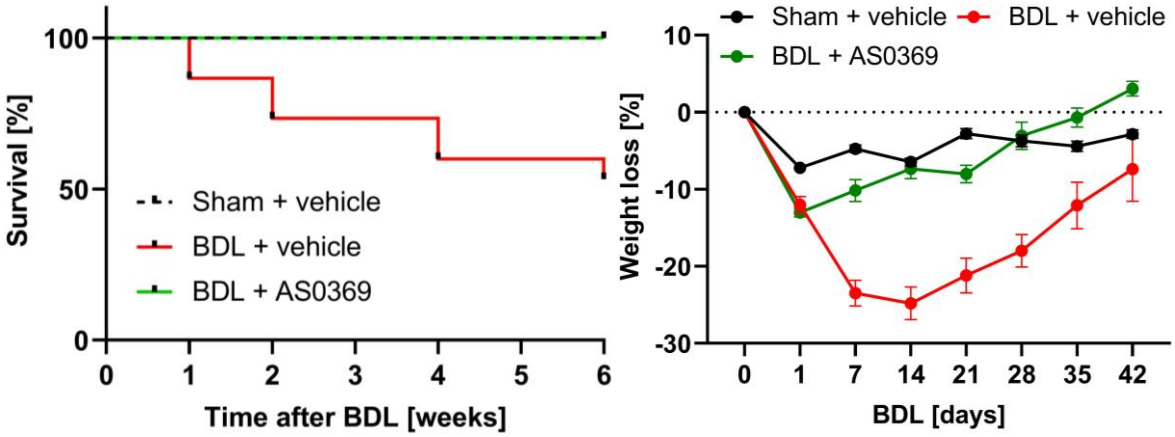

Fig. 37: Survival analysis and body weight changes. Both analyses show a strong beneficial effect of BDL mice after treatment with AS0369. The data are from female mice and correspond to the three treatment groups (sham-vehicle/ BDL-vehicle/ BDL-AS0369).

To analyse the morphological changes, I analysed the gross pathological images. There is a clear reduction in gallbladder dilatation and increased bile volume in the liver of AS0369 treated BDL mice (Fig. 38). The kidney of AS0369 treated BDL mice also shows a strong improvement in morphology, there is no more greenish color due to bilirubin accumulation in BDL mice and the shape of the kidney becomes more similar to the healthy kidney of sham vehicle mice (Fig. 38). These observations indicate a major improvement demonstrating the efficacy of ASBT inhibition in BDL mice.

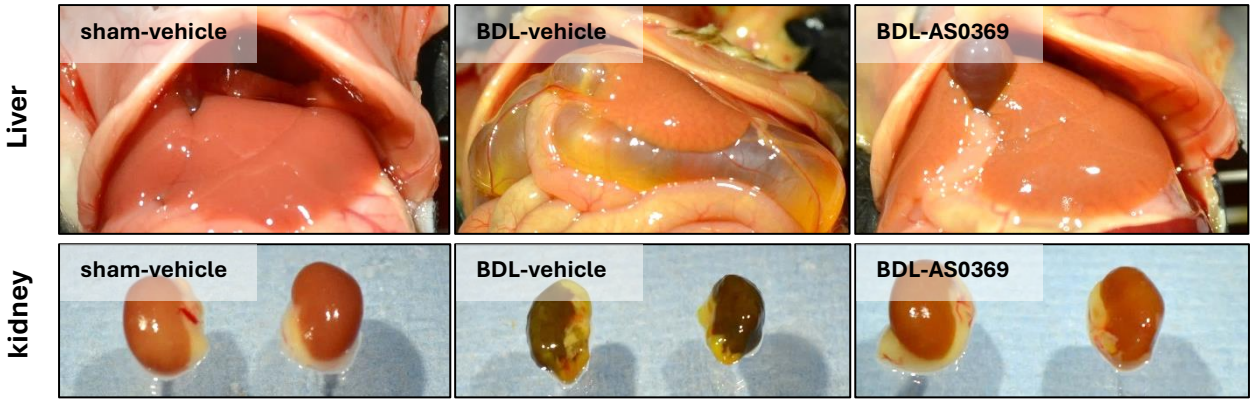

Fig. 38: Morphology of the gallbladder, the liver and the kidneys after bile duct ligation. The findings reveal a clear decrease in the dilatation of the gallbladder seen in the liver of BDL vehicle mice with AS0369 treatment, accompanied by a reduction in bile volume. AS0369 improved the efficacy to reduce the greenish coloration resulting from the accumulation of bilirubin in the kidneys, thereby minimizing the associated damage. The images are from female mice and correspond to the three treatment groups (sham-vehicle/ BDL-vehicle/ BDL-AS0369).

11.17 Influence of ASBT inhibition on bile acids in the gallbladder, urine, tissue and blood

Analysis of bile volume in the gallbladder shows a strong decrease in AS0369 treated BDL mice compared to BDL vehicle mice (Fig. 39). This result corresponds to the gross pathology observations in Figure 36 and improves the efficacy of ASBT inhibition in reducing bile volume.

In order to check bile acid concentrations, LC-MS/MS was used to quantify bile acids in urine, tissue homogenate of liver, kidney, blood and bile (Figure 40). A significant increase in the sum of bile acids was observed in the urine of BDL AS0369 mice on day 1. This increase was found to be reduced but remained at significant levels until week 6, indicating an increased bile acid output in the urine, which is reflected in a decrease in bile acid concentration in the blood circulation (Fig. 40). This reduction was also observed in both homogenates of liver and kidney tissue, as well as in bile (Fig. 40). The elevated levels of bile acids in urine and the reduced levels in blood circulation and other samples represent a further improvement in the protective influence of ASBT inhibition on bile acids, consequently on the induced CN.

Results

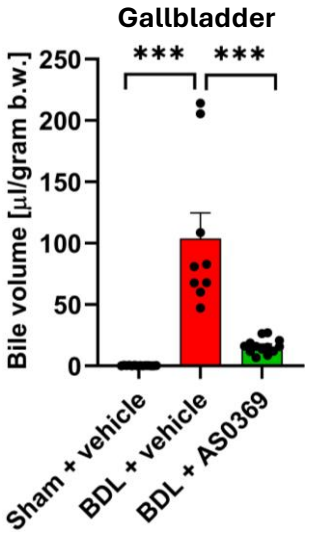

Fig. 39: Quantifications of bile volumes in the gallbladder. ***p <0.001, Tukey's multiple comparisons test. The data are from female mice and correspond to the three treatment groups (sham-vehicle/ BDL-vehicle/ BDL-AS0369).

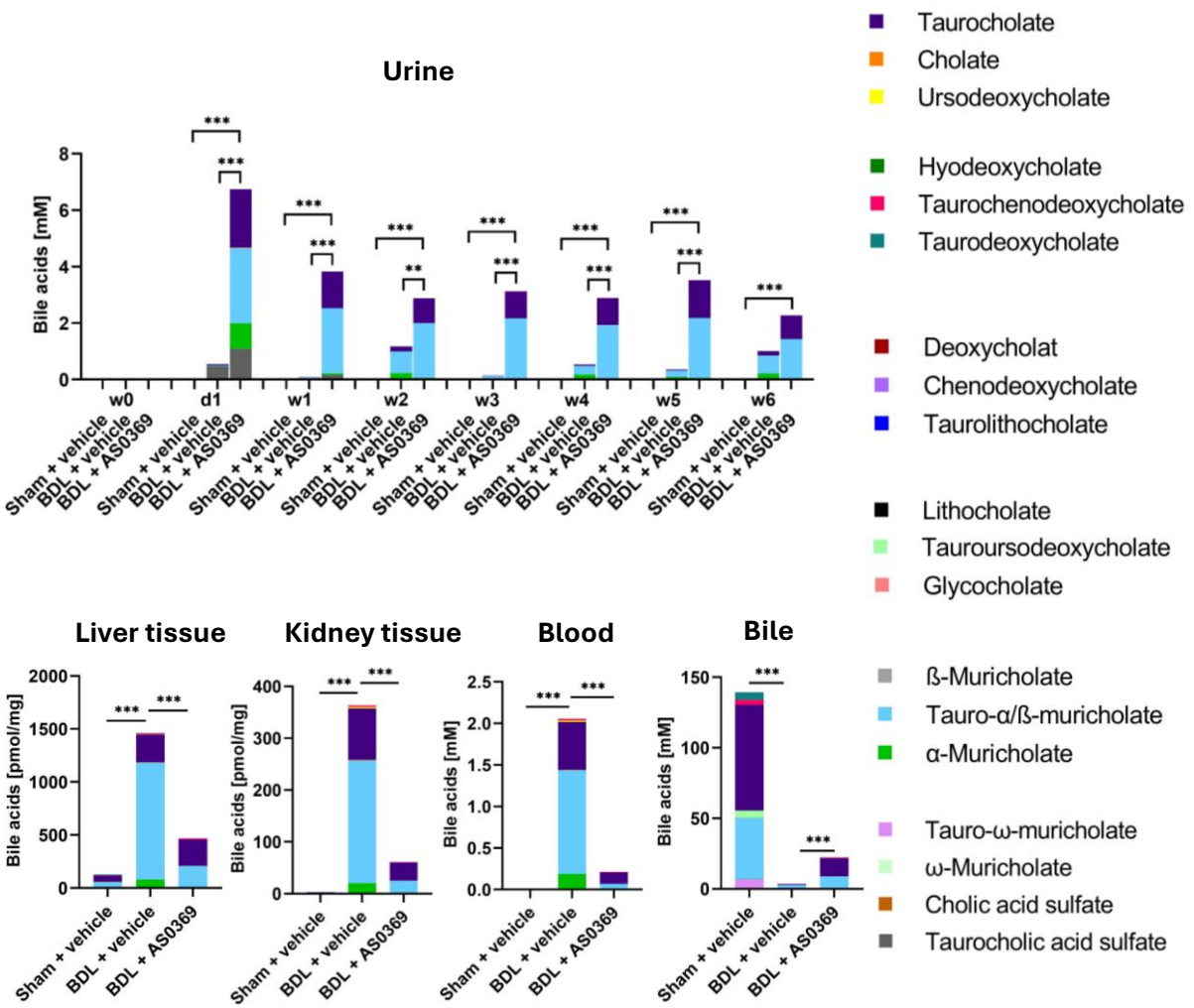

Fig. 40: Quantifications of bile acids concentrations in urine, liver and kidney tissues, blood and bile after BDL by LC-MS/MS. ***p <0.001, Tukey's multiple comparisons test.

The data are from female mice and correspond to the three treatment groups (sham-vehicle/ BDL-vehicle/ BDL-AS0369).

11.18 MALDI-MSI analysis of liver and kidney tissues before and after ASBT inhibition

To verify the results seen in the above analysis, MALDI-MSI was used to identify accumulation of TCA in liver and kidney tissues of BDL mice treated with AS0369 or vehicle, and sham vehicle is also analysed as a healthy control. The results are shown in Figure 41. When analysing the TCA signal in the liver tissue, there is a clear reduction in the TCA signal in BDL AS0369 mice compared to BDL vehicle mice (Fig. 41 A). To get a better overview of the TCA signal in the liver and kidney tissues, whole slide scans were taken from the liver and kidney of the three experimental groups (sham control / BDL vehicle / BDL-AS0369) (Fig. 41 B). The whole slide scans show the same trends. The reduction of the TCA signal in both liver and kidney tissues became more evident, leading to a further improvement in the efficacy of ASBT inhibition against elevated bile acid levels and subsequently against CN progression.

The quantification of this signal also shows the reduction observed in the MALDI images of the liver tissue (Fig. 42). The kidney of BDL AS0369 mice shows the same trend observed in liver tissue. In kidney tissue of AS0369 treated BDL mice, there is a strong decrease in TCA signal which became close to that of the healthy control (sham vehicle) (Fig. 42). Quantification of this observation validates the protective effect of AS0369 in kidney tissue. These findings further enhance the beneficial influence of ASBT inhibition on tissue bile acid concentrations and allow for improved prevention of CN.

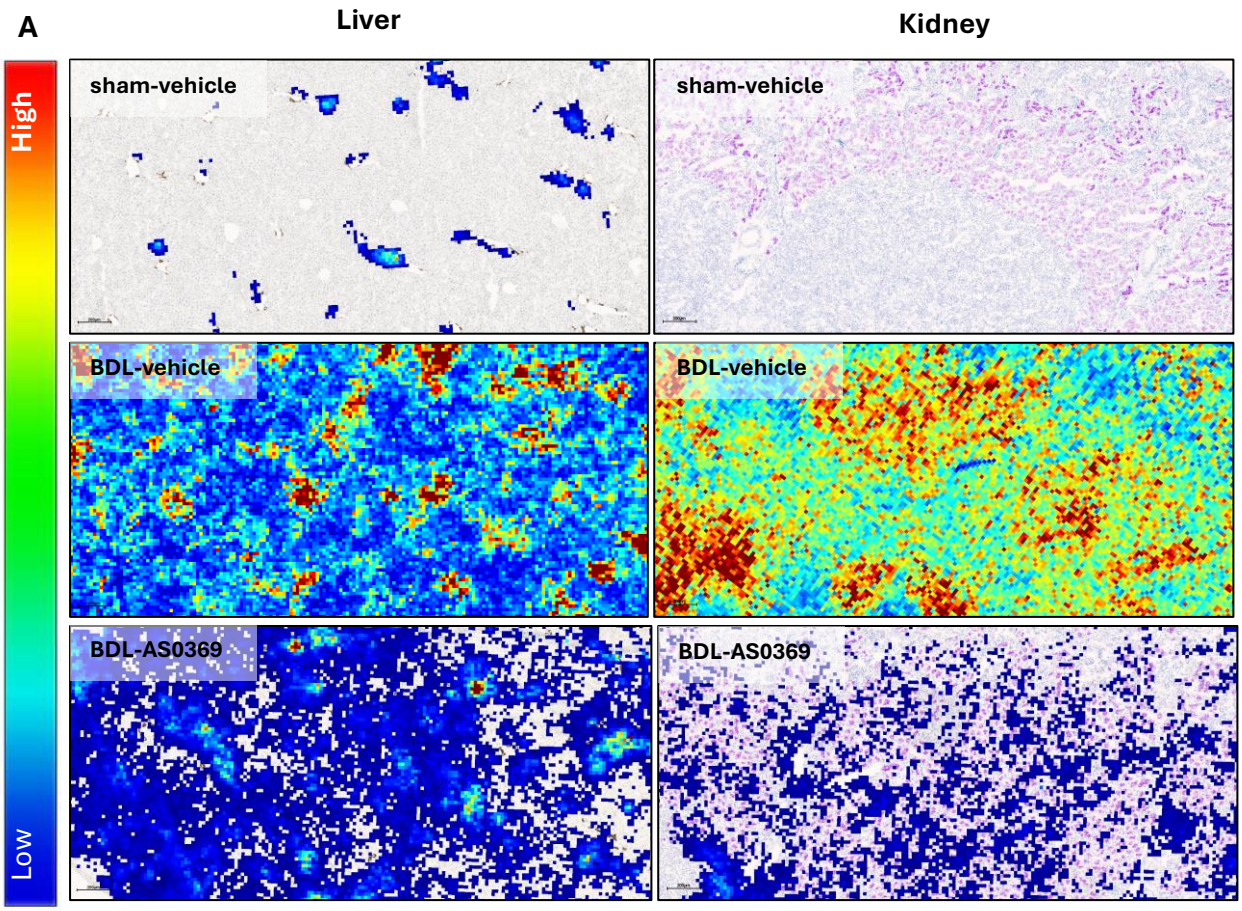
A
Liver
Kidney
High
Low
sham-vehicle
sham-vehicle
BDL-vehicle
BDL-vehicle
BDL-AS0369
BDL-AS0369

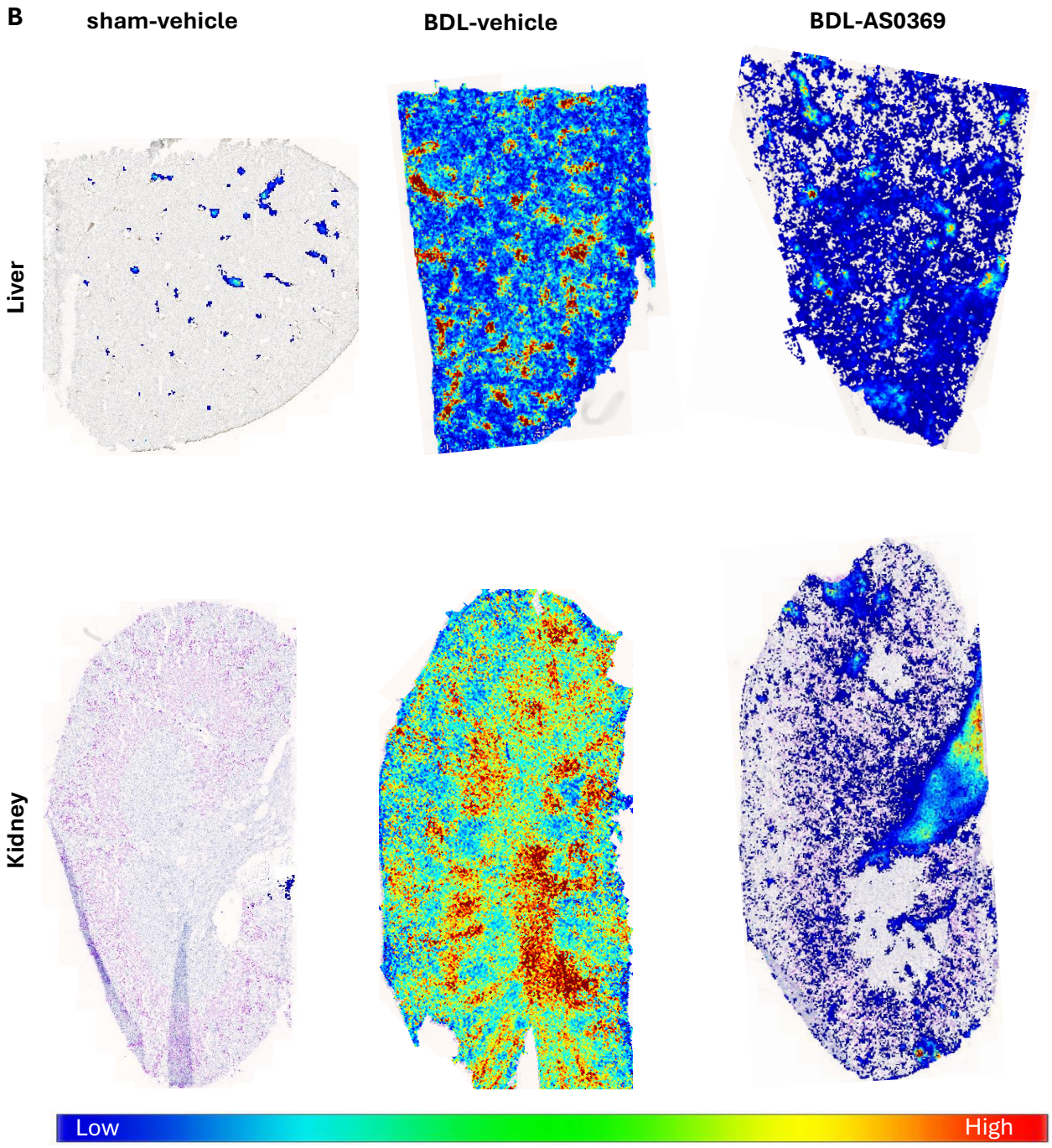

Fig. 41: Images from MALDI-MSI analysis of taurocholic acid in liver and kidney tissues. **A:** Zoom in on MALDI-MSI analysis of taurocholic acid in liver and kidney tissues. Scale bars: 200 µm. **B:** Whole slide scans of MALDI-MSI images to obtain an overview of accumulation of taurocholate in liver and kidney tissues. The MALDI-MSI signal was superimposed onto adjacent liver sections stained with CK19 and onto adjacent kidney slices stained with ASBT. These results illustrate the efficacy of the AS0369 by a strong reduction of TCA in AS0369 treated mice. As in the previous images, there is a prevention from the accumulation of TCA in the BDL liver and kidney tissues after AS0369 administration. The data are from female mice and correspond to the three treatment groups (sham-vehicle/ BDL-vehicle/ BDL-AS0369).

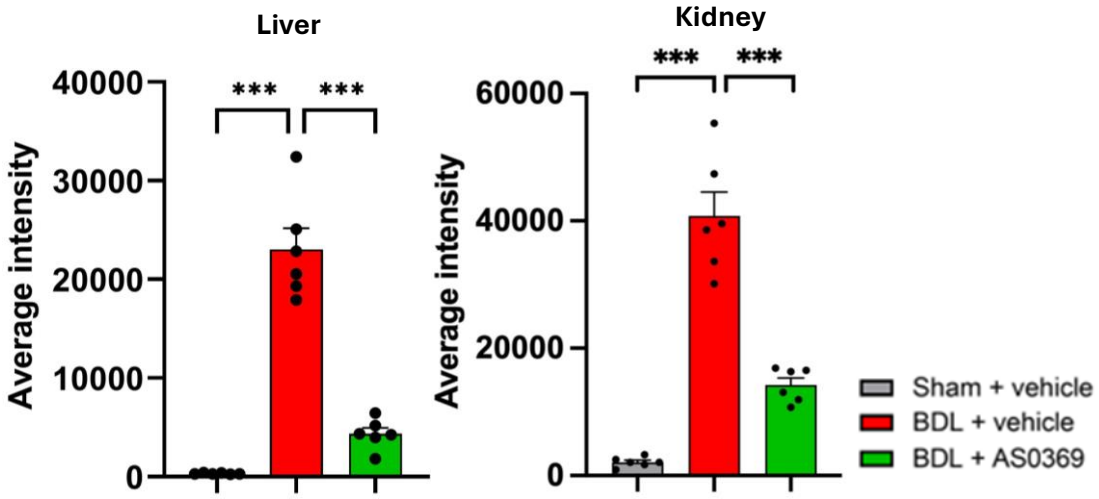

Fig. 42: Quantification of taurocholic acid in liver and kidney tissues using MALDI-MSI analysis. ∗∗∗p <0.001, Tukey's multiple comparisons test. The data are from female mice and correspond to the three treatment groups (sham-vehicle/ BDL-vehicle/ BDL-AS0369).

11.19 Influence of ASBT inhibition on liver and kidney injury markers

To further validate ASBT inhibition with AS0369, I performed analyses to validate biomarkers of liver and kidney injury (Fig. 43, Fig. 44). Starting with the measured damage enzymes in blood, the analysed levels of bilirubin, ALP and urea show a significant improvemnet (Fig. 43). All enzymes are significantly reduced after ASBT inhibition. As an exception, BDL AS0369 mice show comparable levels of ALT and AST to BDL vehicle mice, indicating no effect of ASBT inhibition on these liver damage biomarkers (Fig. 43). In contrast, NGAL, the marker of renal injury, is strongly reduced in urine of BDL AS0369 mice at week 1, and this significant reduction continues until the end of treatment (week 6) (Fig. 44). These results indicate a strong beneficial effect of ASBT inhibition on systemic circulation and kidney injury, in contrast to the liver where there no major effect was obtained, suggesting effective prevention of CN but not of liver damage.

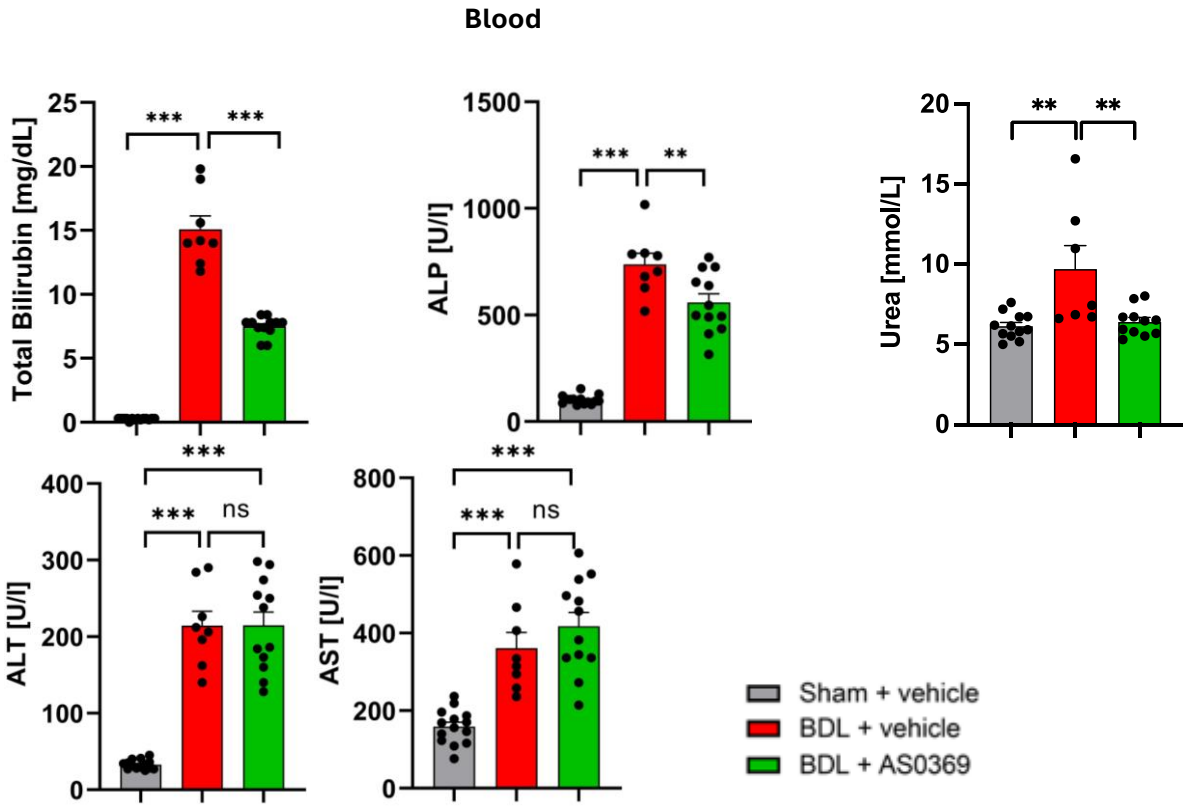

Fig. 43: Quantifications of the biomarkers of liver damage: total bilirubin, alkaline phosphatase, urea, ALT, AST. Total billirubin, ALP and urea show a significant decrease but ALT and AST show results similar to the BDL vehicle mice. $*p < 0.05$, $***p < 0.001$, Tukey's multiple comparisons test. Data are presented as mean ± SEM. The data are from female mice and correspond to the three treatment groups (sham-vehicle/ BDL-vehicle/ BDL-AS0369).

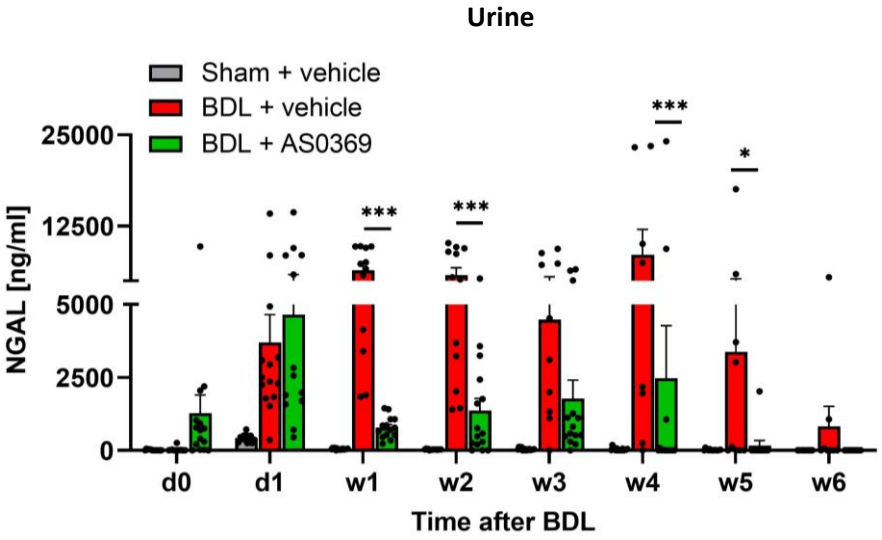

Fig. 44: Quantifications of urine NGAL, a biomarkers of kidney damage. ∗p <0.05, ∗∗∗p <0.001, Tukey's multiple comparisons test. NGAL was significantly reduced after intervention with AS0369. Data are presented as mean ± SEM. The data are from female mice correspond to the three treatment groups (sham-vehicle/ BDL-vehicle/ BDL-AS0369).

11.20 Impact of ASBT inhibition on body, kidney and liver weights

In order to verify whether AS0369 therapy has an influence on body weight, this parameter was measured with and without exclusion of bile volume in the three experimented groups (sham vehicle/ BDL vehicle/ BDL-AS0369) (Fig. 45). Following the exclusion of bile volume, the loss in body weight of BDL mice was effectively counterbalanced by AS0369 treatment (Fig. 45). This finding underscores the potential benefits of ASBT inhibition on mice, highlighting its multifaceted impact on health outcomes.

Same analyses were performed on both kidneys and the liver (Fig. 46). The kidneys demonstrate no variation across the three experimental groups (sham vehicle/ BDL vehicle/ BDL-AS0369) (Fig. 46). However, a compensatory increase in liver weight was observed in response to the loss induced by BDL, as illustrated in Figure 46. The liver of AS0369-treated mice exhibited an increase in weight, in contrast to the BDL vehicle mice (Fig. 46). Thereby, ASBT inhibition treatment resulted in an improvement in body and liver weight, while no effect was observed on kidney weight.

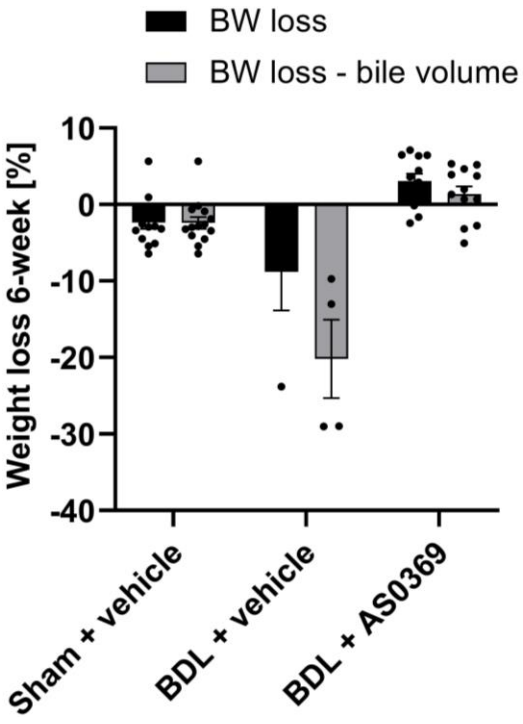

Fig. 45: Body weight of mice was measured with and without exclusion of the bile volume. The female mice correspond to the three treatment groups (sham-vehicle/ BDL-vehicle/ BDL-AS0369). **p< 0.01; ***p< 0.001 compared to the corresponding sham vehicles, Tukey's multiple comparisons test.

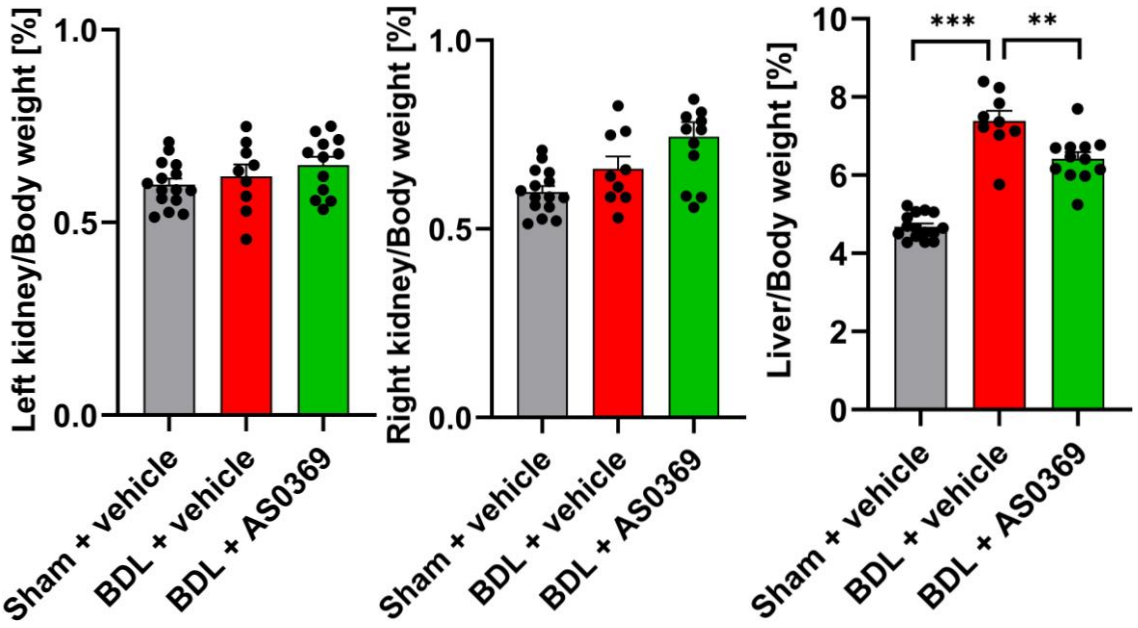

Fig. 46: Alterations in liver-to-body weight and kidney-to-body weight in mice. The female mice correspond to the three treatment groups (sham-vehicle/ BDL-vehicle/ BDL-AS0369). **p< 0.01; ***p< 0.001 compared to the corresponding sham vehicles, Tukey's multiple comparisons test.

11.21 Effect of ASBT inhibition on the histology and the physiology of liver and kidney tissue

The present study examined the influence of ASBT inhibition on the histological modifications due to BDL. To this end, tissue sections from healthy controls (sham vehicle) and from BDL mice livers with and without AS0369 administration were analysed. Initial staining was performed using H&E (Fig. 47). This analysis demonstrated that both BDL conditions resulted in tissue damage in the periportal region of liver lobules, thus suggesting that there was negligible impact of ASBT inhibition on liver tissue in BDL mice. Corresponding observations were made after analysing the CK 19 staining, which demonstrated that the ductular reaction caused by bile duct ligation (BDL) is not ameliorated after the administration of AS0369 (Fig. 47). The infiltrated immune cells shown in CD45 staining in figure 47 are comparable in BDL mice liver with and without AS0369. Furthermore, the results demonstrate that the induced fibrosis after BDL is not ameliorated by AS0369 treatment (Fig. 47). However, an exception to this was noted in the CD13 images, in which a reduction in bile canaliculi dilatation following AS0369 treatment was observed (Fig. 47). In conclusion, the findings demonstrate the ineffectiveness of AS0369, indicating its lack of efficacy in ameliorating or protecting against the development of liver damage.

A similar analysis has been performed on the kidney tissue of healthy controls (sham vehicle) and BDL mice, with and without AS0369 treatment. In contrast to the liver, the damage seen in HE stains after BDL is strongly ameliorated after AS0369 treatment (Fig. 48). Similar trends are observed for the infiltrating immune cells, with a significant decrease in the number of CD45-positive leukocytes (Fig. 48). In addition, AS0369 treatment validates protection from collagen accumulation seen in SR stains in mice kidney tissues after BDL (Fig. 48). Additionally, AS0369 has demonstrated efficacy in addressing the leakiness of endothelial cells triggered by BDL. MECA staining demonstrates the presence of healthy blood vessels in kidneys treated with BDL AS0369, which are not comparable to those observed in kidneys treated with BDL vehicle. Finally, Hall's staining analysis confirmed the protective effect of AS0369 against BDL-induced cast formation in mice (Fig. 48). Collectively, these observations confirm the significant protection against CN development provided by AS0369.

As illustrated in Figure 49, the overview shows the beneficial effect of AS0369 in the kidney of mice after BDL. The data show that BDL-induced tissue damage is considerably reduced. Histological analysis, employing hematoxylin and eosin (H&E) staining, indicates prevention of renal tissue damage in BDL mice after AS0369 treatment (Fig. 49). Whereas SR staining shows a significant reduction in collagen signaling and protection against fibrosis (Fig. 49). Collectively, these observations provide further efficacy evidence for AS0369 in preventing CN as a preventative target in mice.

The quantitative analysis of H&E, SR signal and CD45-positive cells in renal tissue of BDL mice treated and untreated with AS0369 confirmed of the staining seen in Figure 48 (Figure 50). The figures show a significant suppression of damage and fibrosis in AS0369-treated BDL mice, accompanied by a significant reduction in leukocyte infiltration, providing evidence for the efficacy of AS0369 in preventing kidney injury.

Results

In order to evaluate the expression of early growth response protein 1 (Erg1), which plays a critical role in kidney fibrogenesis, analysis of this protein was conducted (Fig. 51). The results obtained were consistent with the most positive outcomes, with Erg1 being found to be overexpressed in kidney tissue following BDL and reduced to control levels after AS0369 treatment (Fig. 51).

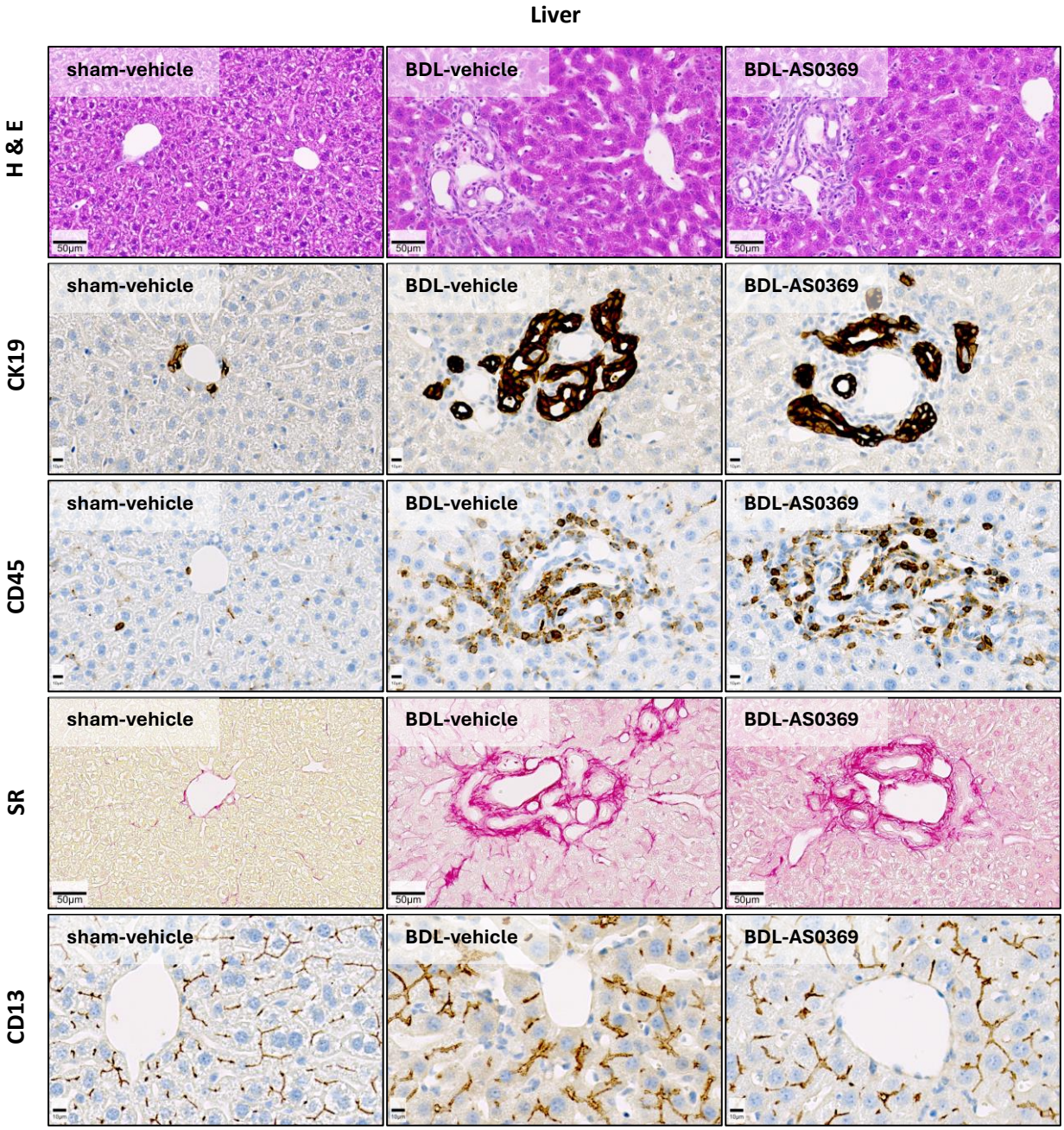

Fig. 47: Effect of ASBT inhibition on liver histopathology. The following histopathological changes were observed: H&E: illustration of damage in liver tissue, CK19: used to improve ductal reaction, CD45: staining of infiltrating immune cells induced by BDL, SR: investigation of induced fibrosis after BDL and CD13: improvement of damage in bile canaliculi. The female mice correspond to the three treatment groups (sham-vehicle/ BDL-vehicle/ BDL-AS0369). Scale bars: H&E, SR: 50 µm; CK19, CD45, CD13: 10 µm.

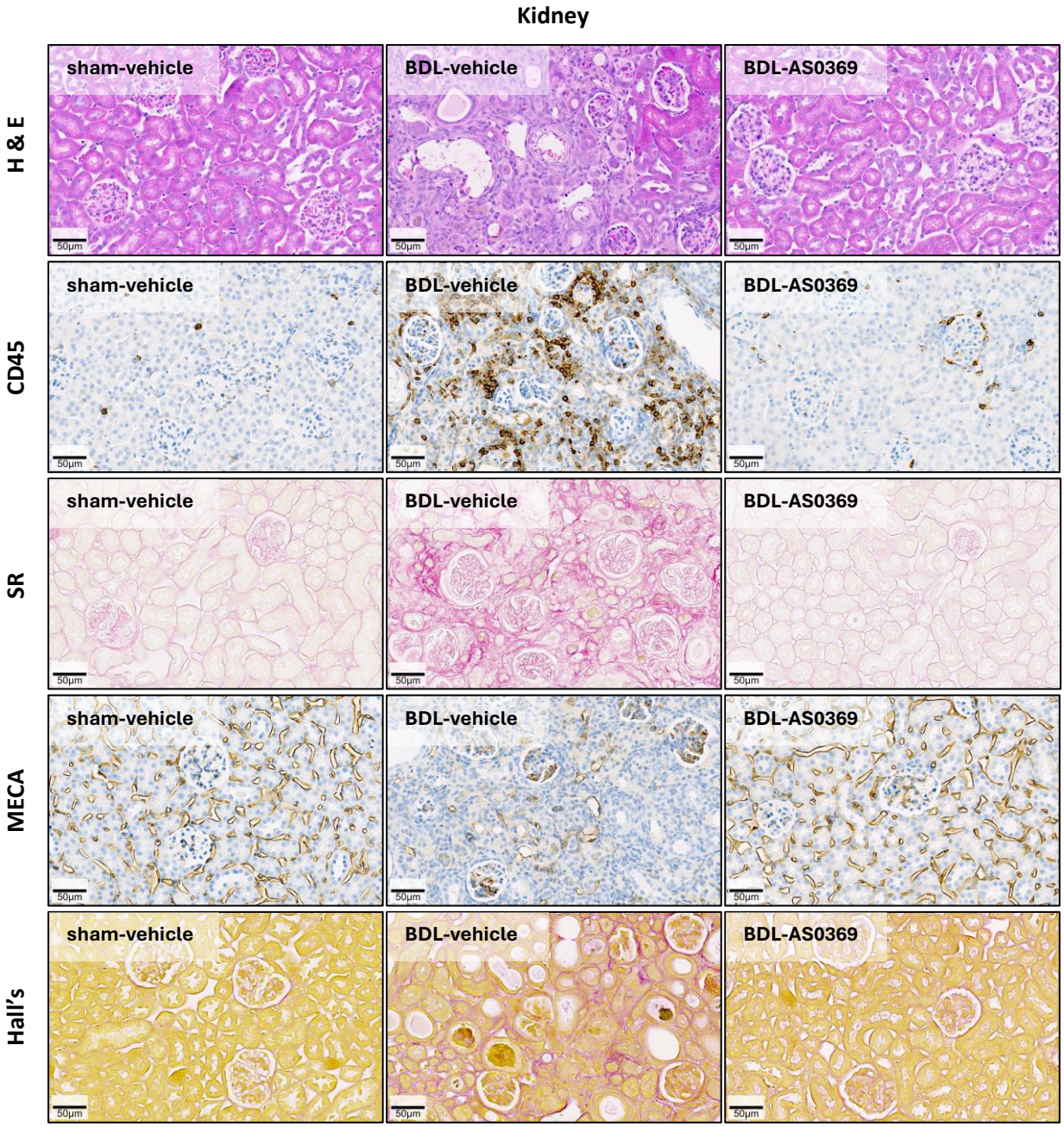

Fig. 48: The consequences of ASBT inhibition on kidney histopathology. The subsequent histopathological alterations were identified: H&E: demonstration of renal tissue damage, CD45: staining of infiltrated immune cells induced by BDL, SR: investigation of induced fibrosis after BDL, MECA: improvement of damage in endothelial cells. Hall's: validation of cast formation in tubular epithelial cells. The female mice correspond to the three treatment groups (sham-vehicle/ BDL-vehicle/ BDL-AS0369). Scale bars: 50 µm.

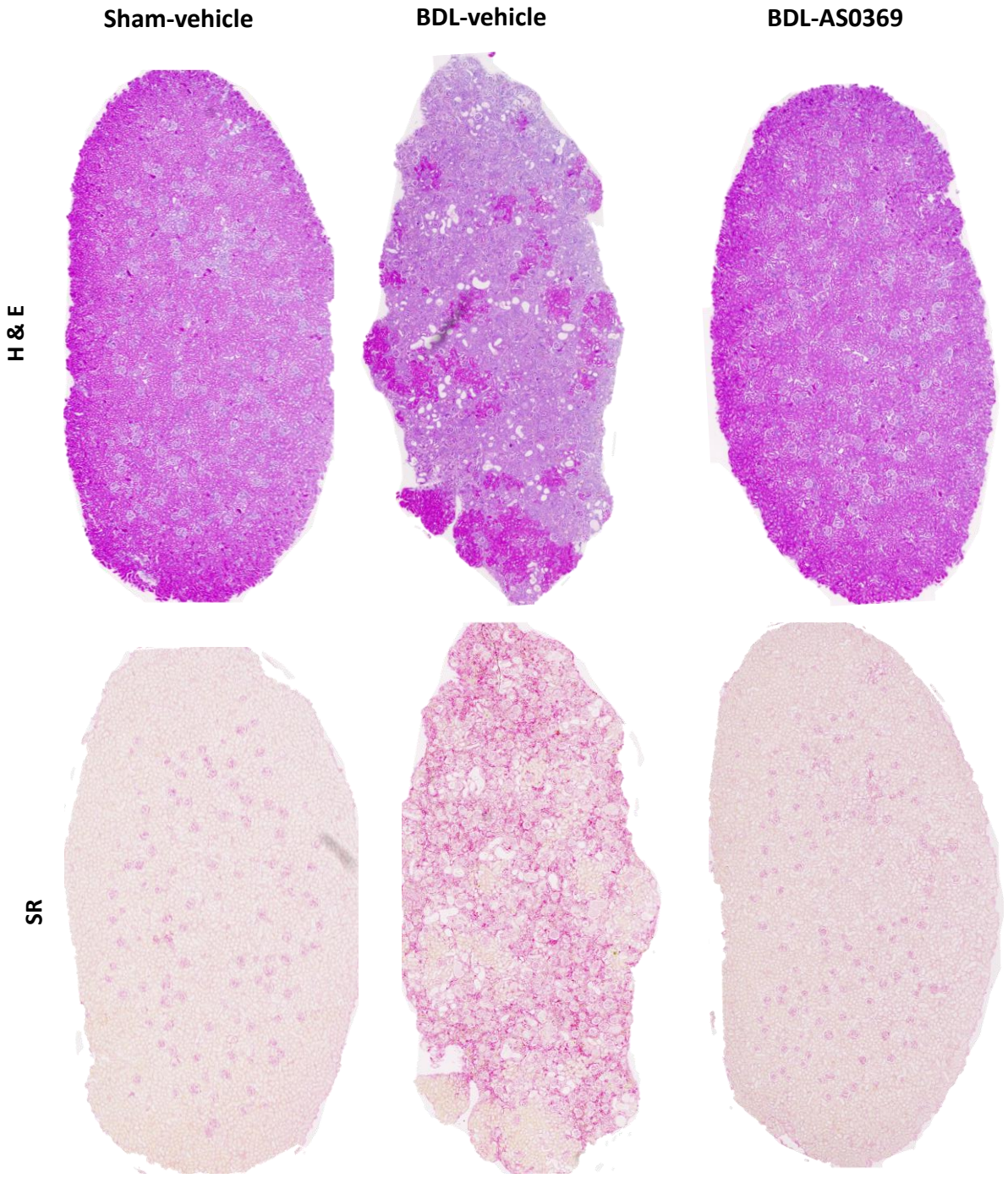

Fig. 49: Overview of the histopathological changes in kidneys. H&E: evidence of kidney tissue damage, SR: examination of fibrosis in kidney of mice after BDL. The female mice correspond to the three treatment groups (sham-vehicle/ BDL-vehicle/ BDL-AS0369).

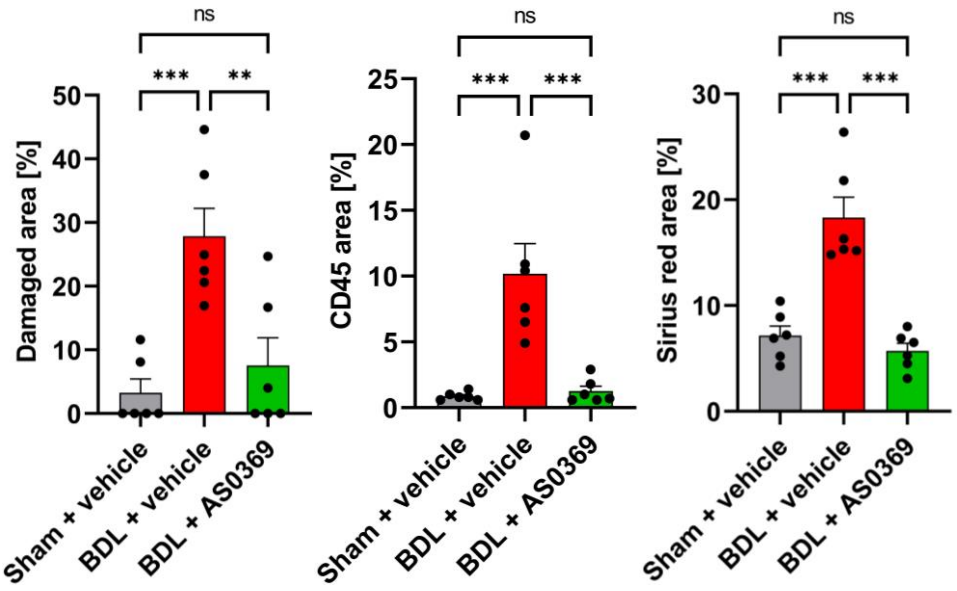

Fig. 50: Quantification of SR and CD45 stains performed in kidney tissue for BDL mice with and without AS0369. The results confirm the observations in Figure 54 with a clear decrease in both stains after AS0369 in BDL mice. $*p$ <0.05, $**p$ <0.01, $***p$ <0.001; Tukey's multiple comparisons test. Data are presented as mean ± SEM. The female mice correspond to the three treatment groups (sham-vehicle/ BDL-vehicle/ BDL-AS0369).

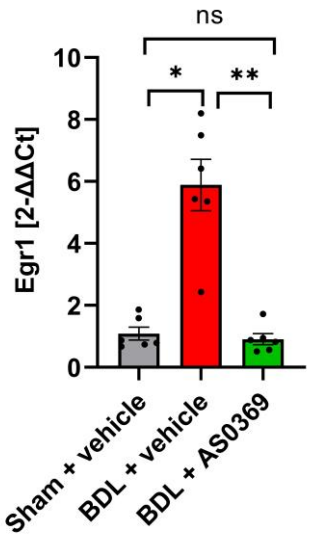

Fig. 51: RNA levels of *Egr1* in renal tissue. $*p$ <0.05, $**p$ <0.01, $***p$ <0.001; Tukey's multiple comparisons test. Data are presented as mean ± SEM.

11.22 Effect of ASBT inhibition on the leakiness in kidney of mice after BDL

As previously referenced, Evans blue, a magenta dye, has historically been utilised as a means of visualising leaky capillaries through intravenous injection. Following intravenous injection, Evans Blue is retained within the lumen of intact capillaries (Fig. 52). However, when capillaries become leaky, the dye leaks into the adjacent interstitium (Fig. 52). Utilising this technique, it was demonstrated that leaky renal capillaries in BDL vehicle mice are prevented by AS0369 administration (Fig. 52).

The analysis of intravital video images revealed a robust signal within the capillaries and an almost negative signal in the interstitium in the sham mice (Fig. 53). Conversely, a marked enhancement in the signal intensity has been observed in both blood capillaries and interstitium six weeks post-BDL (Fig. 53). This enhancement is successfully antagonised, and the leakiness is strongly ameliorated after AS0369 treatment. This finding illustrates and confirms the inhibition of interstitial fluid leakage from the peritubular capillaries.

In order to characterise the interstitial tissue into which Evans blue leaked (Fig. 54), a combined intravital imaging of Evans blue (magenta) and Rhodamine 123 (green) was performed (Fig. 54). It was observed that Evans blue leaked into tissue domains that were Rhodamine 123 negative, and that these domains exhibited improved functionality following administration of AS0369. The BDL AS0369 group exhibited a reduced presence of dead tissue, which was comparable to the signal observed in the healthy control (sham vehicle) group. This finding serves to reinforce the substantial impact of ASBT inhibition on the reduction of capillary leakiness.

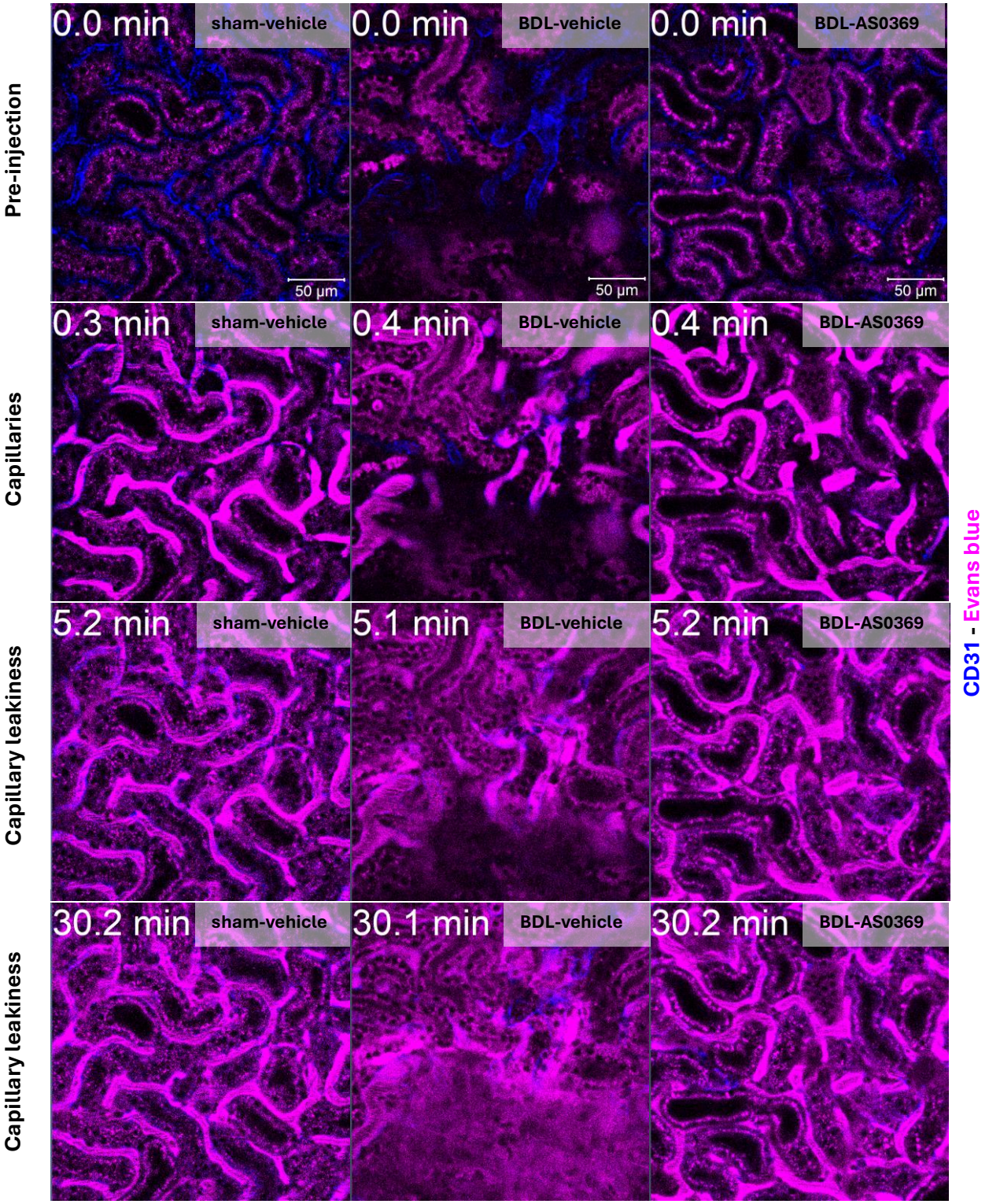

Fig. 52: Leakiness of peritubular capillaries was observed six weeks after BDL. Intravital imaging was performed following the injection of Evans blue (magenta). Blue into the tail vein. Peritubular capillaries are visualized by anti-CD31 antibody (blue); scale bars: 50 µm. Data are presented as mean ± SEM; n = 5 mice per group. $*p$ <0.05; $**p$ <0.01; $***p$ <0.001 compared to the corresponding sham controls; Tukey's multiple comparisons test. The data are from female mice correspond to the three treatment groups (sham-vehicle/ BDL-vehicle/ BDL-AS0369).

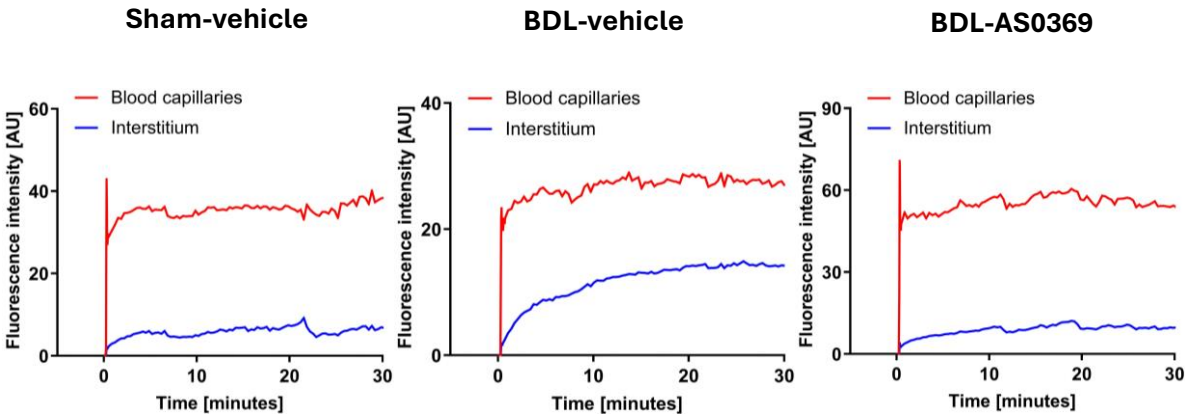

Fig. 53: The signal of Evans blue is quantified in the peritubular capillaries and in the interstitium according to the intravital videos. Data are presented as mean ± SEM; n = 5 mice per group. ∗p <0.05; ∗∗p <0.01; ∗∗∗p <0.001 compared to the corresponding sham vehicles; Tukey's multiple comparisons test. The data from female mice correspond to the three treatment groups (sham-vehicle/ BDL-vehicle/ BDL-AS0369).

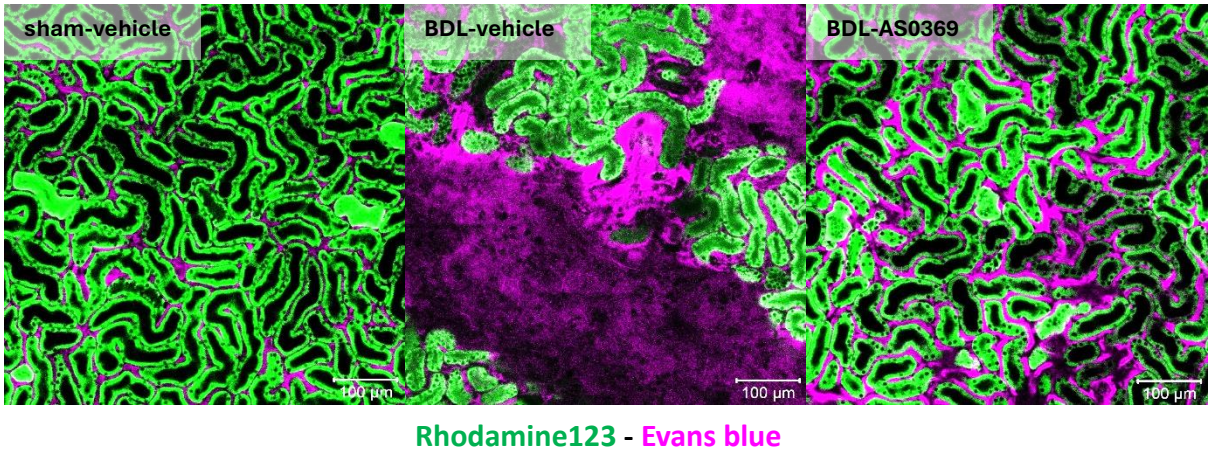

Fig. 54: Overview of intravital imaging following the tail vein injection of Evans Blue in mice. This technique illustrates leakiness of peritubular capillaries under control condition (sham-vehicle) and after 6 weeks of bile duct ligation (BDL) with vehicle (BDL-vehicle) or AS0369 treatment (BDL-AS0369). Evans Blue (Magenta); Rhodamine 123 (Green). Scale Bars: 100 µm.

11.23 The impact of ASBT inhibition on the histology and physiology of liver and kidney tissue in male mice

Given that the primary intervention study was conducted in female mice, a decision was taken to replicate the intervention experiment using male mice. However, urine was only

collected at the completion of the 6-week treatment period. Following the collection of samples, the influence of ASBT inhibition on the histological modifications due to BDL was analysed by examining tissue sections from BDL mice livers with and without AS0369 administration. Initial staining was performed using H&E (Fig. 55). This analysis illustrated the tissue damage in the periportal region of liver lobules in both conditions, suggesting the negligible impact of ASBT inhibition on liver tissue of BDL mice. Conclusive observations were made after analysing the CK 19 staining, which demonstrated that the ductular reaction caused by BDL is not ameliorated after AS0369 treatment (Fig. 55). The infiltrated immune cells shown in CD45 staining in figure 53 are comparable in BDL mice liver with and without AS0369. Furthermore, the results demonstrate that the induced fibrosis after BDL is not ameliorated by AS0369 treatment (Fig. 55). An exception to this is observed in CD13 images, wherein the bile canaliculi demonstrate a reduction in dilatation following AS0369 treatment. This finding indicates that AS0369 does not provide any amelioration or protection against the development of cholestasis, with the exception of bile canaliculi. Furthermore, this demonstrates that this effect is not sex specific.

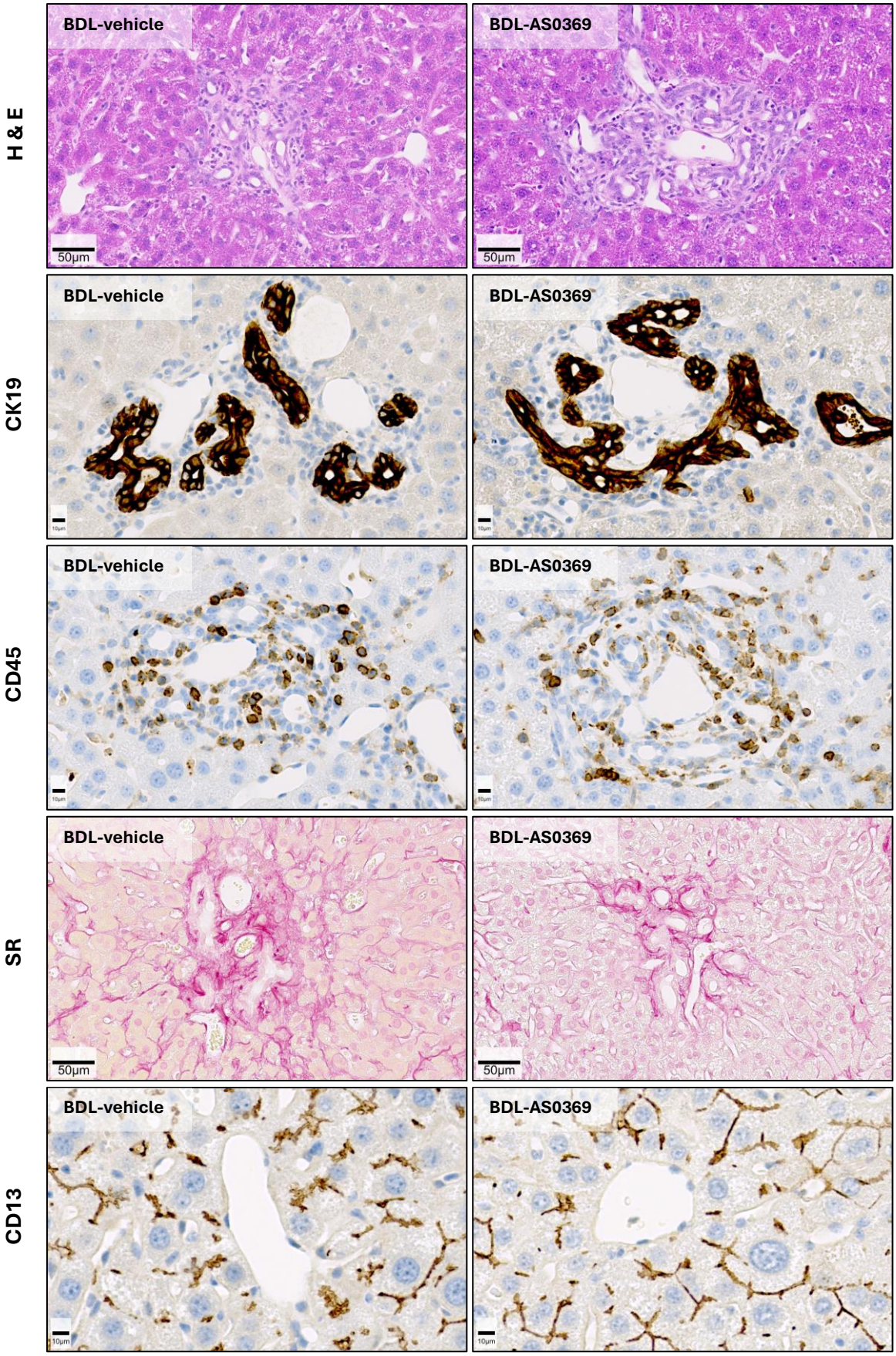

Fig. 55: The impact of ASBT inhibition on hepatic histopathology. Following histopathological alterations were identified: H&E: illustration of damage in liver tissue,

CK19: used to improve the ductular reaction, CD45: staining of infiltrated immune cells induced by BDL, SR: investigation of induced fibrosis after BDL and CD13: improvement of damage in bile canaliculi. The male mice correspond to the two treatment groups (BDL-vehicle/ BDL-AS0369). Scale bars: H&E, SR: 50 µm; CK19, CD45, CD13: 10 µm.

The same analysis is applied to the kidney tissue of male BDL mice, both treated and untreated with AS0369. In contrast to the liver, the damage seen in HE stains after BDL is strongly ameliorated after AS0369 treatment (Fig. 56). A similar trend is observed in the infiltrating immune cells, with a significant decrease in the number of CD45-positive leukocytes (Fig. 56). Furthermore, the AS0369 treatment validates protection from collagen accumulation seen in SR stains in mice kidney tissues after BDL (Fig. 56). Furthermore, AS0369 treatment has been shown to effectively mitigate the leakiness of endothelial cells induced by BDL. MECA staining reveals the presence of healthy blood vessels in BDL AS0369-treated kidneys, which are not comparable to those observed in BDL vehicle-treated kidneys (Fig. 56). Finally, analysis of Hall's staining revealed an enhancement in the protective efficacy of AS0369 against cast formation, induced by BDL in mice (Fig. 56). These observations collectively substantiate the considerable protection against CN development provided by AS0369 and demonstrate its non-sex-specific nature.

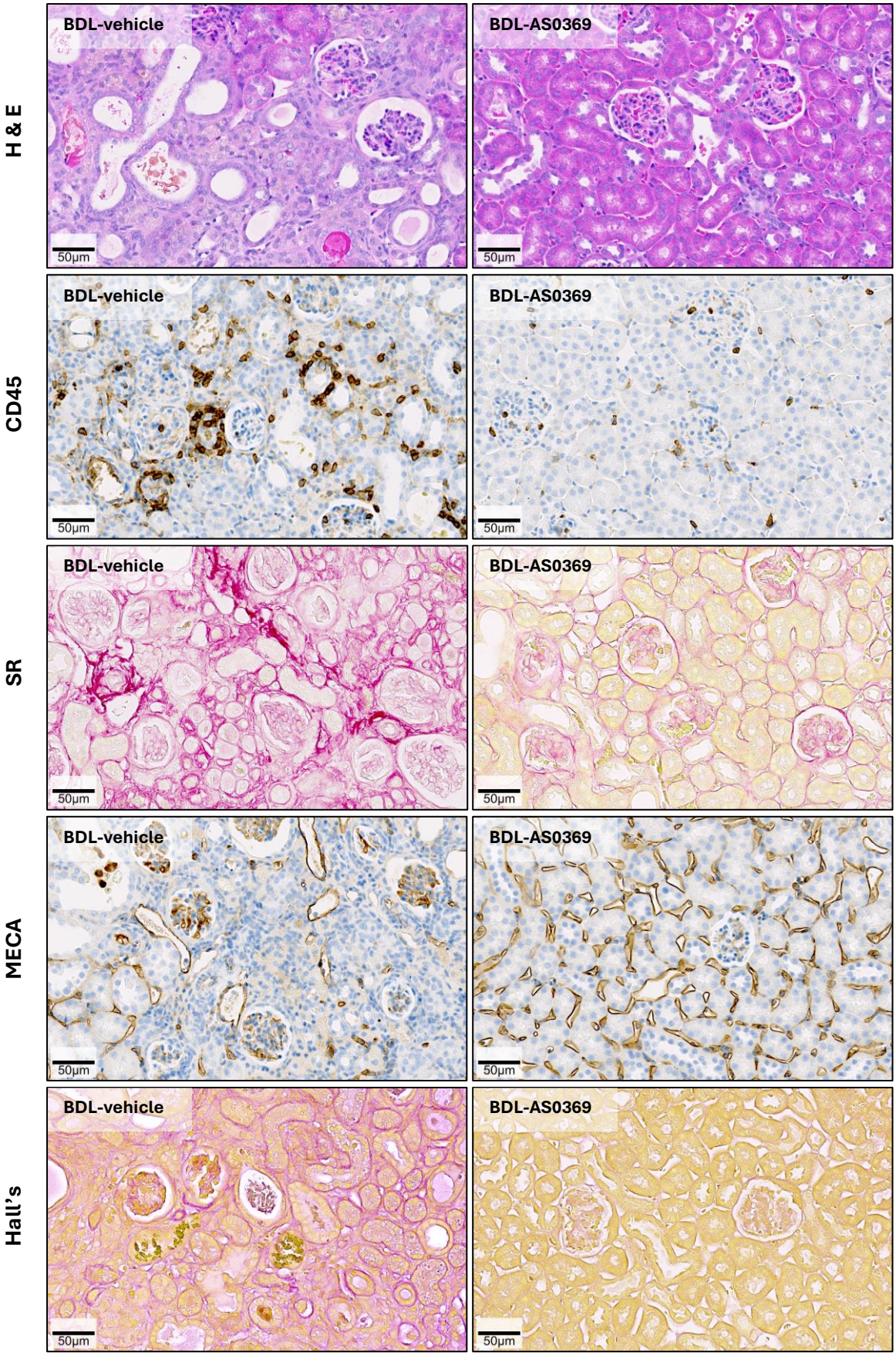

Fig. 56: The consequences of ASBT inhibition on kidney histopathology. The subsequent histopathological alterations were identified: H&E: demonstration of renal tissue

damage, CD45: staining of infiltrated immune cells induced by BDL, SR: investigation of induced fibrosis after BDL, MECA: improvement of damage in endothelial cells. Hall's: validation of cast formation in tubular epithelial cells. The male mice correspond to the two treatment groups (BDL-vehicle/ BDL-AS0369). Scale bars: 50 µm.

In Figure 57, the overview illustrates the beneficial effect of AS0369 in the kidney of mice after BDL. As demonstrated, the damage caused by BDL is significantly reduced. H&E staining reveals a prevention of renal tissue damage in BDL mice after AS0369 treatment, while SR staining demonstrates a substantial decrease in collagen signal and protection from fibrosis. These findings provide further evidence for the efficacy of AS0369 in inhibiting CN in mice.

The quantification of SR signal and CD45-positive cells in renal tissue in BDL mice treated and untreated with AS0369 confirmed the staining seen in Figure 56 (Fig. 58). The data demonstrate a significant reduction in fibrosis in BDL mice treated with AS0369, accompanied by a substantial decrease in leucocyte infiltration, thereby providing evidence for the efficacy of AS0369 in preventing kidney injury.

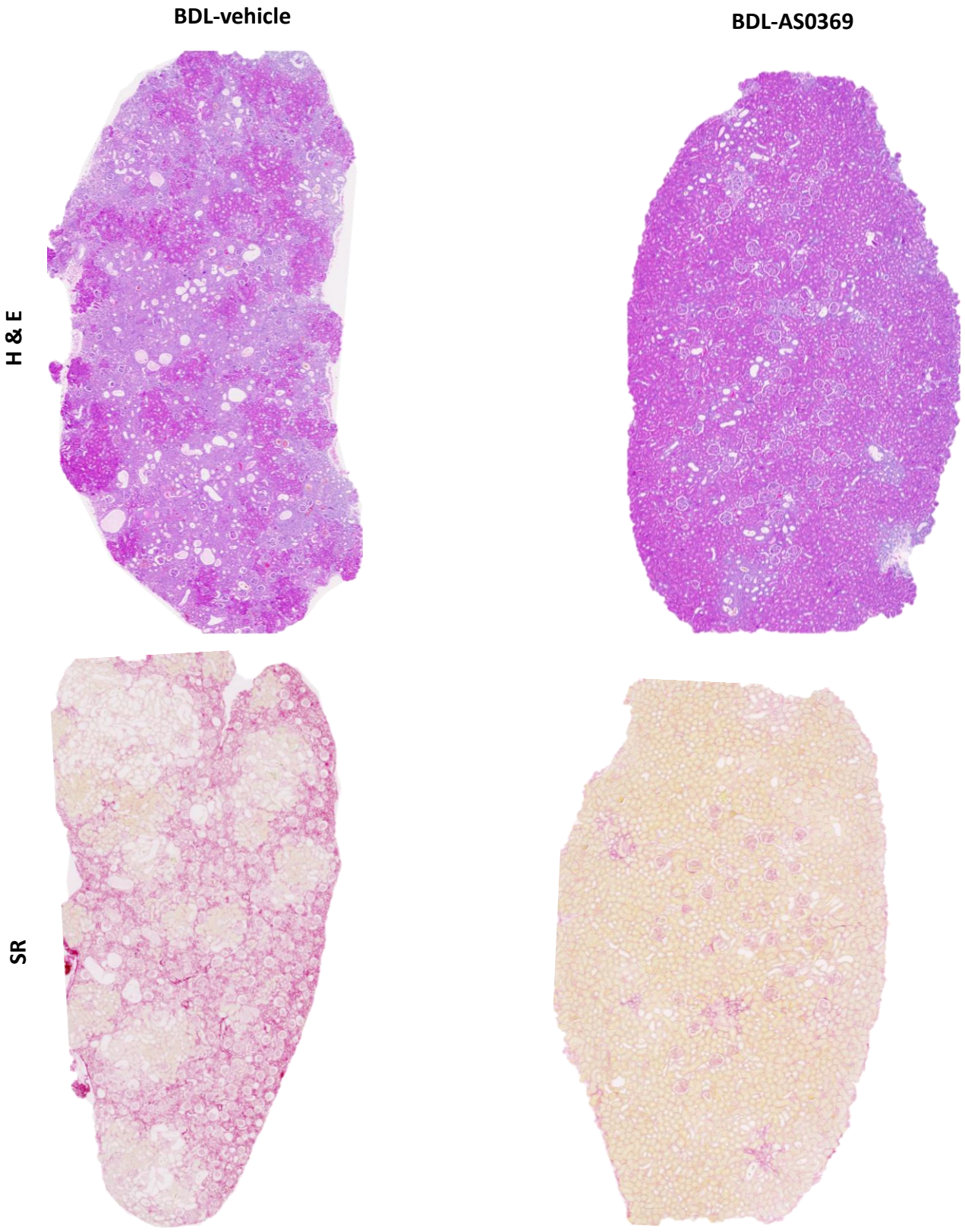

Fig. 57: Overview of the histopathological changes in kidneys were identified. H&E: evidence of renal tissue damage, SR: examination of induced fibrosis after BDL. The male mice correspond to the two treatment groups (BDL-vehicle/ BDL-AS0369).

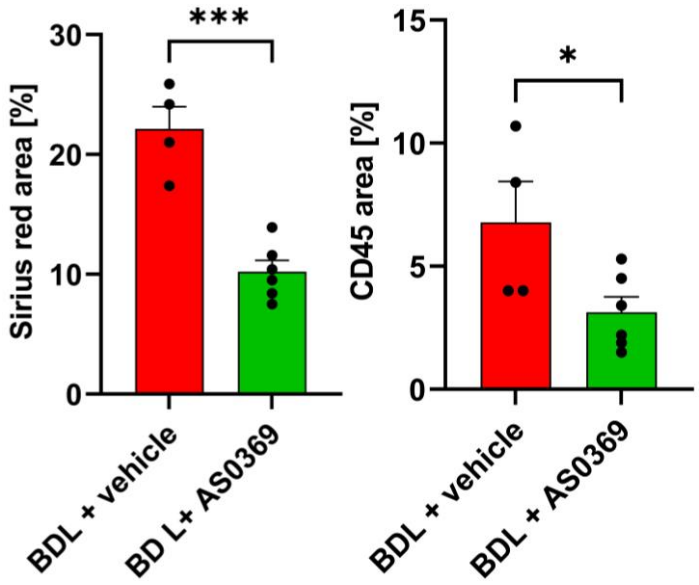

Fig. 58: Quantification of SR and CD45 stains in kidney tissue for BDL mice with and without AS0369. The results confirm the observations in Figure 54 with a clear decrease in both stains after AS0369 in BDL mice. The male mice correspond to the two treatment groups (BDL-vehicle/ BDL-AS0369). $*p$ <0.05, $**p$ <0.01, $***p$ <0.001; Tukey's multiple comparisons test. Data are presented as mean ± SEM.

11.24 Examination of RNA levels of bile acid and of Cyp7a1 in the liver after ASBT inhibition

In the subsequent stage of the study, the impact of ASBT inhibition on bile acid transporter and Cyp7a1 expression in the liver was analysed. Firstly, the expression of bile acid transporters and cholesterol 7α-hydroxylase (Cyp7a1), a regulator of bile acid synthesis, was studied at the RNA level (Fig. 59). There is no relevant change in the expression of the sinusoidal uptake transporters Ntcp and Oatp after ASBT inhibition. In addition, the expression of the apical transporters Bsep was numerically reduced but not statistically significantly. Treatment with AS0369 did not result in a significant alteration of bile acid carrier expression in the liver when compared to the BDL vehicle group. However, the BDL-induced upregulation of MRP4 was mitigated in response to AS0369 (Fig. 59). However, Cyp7a1 expression was found to be induced following AS0369 treatment (Fig. 59).

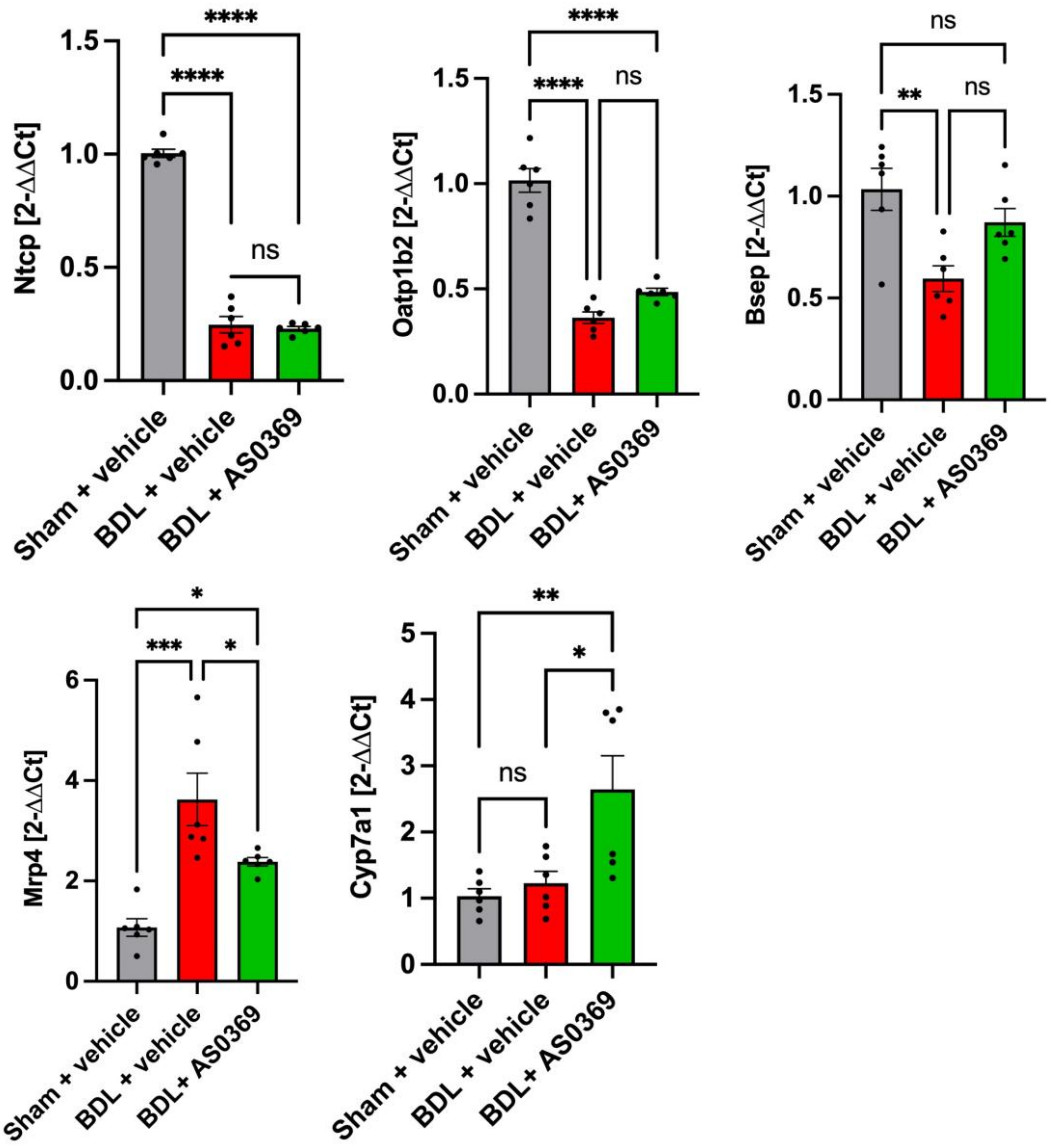

Fig. 59: Illustration of RNA levels of bile acid transporters and of Cyp7a1 in the liver. The mice correspond to the three treatment groups (sham-vehicle/ BDL-vehicle/ BDL-AS0369). p< 0.05; **p< 0.01; ***p< 0.001, ***p< 0.0001 compared to the sham controls, Dunn's multiple comparisons test.

11.25 Examination of RNA levels of bile acid in the kidney after ASBT inhibition

Analogous to the liver, the impact of ASBT inhibition on bile acid transporter expression in the kidney was examined (Fig. 60). In contrast to the liver, the results demonstrated that BDL mice treated with AS0369 exhibited an improved expression of bile acid transporters in the kidney, with comparable results to the control mice (sham-vehicle) (Fig.60). However, MRP4 upregulation due to BDL exhibited a very weak transition. In renal tissue, the administration of AS0369 prevented the BDL-induced dysregulation of BA carrier expression, with the exception of Mrp4 (Fig. 60).

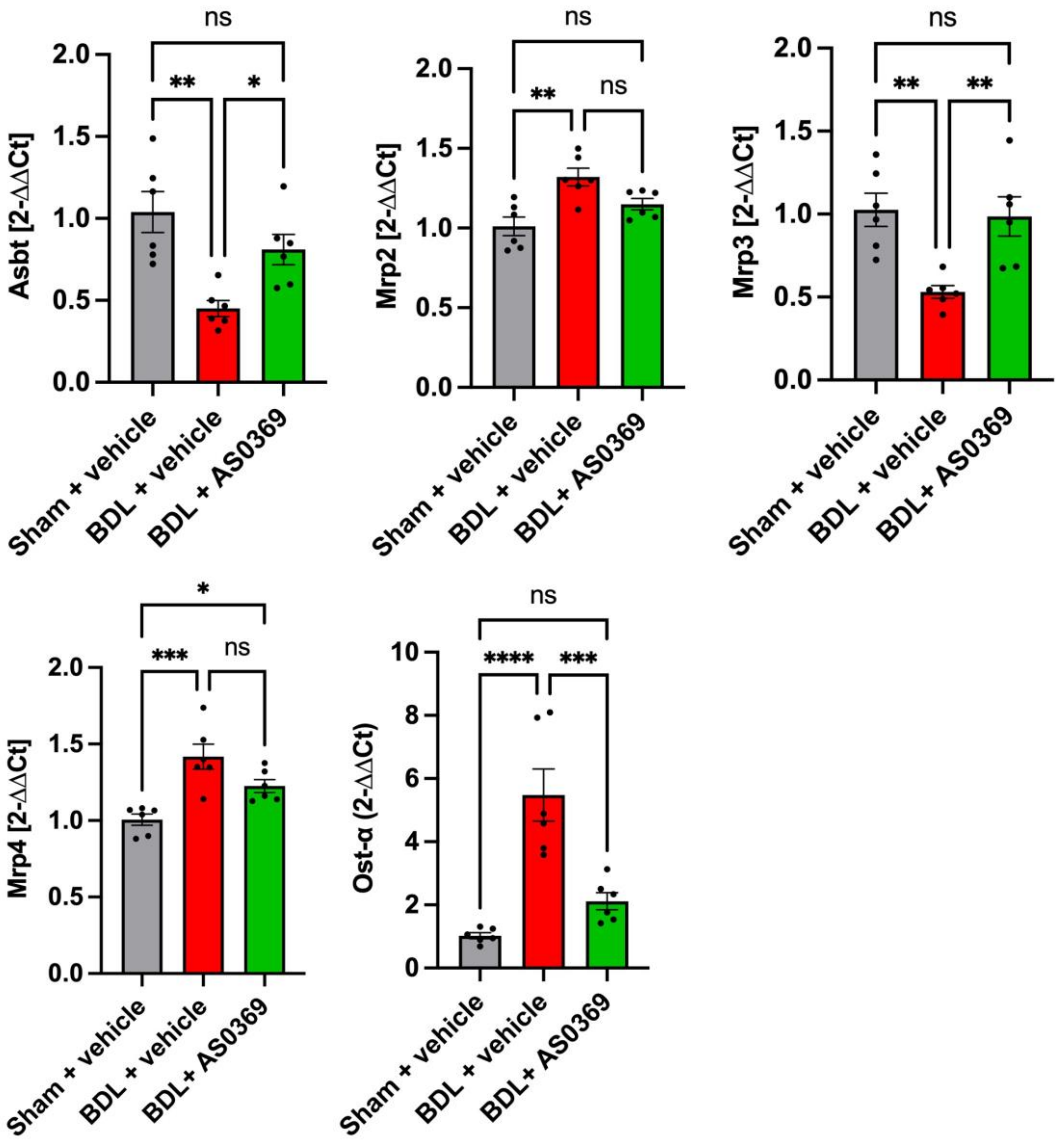

Fig. 60: Investigation and illustration of RNA levels of bile acid transporters in kidney tissue. The mice correspond to the three treatment groups (sham-vehicle/ BDL-vehicle/ BDL-AS0369). *p< 0.05; **p< 0.01; ***p< 0.001, ***p< 0.0001 compared to the sham controls, Dunn's multiple comparisons test.

11.26 RNA-sequencing analysis of renal tissue

In a last step RNA-sequencing (RNA-seq) of the renal tissue of control mice (sham-vehicle), mice six weeks after BDL treated with vehicle (BDL-vehicle) and mice with BDL treated with AS0369 (BDL-AS0369) was performed. To obtain an overview of the genome wide expression patterns a principal component analysis was performed (PCA) (Fig. 61, A). In this PCA analysis each dot represents the kidney tissue of an individual mouse. Interestingly, BDL-vehicle and sham-vehicle mice show the largest difference (Fig. 61, A). Treatment with the ASBT inhibitor (BDL-AS0369) leads to a shift of the samples closer to the controls suggesting efficacy of the therapy.

This result was confirmed by volcano plot analysis, where the fold-change between BDL-vehicle and sham-vehicle was plotted on the x-axis and the corresponding p-values on the y-axis (Fig. 61, B). In this analysis each dot represents a single gene. Interestingly, the ASBT inhibitor therapy (right panel) strongly reduced the difference to the sham-vehicle mice.

To characterise the therapeutic effect of the ASBT inhibitor in more detail, a differential expression pattern plot analysis (DiPa) was performed, as recently established by Nell et al., 2022 (Fig. 61, C)[31]. In DiPa plot the ratio of BDL-vehicle versus sham-vehicle was plotted on the x-axis; the ratio of BDL-AS0369 versus sham-vehicle on the y-axis. Each dot represents an individual gene. This type of plot allows an evaluation of the therapeutic efficacy of AS0369. If there would be no efficacy all genes would cluster close to the diagonal, shown in red (Fig. 61, C). If the therapeutic effect of AS0369 would be perfect all genes would cluster into the DiPa regions 1b and 1a. In the present experiment, an intermediate result was obtained. A relatively large number of genes clustered to DiPa region 1a and 1b. However, further genes were found in 2a and 2b, indicating an amelioration by therapy but not improvement to the level of mice without BDL. Importantly, for only very few genes ASBT inhibition led to a worse situation compared to BDL-vehicle.

In conclusion the genome wide analysis confirmed the previous data that ASBT inhibition improves the situation of BDL induced cholestasis.

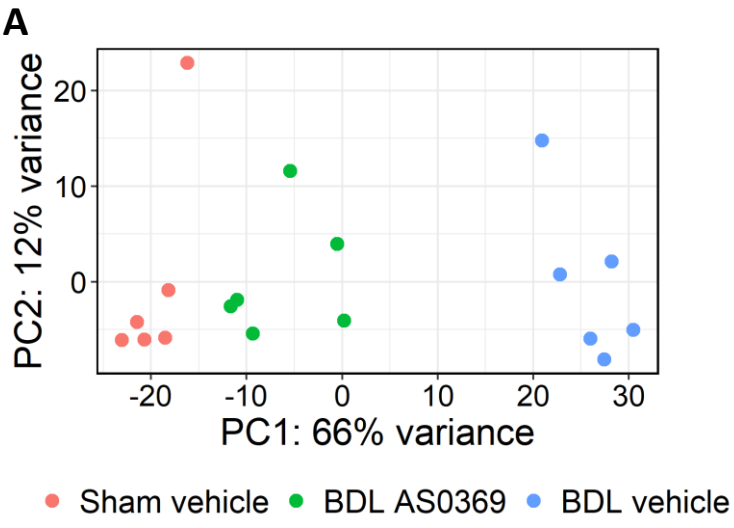

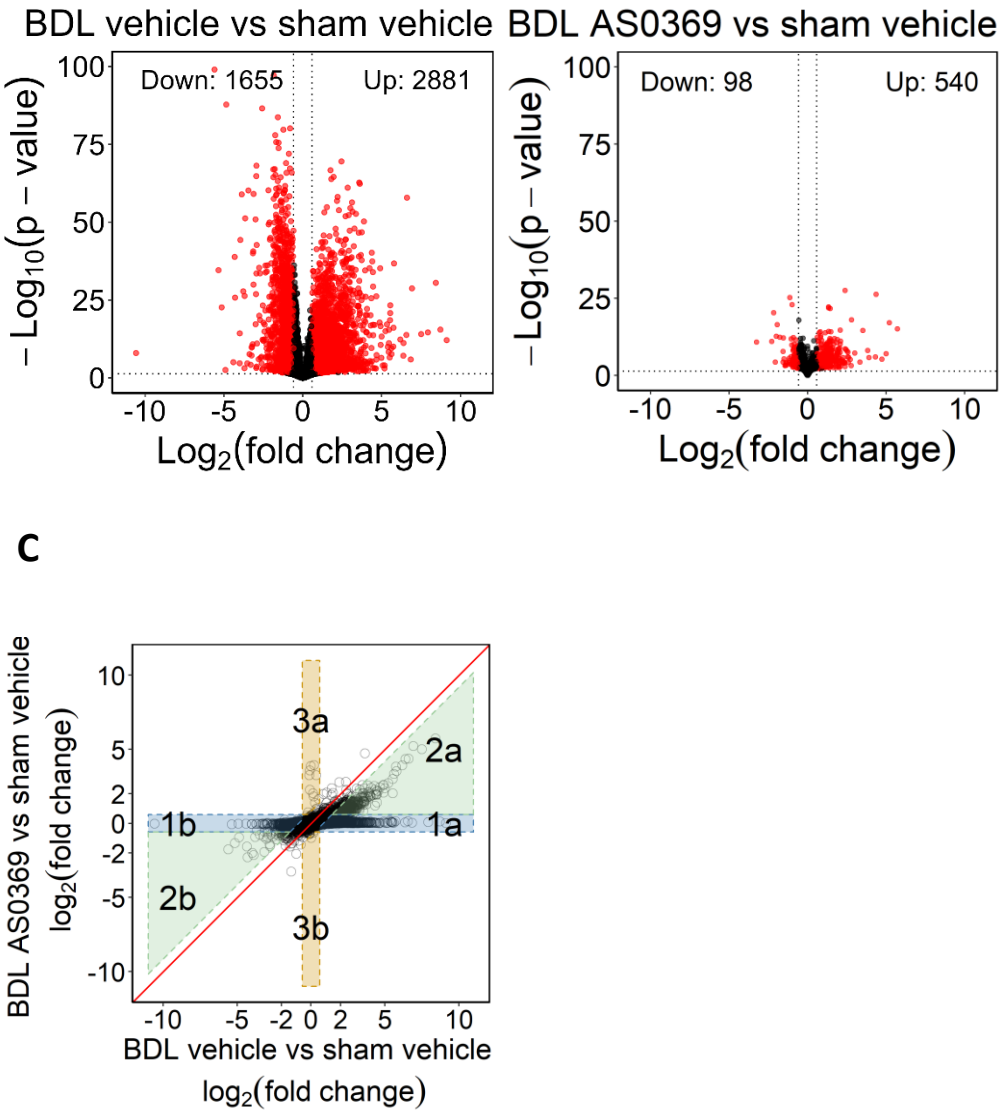

Fig. 61: Validation of the preventive effect of ASBT inhibition based on RNA-seq results of BDL mice in kidney with and without AS0369 treatment. (A) PCA plots of sham vehicle mice, vehicle-treated BDL mice and AS0369-treated BDL mice. (B) Volcano plots showing differential genes between vehicle-treated (left panel) and AS0369-treated (right panel) BDL mice and controls (sham vehicle). (C) DiPa plots illustrating protection by AS0369 treatment. Each point represents a single gene. The female mice correspond to the three treatment groups (sham-vehicle/ BDL-vehicle/ BDL-AS0369).

12 Discussion

The data of my PhD thesis led to a so far unrecognised mechanism how increased bile acids in the systemic circulation cause kidney injury and how this disease can be treated. These data have already been extensively discussed in Ghallab et al. in 2024[1]. Here, I will only summarise key aspects of the new concept.

In healthy livers bile acids are taken up from the blood into hepatocytes (Fig. 62). Next, hepatocytes secrete the bile acids into bile canaliculi from where they travel downstream the biliary tract, finally reaching the small intestine[34]. In cholestasis hepatocytes are no longer able to absorb bile acids from the sinusoidal blood (Fig. 62)[35]. Therefore, bile acids concentration massively increases in the systemic circulation[1]. Consequently, more bile acids enter the renal glomeruli and are filtered into the tubular lumen. From the tubular lumen they are taken by proximal tubular epithelial cells. My data have shown that increased tubular bile acids concentrations lead to higher intracellular bile acids concentrations in proximal tubular epithelial cells that may cause cytotoxicity. These cytotoxic events of proximal tubular epithelial cells represent an early key event of kidney injury.

This concept was further validated by the use of an ASBT inhibitor (Fig. 63). Importantly, ASBT inhibition in cholestasis caused a strong increase of the urinary excretion of bile acids.

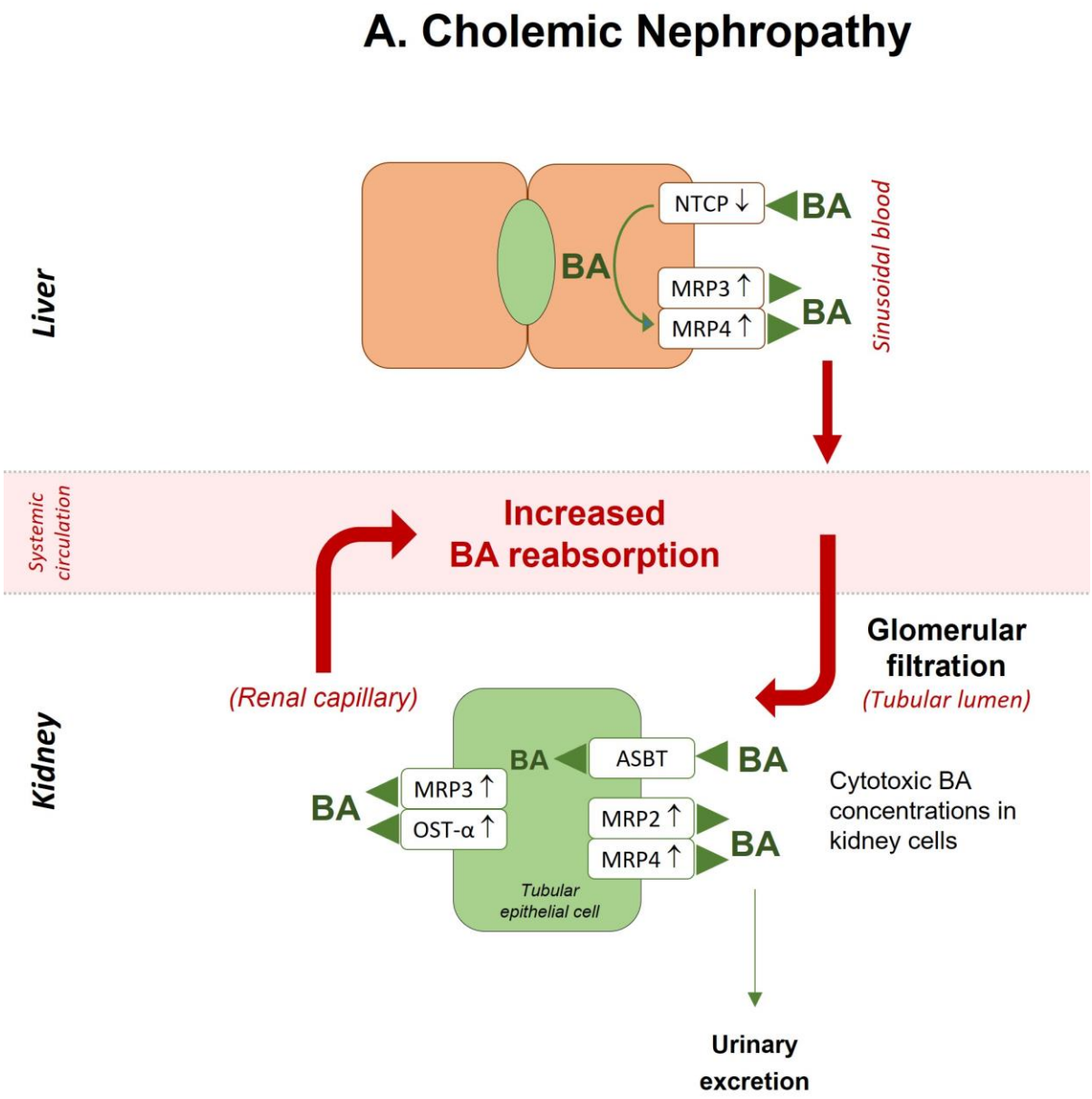

Fig. 62: The graphical abstract shows the key events that lead to cholemic nephropathy. It illustrates the elevated concentrations of cytosolic bile acids in tubular epithelial cells, which are known to cause kidney damage. Furthermore, it demonstrates elevated levels of bile acids in the blood and reduced bile acid excretion in urine. The figure has been modified from Ghallab et al, 2024[1].

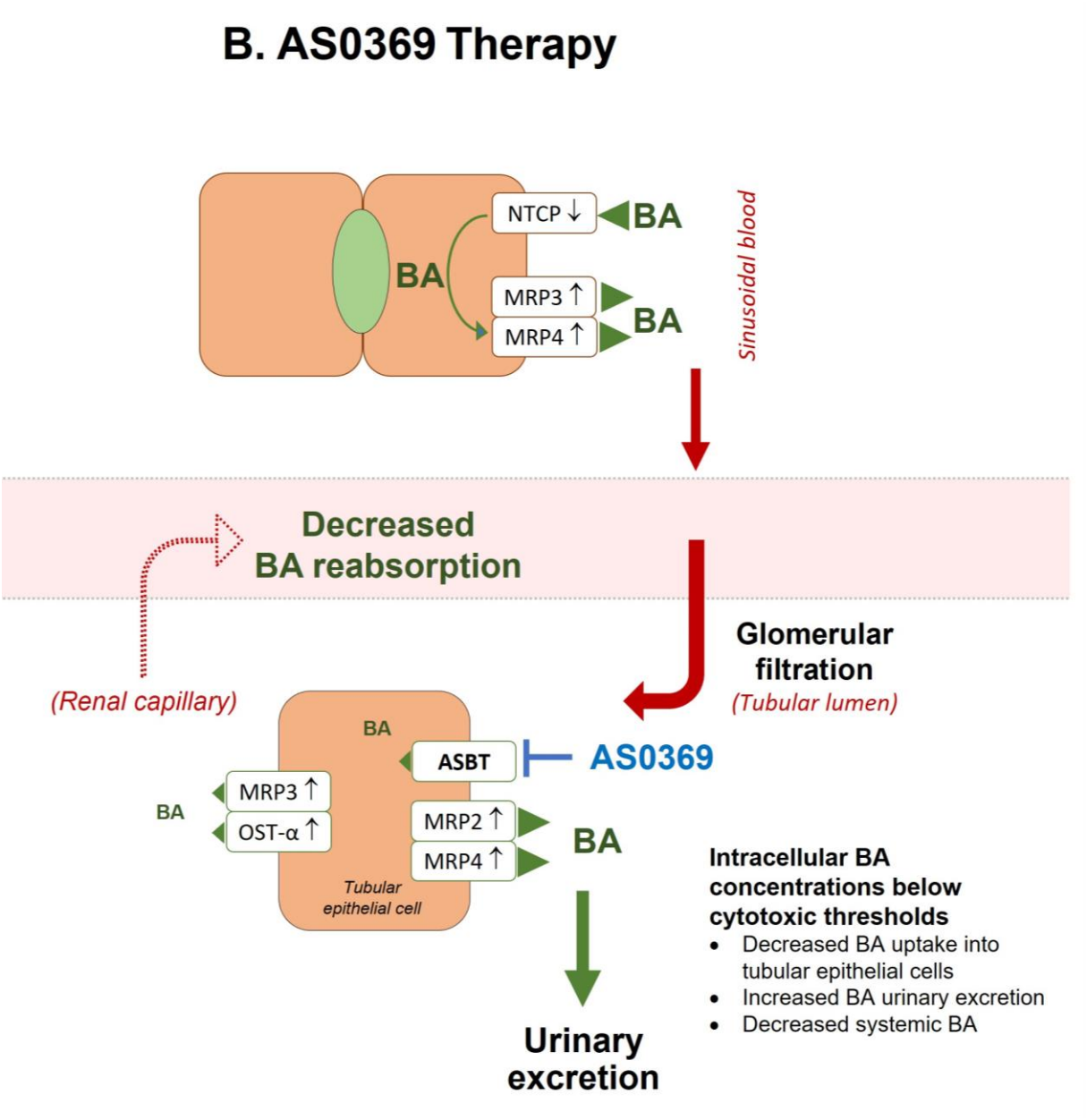

Fig. 63: Principle of ASBT inhibition therapy. This therapy has been shown to result in a decrease in bile acid uptake by tubular epithelial cells, with concentrations of bile acids falling below levels that are toxic to these cells. Additionally, the therapy has been observed to reduce the concentration of bile acids in the blood and to increase the urinary excretion of bile acids. The figure has been modified from Ghallab et al, 2024[1].

Moreover, the accumulation of bile acids in proximal tubular epithelial cells was efficiently prevented. This also allowed to prevent kidney injury.

Therefore, my results demonstrate that inhibition of ASBT in the kidney leads to two critical therapeutic effects (Fig.63):

- Uptake and accumulation of bile acids into proximal tubular epithelial cells is prevented. Thereby, no cytotoxicity occurs in the target cells of this disease.
- Urinary excretion of bile acids is increased. Thereby, the systemic bile acid load is decreased. Due to these therapeutic effects systemic ASBT inhibitors represent a promising perspective to treat the complications of cholestatic liver diseases.

13 Perspective

A limitation of the here presented results is that ASBT inhibitor administration was initiated at the same day when BDL was performed. Therefore, only a preventive but not a therapeutic effect was proven. To address this shortcoming, I used an experimental schedule where ASBT inhibition was initiated at different periods (up to 9 weeks) after BDL.

Interestingly, an improvement occurred even if ASBT inhibition was initiated as late as 9 weeks after BDL demonstrating also a therapeutic efficacy. These experiments were finished just recently, and we will summarise them in an independent manuscript.

14 References

1. Ghallab, A., et al., *Inhibition of the renal apical sodium dependent bile acid transporter prevents cholemic nephropathy in mice with obstructive cholestasis*. Journal of Hepatology, 2024. **80**(2): p. 268-281.
2. *EASL Clinical Practice Guidelines for the management of patients with decompensated cirrhosis*. J Hepatol, 2018. **69**(2): p. 406-460.
3. Krones, E., et al., *Cholemic nephropathy - Historical notes and novel perspectives*. Biochim Biophys Acta Mol Basis Dis, 2018. **1864**(4 Pt B): p. 1356-1366.
4. Fickert, P. and A.R. Rosenkranz, *Cholemic Nephropathy Reloaded*. Semin Liver Dis, 2020. **40**(1): p. 91-100.
5. Mandorfer, M. and M. Hecking, *The Renaissance of Cholemic Nephropathy: A Likely Underestimated Cause of Renal Dysfunction in Liver Disease.* Hepatology, 2019. **69**(5): p. 1858-1860.
6. Ariza, X., et al., *Neutrophil gelatinase-associated lipocalin is a biomarker of acute-on-chronic liver failure and prognosis in cirrhosis*. J Hepatol, 2016. **65**(1): p. 57-65.
7. Arroyo, V., et al., *Acute-on-chronic liver failure: A new syndrome that will re-classify cirrhosis*. J Hepatol, 2015. **62**(1 Suppl): p. S131-43.
8. Somagutta, M.R., et al., *Bile Cast Nephropathy: A Comprehensive Review*. Cureus, 2022. **14**(3): p. e23606.
9. Fickert, P., et al., *Bile acids trigger cholemic nephropathy in common bile-duct-ligated mice*. Hepatology, 2013. **58**(6): p. 2056-69.
10. Slijepcevic, D., et al., *Na(+) -taurocholate cotransporting polypeptide inhibition has hepatoprotective effects in cholestasis in mice*. Hepatology, 2018. **68**(3): p. 1057-1069.
11. Woolbright, B.L. and H. Jaeschke, *Inflammation and Cell Death During Cholestasis: The Evolving Role of Bile Acids*. Gene Expr, 2019. **19**(3): p. 215-228.
12. Geier, A., et al., *Principles of hepatic organic anion transporter regulation during cholestasis, inflammation and liver regeneration*. Biochim Biophys Acta, 2007. **1773**(3): p. 283-308.
13. Paolini2., I.V.M.M.A., *Histology, Kidney and Glomerulus*. 2023.
14. Mandorfer, M., et al., *Austrian consensus on the diagnosis and management of portal hypertension in advanced chronic liver disease (Billroth IV)*. Wien Klin Wochenschr, 2023. **135**(Suppl 3): p. 493-523.
15. Simbrunner, B., et al., *Recent advances in the understanding and management of hepatorenal syndrome*. Fac Rev, 2021. **10**: p. 48.
16. Nayak, S.L., et al., *Bile Cast Nephropathy in Patients with Acute Kidney Injury Due to Hepatorenal Syndrome: A Postmortem Kidney Biopsy Study*. J Clin Transl Hepatol, 2017. **5**(2): p. 92-100.
17. Krones, E., et al., *NorUrsodeoxycholic acid ameliorates cholemic nephropathy in bile duct ligated mice*. J Hepatol, 2017. **67**(1): p. 110-119.
18. Allegretti, A.S. and J.M. Belcher, *Bile Acids Are Important Contributors to AKI Associated with Liver Disease: CON*. Kidney360, 2022. **3**(1): p. 21-24.
19. Fickert, P. and A.R. Rosenkranz, *Bile Acids Are Important Contributors to AKI Associated with Liver Disease: PRO*. Kidney360, 2022. **3**(1): p. 17-20.
20. Ghallab, A., et al., *Interruption of bile acid uptake by hepatocytes after acetaminophen overdose ameliorates hepatotoxicity*. J Hepatol, 2022. **77**(1): p. 71-83.

References

21. Ghallab, A., et al., *Bile Microinfarcts in Cholestasis Are Initiated by Rupture of the Apical Hepatocyte Membrane and Cause Shunting of Bile to Sinusoidal Blood*. Hepatology, 2019. **69**(2): p. 666-683.
22. Wilson, F.A., et al., *Sodium-coupled taurocholate transport in the proximal convolution of the rat kidney in vivo and in vitro.* J Clin Invest, 1981. **67**(4): p. 1141-50.
23. Truong, J.K., et al., *Ileal bile acid transporter inhibition in Cyp2c70 KO mice ameliorates cholestatic liver injury.* J Lipid Res, 2022. **63**(9): p. 100261.
24. Kunst, R.F., et al., *Systemic ASBT inactivation protects against liver damage in obstructive cholestasis in mice.* JHEP Rep, 2022. **4**(11): p. 100573.
25. Ghallab, A., et al., *Spatio-Temporal Multiscale Analysis of Western Diet-Fed Mice Reveals a Translationally Relevant Sequence of Events during NAFLD Progression.* Cells, 2021. **10**(10).
26. Patro, R., et al., *Salmon provides fast and bias-aware quantification of transcript expression*. Nat Methods, 2017. **14**(4): p. 417-419.
27. C, T.R., *language and environment for statistical computing. R Foundation for Statistical Computing*. 2022.
28. Love, M.I., et al., *Tximeta: Reference sequence checksums for provenance identification in RNA-seq*. PLoS Comput Biol, 2020. **16**(2): p. e1007664.
29. Love, M.I., W. Huber, and S. Anders, *Moderated estimation of fold change and dispersion for RNA-seq data with DESeq2.* Genome Biol, 2014. **15**(12): p. 550.
30. Zhu, A., J.G. Ibrahim, and M.I. Love, *Heavy-tailed prior distributions for sequence count data: removing the noise and preserving large differences.* Bioinformatics, 2019. **35**(12): p. 2084-2092.
31. Nell, P., et al., *Identification of an FXR-modulated liver-intestine hybrid state in iPSC-derived hepatocyte-like cells.* J Hepatol, 2022. **77**(5): p. 1386-1398.
32. Alexa, A., J. Rahnenführer, and T. Lengauer, *Improved scoring of functional groups from gene expression data by decorrelating GO graph structure.* Bioinformatics, 2006. **22**(13): p. 1600-7.
33. Shinde, V., et al., *Definition of transcriptome-based indices for quantitative characterization of chemically disturbed stem cell development: introduction of the STOP-Tox(ukn) and STOP-Tox(ukk) tests*. Arch Toxicol, 2017. **91**(2): p. 839-864.
34. John3, M.H.H.B.S., *Physiology, Bile Secretion*. 2022.
35. Cai, S.Y. and J.L. Boyer, *The role of bile acids in cholestatic liver injury.* Ann Transl Med, 2021. **9**(8): p. 737.

15 Acknowledgments

I would like to express my deepest gratitude to the people who have supported me throughout my PhD and my life. This achievement would not have been possible without their support, encouragement, love and unwavering belief in me.

First, I want to thank Prof. Dr. med. Jan G. Hengstler for giving me the amazing opportunity to do my PhD. I can't thank you enough for being there for me every step of the way. Thank you for believing in me and for being such an exceptional mentor.

I would like to express my deepest gratitude to my co-supervisor Dr Ahmed Ghallab, whose unwavering support, guidance, and encouragement have been invaluable throughout my PhD. You have been more than just a mentor, you have been like an elder brother, always there to provide assistance, advice, and motivation at every step. Your dedication, patience, and insightful feedback have greatly contributed to my academic and personal growth. Without your constant support, achieving this milestone would not have been possible. I am truly grateful for everything I have learned from you, and I will always appreciate your kindness and generosity. Thank you for everything.

I would also like to thank the whole junior group for being so supportive and helpful. I'd like to thank Dr. Reham Hassan, Dr. Dani Gonzalez, and especially Dr. Maiju Myllys, you've all been such great colleagues and friends to me over the years, and I really appreciate it. You've all been so supportive and helpful, and I can't thank you enough.

I would like to acknowledge Erik Lindström (Albireo Pharma Inc, Boston, MA, USA) and Santosh Kulkarni, Runa Pal, Atul Tiwari, Shivendra Singh, Ramesh Kangarajan, Ashwani Gaur (Syngene International, Bangalore, India) for their contributions to the development of AS0369.

I am grateful for all the technical support I have got. Thank you, Brigitte Begher-Tibbe, for your

help especially with MALDI-MSI. Thank you for Dr. rer. nat. Stefan Höhme for data analysis. Thank you Dr. Jörg Reinders for bile acid analysis.

My heartfelt thanks go to my beloved family. To my husband, whose patience, understanding, and constant support kept me going even in the toughest times. To my wonderful children, who filled my life with love and purpose, reminding me why I embarked me on this PhD in the first place. To Maria and Nabil, who stood by my side, offering their kindness and encouragement whenever I needed it.

Above all, I dedicate this achievement to my late Father. Though he is no longer physically with me, his dreams, his wishes, and his love have never left my heart. He always wanted to see me earn my doctorate, and I hope this accomplishment makes him proud.

Lastly, I extend my gratitude to my big Family especially to my mother, for the beautiful moments, for their endless support, and for making Life’s journey so meaningful.

Eidesstaatliche Versicherung

16 Eidesstaatliche Versicherung/Affidavit

NAME: Zaynab Hobloss **Matrikelnummer:** 268832

Ich versichere hiermit an Eides statt, dass ich die vorliegende Dissertation mit dem folgenden Titel:

Renal ASBT as a therapeutic target for cholemic nephropathy caused by cholestatic liver diseases

selbstständig und ohne unzulässige fremde Hilfe erbracht habe. Ich habe keine anderen als die angegebenen Quellen und Hilfsmittel benutzt sowie wörtliche und sinngemäße Zitate kenntlich gemacht. Die Arbeit hat in gleicher oder ähnlicher Form noch keiner Prüfungsbehörde vorgelegen.

_____ _____

Ort, Datum **Unterschrift**

Belehrung: Wer vorsätzlich gegen eine die Täuschung über Prüfungsleistungen betreffende Regelung einer Hochschulprüfungsordnung verstößt, handelt ordnungswidrig. Die Ordnungswidrigkeit kann mit einer Geldbuße von bis zu 50.000,00 € geahndet werden. Zuständige Verwaltungsbehörde für die Verfolgung und Ahndung von Ordnungswidrigkeiten ist der Kanzler/die Kanzlerin der Technischen Universität Dortmund. Im Falle eines mehrfachen oder sonstigen schwerwiegenden Täuschungsversuches kann der Prüfling zudem exmatrikuliert werden. (§ 63 Abs. 5 Hochschulgesetz - HG -). Die Abgabe einer falschen Versicherung an Eides statt wird mit Freiheitsstrafe bis zu 3 Jahren oder mit Geldstrafe bestraft. Die Technische Universität Dortmund wird gfls. elektronische Vergleichswerkzeuge (wie z.B. die Software „turnitin“) zur Überprüfung von Ordnungswidrigkeiten in Prüfungsverfahren nutzen.

Die obenstehende Belehrung habe ich zur Kenntnis genommen:

_____ _____

Ort, Datum **Unterschrift**